

Multidecadal and NAO related variability
in a numerical model of the
North Atlantic circulation

Dissertation

zur

Erlangung des Grades eines
Doktors der Naturwissenschaften

- Dr. rer.nat. -

Dem Fachbereich Physik der

Universität Bremen

vorgelegt von

Jennifer P. Brauch

1. Gutachter : Prof Dr. D. Olbers

2. Gutachter : Prof Dr. P. Lemke

ALFRED-WEGENER-INSTITUT FÜR POLAR- UND MEERESFORSCHUNG

BREMERHAVEN, OKTOBER 2003

Jennifer P. Brauch

UVic Climate Modelling Research Group
PO Box 3055, Victoria, BC, V8W 3P6, Canada
<http://climate.uvic.ca/>
jbrauch@uvic.ca

This work is the unchanged version of a phd thesis, which was presented to the Fachbereich Physik/Elektrotechnik of the Universität Bremen in 2003. It is available in printed form at the Alfred Wegener Institut (<http://www.awi-bremerhaven.de/Library>).

Contents

List of Figures	iv
List of Tables	v
Zusammenfassung	vii
Abstract	viii
1 Introduction	1
2 Background	5
2.1 Main Characteristics of the Arctic and North Atlantic Ocean	5
2.1.1 Bathymetry	5
2.1.2 Major currents	7
2.1.3 Hydrography	8
2.1.4 Sea ice	11
2.1.5 Convection	12
2.2 Variability	13
2.2.1 NAO	13
2.2.2 Variability in the Arctic Mediterranean	16
2.2.3 GSA	19
2.2.4 Oscillations in ocean models	20
3 Model description	23
3.1 Ocean model	23
3.1.1 Equations	24
3.1.2 Setup	26
3.2 Sea Ice model	29
3.2.1 Equations	29
3.2.2 Setup	35
3.3 Data exchange	37

4	Atmospheric forcing	41
4.1	OMIP data	41
4.2	NAO+ and NAO– composites	42
4.3	Discussion	46
5	Spin up	49
5.1	Hydrography	49
5.2	Circulation	54
5.3	Heat transport	59
5.4	Ice distribution	61
5.5	Discussion	63
6	Sensitivity experiments	67
6.1	Design	68
6.2	Results	69
6.2.1	Response of the ice fields	69
6.2.2	Response of the ocean fields	72
6.3	Discussion	82
6.4	Conclusions	83
7	Internal variability	85
7.1	First look at the oscillation	86
7.2	Role of the Labrador Sea	93
7.3	Discussion	99
7.4	Conclusions	101
8	Final conclusions and outlook	103
	Bibliography	107
	Acknowledgements	123

List of Figures

1.1	Icelandic winter fishery 1600–1882 and sea surface temperature	2
2.1	Arctic Mediterranean Sea	6
2.2	Major Currents	7
2.3	Major Currents	9
3.1	Model grid	26
3.2	Depth levels	26
3.3	Model topography	28
4.1	Mean of the windstress fields	42
4.2	Mean of the surface air temperature	43
4.3	Difference between the NAO+ and NAO– composite of the wind stress	44
4.4	Difference between the NAO+ and NAO– composite of the two metre temperature	45
4.5	Mean of the magnitude of the wind stress vector	47
5.1	Temperature in 300 m depth	50
5.2	Salinity in 300 m depth	53
5.3	Mean vertically integrated streamfunction	55
5.4	Mean mixed layer depth	56
5.5	Mean zonally integrated overturning	58
5.6	Heat transport	59
5.7	Decomposition of the heat transport	60
5.8	Anomaly of the northward heat transport	61
5.9	Mean ice transport	62
5.10	Annual mean of the maximum of the meridional overturning	65
6.1	NAO Index	67
6.2	Experimental design	68
6.3	Difference of sea ice concentration between SWITCH and CTRL	70
6.4	Difference of sea ice thickness between SWITCH and CTRL	71
6.5	Difference of sea ice growth of SWITCH and SPIKE	72
6.6	Deviation of the meridional overturning from CTRL	73

6.7	Annual mean meridional overturning of the SWITCH	74
6.8	Annual mean meridional overturning of the SWITCH _{ow}	74
6.9	Difference between SWITCH and CTRL in the barotropic streamfunction .	76
6.10	Annual mean velocity field	77
6.11	Annual means of the integrated potential energy anomaly of SWITCH . .	78
6.12	Annual mean of the integrated potential energy anomaly of SWITCH _{ow} .	79
6.13	Maximal convection depth in the Labrador box	80
6.14	Deviation of meridional heat transport at 48°N from CTRL	81
7.1	Time series of the oscillation	85
7.2	Lagged regression between overturning and streamfunction	87
7.3	Fluctuations of the meridional heat transport	88
7.4	Lagged regression between the overturning and the surface salinity	89
7.5	Mean tracer profiles in the Labrador box	90
7.6	Maximal convection depth in the Labrador box	90
7.7	Lagged regression between overturning and the surface salinity	92
7.8	Cross-spectra of the maximum of the overturning maximum of the con- vection in the Labrador box	94
7.9	Temporal derivatives of the density difference between two layers	95
7.10	Annual means of the streamfunction and surface density	96
7.11	Annual means of salt transport in two layers	97
7.12	Sketch of an oscillation cycle	102

List of Tables

3.1	Parameterisations for the ocean model	29
3.2	Parameters used in the ice model	36
5.1	Maxima of important quantities for the three spin up experiments	54
5.2	Mean ice export and ice volume	63
6.1	Total ice volume and area and ice export to the south	70

Zusammenfassung

Das Verständnis der natürlichen Variabilität des Nordatlantischen und Arktischen Ozeans ist noch immer unzureichend. Besonders auf Zeitskalen von zwischenjähriger bis multidekadischer Variabilität, auf welchen die Verfügbarkeit der Daten limitiert ist, verbleiben noch viele offene Fragen. Diese Studie beschäftigt sich mit der Reaktion eines numerischen Modells des Nordatlantischen und Arktischen Ozeans auf Änderungen des Oberflächenantriebs und versucht das Verständnis der internen Variabilität des Modells und darüber hinaus des realen Ozean–Meereissystems zu verbessern.

Das Ozeanmodell basiert auf dem MOM-2 Kode, welches mit einem dynamisch–thermodynamischen Meereismodell mit einer viskos–plastischen Rheologie gekoppelt ist.

Der Hauptmode der atmosphärischen Variabilität über dem Nordatlantik ist die Nordatlantische Oszillation (NAO). Zwei Integrationen über 200 Jahre mit dem gekoppelten Ozean–Meereismodell werden mit atmosphärischem Antrieb durchgeführt, welcher einerseits mit positiver und andererseits mit negativer NAO assoziiert ist. Diese Integrationen werden mit einem Kontrolllauf über den gleichen Zeitraum verglichen, der mit einem klimatologischen Antrieb gerechnet wurde. Alle drei Experimente zeigen einen voneinander abweichenden langfristigen Trend, der in der Zunahme des Maximums der meridionalen Umwälzbewegung (Overturning) ersichtlich ist. Der Grad der internen Variabilität unterscheidet sich auch deutlich zwischen den Experimenten.

Der Kontrolllauf mit dem klimatologischen Antrieb entwickelt nach circa 80 Jahren eine Oszillation mit einer Periodizität von 40 Jahren. Der Mechanismus umfaßt den Transport von warmen, salzreichen Oberflächenanomalien subtropischen Ursprungs, die in das Gebiet des Subpolarwirbels advehiert werden, wodurch sich in diesem Gebiet die Konvektion und somit auch die Tiefenwasserbildung verstärkt. Das Zusammenspiel des tiefen westlichen Randstroms (DWBC) und des Golfstroms ist entscheidend für das Aufrechterhalten der Oszillation.

Die Integration mit atmosphärischen Antrieb, der mit einer positiven NAO Phase assoziiert wird, ist der Ausgangspunkt, um die Reaktion des Ozean–Meereis–Systems auf ein langfristiges Umschalten auf NAO–Antrieb zu untersuchen. Die Meereisausdehnung reagiert instantan auf das Umschalten, wohingegen sich die Meereisdicke langsamer an den neuen Antrieb anpaßt. Der Nordatlantische Ozean durchläuft eine schnelle, barotrope Anpassungsphase, die mit einem kurzfristigen Anstieg der meridionalen Umwälzbewegung und des nordwärtigen Wärmetransports bei 48°N verbunden ist. Die langfristige Anpassung zieht eine Abnahme des nordwärtigen Wärmetransports, eine Abnahme der Stärke des Subpolaren und Subtropischen Wirbel und eine Abnahme der meridionalen Umwälzbewegung nach sich.

Ein Experiment, welches nur für ein Jahr mit dem NAO–Antrieb gerechnet wird und anschließend wieder mit NAO+ Antrieb, verschiebt das Konvektionsgebiet in der Labrador See nach Nordwesten, was sich als neuer Gleichgewichtszustand des Ozeans herausstellt.

Abstract

The natural variability of the North Atlantic and Arctic Ocean is still not completely understood. Especially on interannual to multidecadal time scales, where the amount of observations is limited, many open questions remain. The objective of this study is therefore to investigate the reaction of a numerical model of the North Atlantic and Arctic Ocean to changes in the atmospheric surface forcing and to improve the understanding of the internal variability of the model and furthermore the real ocean–sea ice system. The ocean model is based on the MOM–2 code, which is coupled to a dynamic–thermodynamic sea ice model with a viscous–plastic rheology.

A major mode of atmospheric variability over the North Atlantic Ocean is the North Atlantic Oscillation (NAO). Two 200 year integrations of the coupled ocean–sea ice model with surface boundary conditions which are related to periods of positive and negative NAO are compared to an integration with climatological atmospheric forcing over the same number of years. All three experiments are characterised by a different long term trend in the time series of the maximum of the meridional overturning which approximately lasts for the first hundred years of integration. Also, the degree of internal variability differs between the experiments. The experiment with climatological forcing reveals a self-sustaining oscillation. The period of the oscillation is about 40 years. The mechanism is the advection of saline and warm subtropical surface anomalies in the region of the subpolar gyre, where the deep water formation is enhanced due to enhanced convection. The interplay between the Deep Western Boundary Current (DWBC) and Gulf Stream is important to sustain the oscillation.

A switch from a long time NAO+ state to an enduring NAO– situation is also investigated in this study. The sea ice extent increases quickly after this switch, whereas the changes in sea ice volume adapt slower to the changed forcing, because of the integral effect of the ocean mixed layer and ice thickness itself. The ocean adjusts with a fast barotropic circulation anomaly, accompanied by an enhancement of meridional overturning and northward heat transport at 48°N. The slow response is a substantial decrease of the northward heat transport, which is caused by a reduction of the strength of subpolar and subtropical gyres and a decrease of the meridional overturning.

One year of NAO– forcing shifts the area of convection in the Labrador Sea to a different position, which turns out to be a new state of equilibrium for the ocean.

What in water did Bloom, waterlover, drawer of water, watercarrier, returning to the range, admire?

Its universality; its democratic equality and constancy to its nature in seeking its own level; its vastness in the ocean of Mercator's projection;

[. . .]

the restlessness of its waves and surface particles visiting in turn all points of its seaboard; the independence of its units; the variability of states of sea; its hydrostatic quiescence in calm; its hydrokinetic turgidity in neap and spring tides; its subsidence after devastation; its sterility in the circumpolar icecaps, arctic and antarctic; its climatic and commercial significance; its preponderance of 3 to 1 over the dry land of the globe;

[. . .]

its vehicular ramifications in continental lakecontained streams and confluent oceanflowing rivers with their tributaries and transoceanic currents, gulfstream, north and south equatorial courses; its violence in seaquakes, waterspouts, Artesian wells, eruptions, torrents, eddies, freshets, spates, groundswells, watersheds, waterpartings, geysers, cataracts, whirlpools, maelstroms, inundations, deluges, cloudbursts; its vast circumterrestrial ahorizontal curve; its secrecy in springs, and latent humidity, revealed by rhabdomantic or hygrometric instruments and exemplified by the well by the hole in the wall at Ashtown gate, saturation of air, distillation of dew; the simplicity of its composition, two constituent parts of hydrogen with one constituent part of oxygen;

[. . .]

its infallibility as paradigm and paragon; its metamorphoses as vapour, mist, cloud, rain, sleet, snow, hail; its strength in rigid hydrants; its variety of forms in loughs and bays and gulfs and bights and guts and lagoons and atolls and archipelagos and sounds and fjords and minches and tidal estuaries and arms of sea; its solidity in glaciers, icebergs, icefloes; its docility in working hydraulic millwheels, turbines, dynamos, electric power stations, bleachworks, tanneries, scutchmills; its utility in canals, rivers, if navigable, floating and graving docks; its potentiality derivable from harnessed tides or watercourses falling from level to level;

[. . .]

its ubiquity as constituting 90% of the human body;

from James Joyce, *Ulysses*

1 Introduction

“You don’t buy a fish, you buy the life of a human being”

SIR WALTER SCOTT, *The Antiquary*, 1816

This is a central phrase from the book by [KURLANSKY \(1997\)](#) about a fish that changed the world. The book tells a story about the importance of cod in the old and new worlds culminating in the recent near extinction of cod. At all times, fishermen were forced to search for fish populations which tend to appear and disappear unpredictably. This led to a wide range of socio-economic consequences such as prosperity and expansion as well as famine and war. The prospect of understanding and perhaps predicting fish stock developments is the key towards mitigation and a sensible use of this natural resource for food.

It is a well known fact that climatic changes have effects on the fish population, although these changes are different for different species. The effect of climate on fish populations is summarised by [WESTERNHAGEN AND SCHNACK \(2001\)](#). One example in the article is the Icelandic cod fishery, where the fish landings (or catches) are documented from the year 1600 to 1900 ([JONSSON, 1994](#)). It is compared to a time series of the sea surface temperature (SST), which was derived from the amount of drift ice around Iceland. The increase of cod landings closely follows the increasing SST and vice versa as shown in Fig. 1.1. Over these 300 years, fish landings decline and recover in a cycle of 50–60 years, which is attributed to natural climate variability, since there was no industrial fishery at this time. The onset of commercial fishery at the beginning of the 20th century changed this quasi–equilibrium. In the first half of the century, cod landings reached an astronomical height of 6.6 million tons in one year, compared to between 20000 and 30000 tons in earlier years. At the end of the 20th century, the total landings are at a historical low. In this example, natural variability and anthropogenic influences are clearly separable because of the favourable circumstances of long time series. Unfortunately, this is an exception. Long time series of observations of fish populations and climate variability are very sparse and exist only for distinct parameters and locations. Thus, it is important to understand the mechanisms of natural climate variability to be able to distinguish and quantify anthropogenic effects.

Around Iceland, the variability of cod recruitment and SST agree well, but in the view of climate variability, it is important to find a more robust connection which accounts for a larger area. [PLANQUE AND FRÉDOU \(1999\)](#) compared the variation in recruitment of nine cod stocks in the eastern and western North Atlantic Ocean to the North Atlantic SST and found robust correlations: positive in cold waters, none in temperate waters

and negative correlation in warm waters. According to the authors, the relationship for individual cod stocks and the SST is weak, so that the uncertainty associated with any prediction would be high.

The next question is what is the origin of the SST variations. An early detailed analysis of Atlantic air–sea interaction was published by BJERKNES (1964). He could explain the variability in SST on interannual time scales by direct forcing from the variability of the North Atlantic winter sea level pressure (SLP) field. On inter decadal time scales, the SST variations could only be explained by additional contributions from internal variability in the ocean. This time scale dependence was supported by observational studies, e.g. DESER AND BLACKMON (1993) and KUSHNIR (1994). The authors argued that SST reacts passively to changes in the atmosphere on time scales shorter than ten years, but is driven by the ocean on longer time scales.

The North Atlantic winter SLP field has been indexed by the pressure difference between the Icelandic Low and the Azores High. This index is called the North Atlantic Oscillation (NAO) index and it accounts for more than one third of the total variance of the winter SLP field (HURRELL, 1995). The SLP pattern that is associated with a “high” NAO index (positive values of the NAO index) is characterised by a deep Icelandic Low, a pronounced Azores High, and strong westerlies. The “low” NAO index SLP pattern is associated with a substantially reduced difference between the Icelandic low and the Azores high, and weak westerlies. The NAO index is based on instrumental records of SLP (since the mid-1800s at the earliest) at distinct locations, such as Iceland and the Iberian Peninsula or the Azores, depending on the exact definition of the NAO index. The variability of the NAO is linked to changes in the atmospheric temperature, precipitation

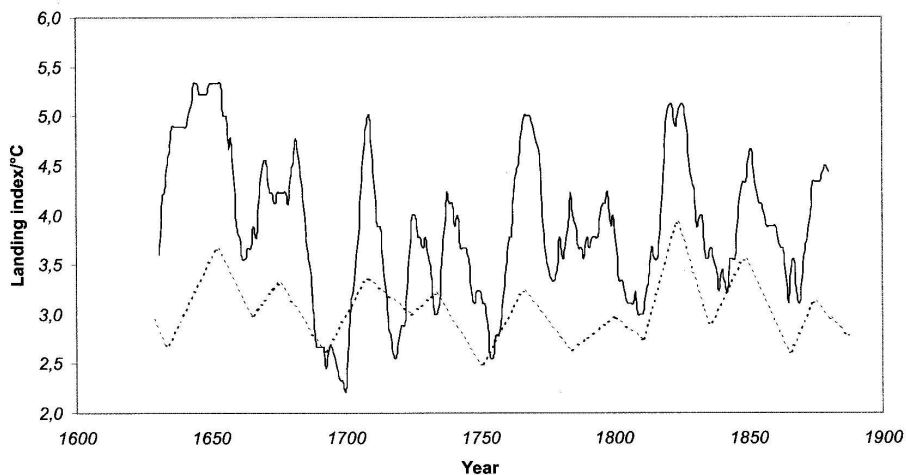


Figure 1.1: Icelandic winter fishery 1600–1882 (according to JONSSON (1994)); dotted line: sea surface temperature in °C; solid line: landings, calibrated on a scale from 1–6 (6=best catches), and filtered with a nine year running mean; graphic is taken from WESTERNHAGEN AND SCHNACK (2001)

patterns, and storm track activity HURRELL (1995). While most evident in the large-scale wind field, the NAO is also associated with interannual variability in ocean-atmosphere heat fluxes and SST forcing over the North Atlantic (CAYAN, 1992).

Although BJERKNES (1964) postulated the importance of the ocean for the explanation of the variability, it is still a subject of controversy. An atmospheric general circulation model of JAMES AND JAMES (1989) with only climatological oceanic forcing could produce NAO-like fluctuations with similar spectral characteristics to those observed. The feedback from the ocean to the atmosphere seems to be unimportant in this study. The spectral density of the observed NAO index is weakly red (WUNSCH, 1999), with slight broadband features at periods around 2.5 and 8 years. This weakly “red behaviour” does produce a predictability of the NAO index with a small degree of skill. WUNSCH (1999) advises caution in the interpretation of short records but, on the other hand, seeks explanations of this “red behaviour”. These are only some examples of the discussion about the dynamics linked to the NAO.

One approach to understand the variability of the NAO and thus of SST is to employ fully coupled climate models, which can capture all subcomponents and their variability: the atmosphere, ocean, cryosphere and land/biosphere. At present, the reproduction of the climate system in models is imperfect, because there are still many unsolved problems of a technical or scientific nature in understanding the single components individually and, furthermore, their coupling. Another way is to investigate the response of subsystems like the ocean or, as in this study, the coupled ocean-sea ice system to the atmospheric NAO. This improves the understanding of the capability of the subsystems to modulate, produce and maintain variability.

In this study, the variability of the North Atlantic and Arctic Ocean is under investigation in the light of influences from the atmosphere and also its internal variability. The present work concentrates on the time scale dependence of the response of the ocean-sea ice system to the NAO. Two questions are, what kind of events a sharp transition from one extreme event to another could trigger in the ocean-sea ice model on short time scales, and which features are persistent or long lasting effects. The role of the Arctic Ocean and the sea ice will be discussed in the view of the time dependence of the reaction and the influence on the North Atlantic Ocean. Another interesting aspect is the question of which mechanisms are involved in a self-sustaining internal variability in the ocean-sea ice system.

Chapter 2 gives a broad introduction to the area which is covered by the model and the background knowledge about atmospheric, oceanic and sea ice variability. One subsection contains an overview about the NAO in observations and models. A general introduction to the internal variability of the ocean follows in section 2.2.4. The ocean and sea ice models, their coupling and the basic setup are described in chapter 3. The atmospheric forcing data are introduced and discussed in chapter 4. Chapter 5 illustrates the main features of the model in a quasi-equilibrium as the results of three different spin-up integrations. In chapter 6, the response of the ocean-sea ice model to a sharp transition

of the atmospheric conditions is studied. The description of a long term oscillation of the ocean–sea ice system with climatological atmospheric forcing follows in chapter 7. The summary and outlook are given in the last chapter. Hope you enjoy reading this thesis.

2 Background

2.1 Main Characteristics of the Arctic and North Atlantic Ocean

2.1.1 Bathymetry

The Arctic Mediterranean Sea belongs to the class of mediterranean seas. As indicated by its name, these are defined as parts of the world ocean, which have only limited connections to the major ocean basins, such as Pacific, Atlantic or Indian Oceans. Their circulation is dominated by thermohaline forcing. The Arctic Mediterranean Sea comprises the area north of the Greenland–Scotland Ridge^I and the Bering Strait described by [SVERDRUP ET AL. \(1942\)](#) (Fig. 2.1). The Arctic Ocean denotes the ocean around the North Pole, the Beaufort Sea and the shallow shelf seas (starting at the Bering Strait in clockwise direction): the Chukchi Sea, the East Siberian Sea, the Laptev Sea, the Kara Sea and the Barents Sea. The shelf areas are all less than 200 m deep. The deep basins of the Arctic Ocean are separated by the Lomonosov Ridge (at approximately 40°W), into the Canadian and Makarov Basins on the western side and the Amundsen and Nansen Basins on the eastern side. The Amundsen and Nansen Basins together are called the Eurasian Basin. These basins reach depths of over 4000 m, the Lomonosov Ridge has a sill depth of 1600 to 2000 m. The Bering Strait connects the Pacific Ocean and the Arctic Ocean. It is 45 m deep and 85 km wide. The Canadian Archipelago controls the exchange between the Arctic Ocean and the Atlantic Ocean west of Greenland. The main passages are the Nares Strait and Smith Sound with sill depth less than 250 m. They both link the Arctic Ocean to the Baffin Bay. The latter is connected via the Davis Strait to the Labrador Sea (350 km width and less than 600 m depth). Due to the coarse resolution of the model this link between the Arctic and Atlantic Oceans is realised as one passage, which will be addressed as Davis Strait in the following. The Fram Strait, which is situated between Greenland and Svalbard^{II}, connects the Arctic Ocean with the Nordic Seas. It is 600 km wide and has a threshold depth of 2600 m. It is therefore the deepest connection of the Arctic Ocean to the south. The eastern part of the Fram Strait has a relatively narrow shelf, but the shelf on the Greenland coast is several hundred kilometres wide. There is also a broad and shallow (maximum depth is 500 m) passage between Svalbard and

^IThe Greenland–Scotland Ridge comprises Denmark Strait (between Greenland and Iceland), Faroe–Iceland sill (between Iceland and the Faroe Islands), Faroe Bank Channel (between the Faroe Islands and Scotland)

^{II}Svalbard is a group of several islands, with Spitsbergen being the largest

Main Characteristics of the Arctic and North Atlantic Ocean

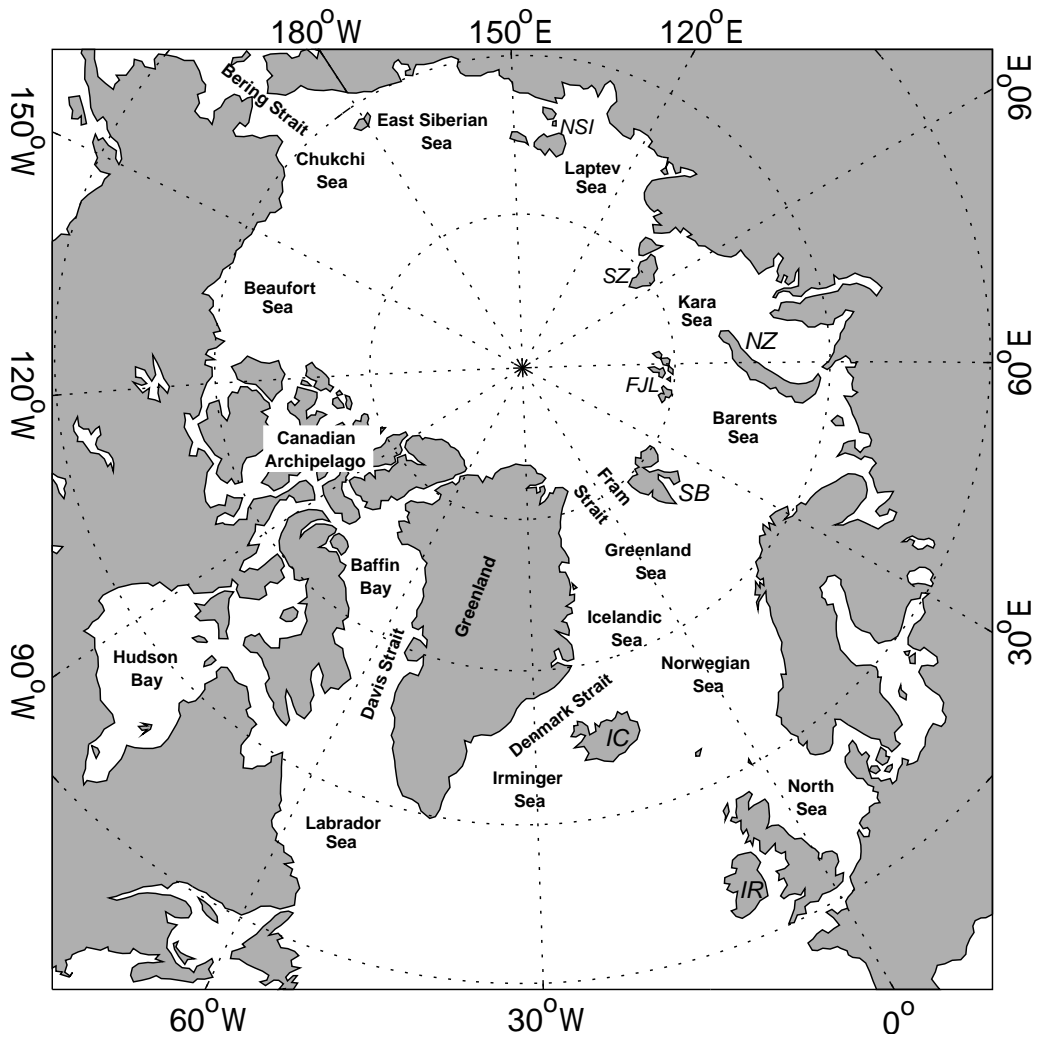


Figure 2.1: Arctic Mediterranean Sea, NZ: Novaja Zemlja, NSI: New Siberian Islands, SZ: Severnaja Zemlja, FJL: Franz–Josef–Land, SB: Svalbard, IC: Iceland, IR: Ireland

Scandinavia, which will be called Barents Sea Opening (BSO) in the following. South of Fram Strait and BSO lie the Nordic Seas, which comprise the Greenland, Iceland and Norwegian Seas, often dubbed GIN Sea. The southern boundary of the Nordic Seas is the Greenland–Scotland Ridge with a width of 1700 km. The sill depth in the Denmark Strait is approximately 600 m, 400 m between Iceland and the Faroe Islands, and 800 m in the Faroe Bank Channel. The Denmark Strait connects the Nordic Seas and the Irminger Sea, which is a marginal sea of the North Atlantic Ocean. Other marginal seas in the North Atlantic are the Labrador Sea and the North Sea, and the Baffin Bay. The Atlantic Ocean is divided by the Mid–Atlantic Ridge into an eastern and a western basin of almost equal sizes. In most parts the Mid–Atlantic Ridge rises to about 2000 m depth, with some elevations up to 1000 m depth. The existence and geographical extension of the Mid–Atlantic Ridge poses an important constraint for the circulation in the deep layers of the Atlantic.

2.1.2 Major currents

In the tropical Atlantic Ocean, surface water is heated by the atmosphere, precipitation and evaporation modulate its salinity. A series of currents such as the North Brazil Current, the Antilles Current, the Florida Current and the Gulf Stream, which are part of the subtropical gyre, transport the warm and saline surface water to mid and high latitudes (Fig 2.2). The subtropical gyre has several recirculation loops. The Azores Current forms one of its major branches. The Gulf Stream separates from the North American continent and is then called the North Atlantic Current (NAC). This is already part of the subpolar gyre, which involves also the Irminger Current, the East and West Greenland Current and the Labrador Current. Besides the Irminger Current the North Atlantic Current also feeds the Norwegian Atlantic Current. It carries surface water which is called Atlantic



Figure 2.2: Sketch of the major currents of the North Atlantic and Arctic Ocean. **Warm Currents (red):** NBC: North Brazil Current, ANC: Antilles Current, FC: Florida Current, GS: Gulf Stream, NAC: North Atlantic Current, AC: Azores Current, IC: Irminger Current, NWAC: Norwegian Atlantic Current, WSC: West Spitsbergen Current. **Cold Currents (light blue):** TPD: Transpolar Drift, BG: Beaufort Gyre, EGC: East Greenland Current, WGC: West Greenland Current, LC: Labrador Current. **Deep Current (blue):** NADW: Pathway of the overflow water and North Atlantic Deep Water

Main Characteristics of the Arctic and North Atlantic Ocean

Water. The Subpolar Front, spanning from 35°N, 30°W to 55°N, 30°W, separates warm, subtropical water masses and cold, polar water masses. In the Nordic Seas the Norwegian Atlantic Current splits into three branches: the first flows to the east into the Barents Sea, the second enters the Arctic Ocean via Fram Strait as West Spitsbergen Current and the third is a recirculation branch, which flows with the East Greenland Current to the south in the western part of the Nordic Seas. The Barents Sea branch cools on its path through the Barents Sea and sinks underneath the cold and less saline surface water. It leaves the Kara Sea between Franz–Josef–Land and Severnaja Zemlja to flow in a north-easterly direction into the Arctic Ocean. The water mass, which entered the Arctic Ocean with the West Spitsbergen Current, flows eastward along the continental slope. North of the Kara Sea it unites with part of the Atlantic Water that crossed the Barents Sea. The inner Arctic Ocean has two main currents, which are the Transpolar Drift moving water from the Eurasian Basin across the North Pole towards the Fram Strait, and the Beaufort Gyre, an anticyclonic circulation in the Canadian basin. There is an inflow of water from the Pacific Ocean through Bering Strait, but it is of minor importance for the circulation in the North Atlantic except for the freshwater budget. The Arctic Front, which separates the Atlantic and the Pacific water masses coincides with the TPD.

2.1.3 Hydrography

Arctic Mediterranean

Since in the Arctic Mediterranean Sea precipitation exceeds evaporation, this region supplies freshwater for the Atlantic Ocean. Additionally, many rivers discharge into the Arctic Ocean adding more freshwater. In other mediterranean seas with positive freshwater balance (i.e. the Baltic Sea), there is an outflow of freshwater at the surface and inflow of dense water underneath. The exchange processes of the Arctic Mediterranean Sea are different, because the inflowing dense Atlantic Water is not as dense as the bottom water in the Arctic Ocean and Nordic Seas. Therefore, the Atlantic Water does not sink to the bottom but spreads as intermediate water in the Arctic Mediterranean Sea. Furthermore, the outflow from the Arctic Mediterranean Sea is not restricted to the surface layers (TOMCZAK AND GODFREY, 1994). The major currents and water mass modifications of the Arctic Mediterranean Sea are summarised in a sketch by AAGAARD ET AL. (1985) (Fig. 2.3). The layered structure with three water masses is clearly visible in the vertical section. The upper 200 m of the Arctic Ocean are occupied by Polar Water or Arctic Surface Water. It has temperatures close to the freezing point and salinities of less than 30. This is the water mass, which is exported at the surface to the south through Fram Strait via the East Greenland Current. While temperature changes little with depth, salinity varies strongly. In summer, a seasonal halocline^{III} establishes at approximately 30–40 m depth (RUDELS, 1998), which is eroded in the next winter season by formation of sea ice. Underneath this seasonal layer, a second halocline separates the Polar Water

^{III}sharp change of salinity with depth

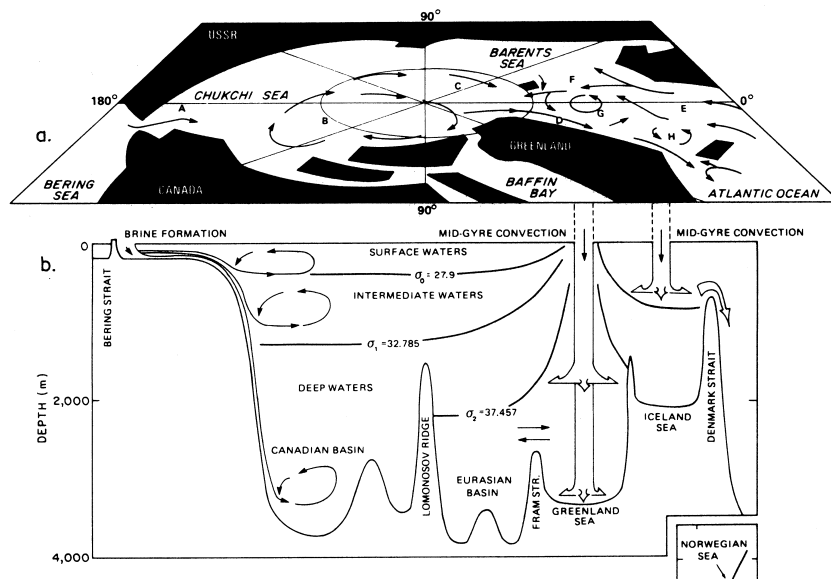


Figure 2.3: Schematic circulation and water mass structure in the Arctic Mediterranean from [AAGAARD ET AL. \(1985\)](#)

from the underlying Atlantic Water. This halocline^{IV} is permanently present above the deep basins of the Arctic Ocean and prevents open ocean convection. Since the thermal expansion coefficient for sea water at low temperature is very small and thus its effect on the density structure is negligible, the halocline and the pycnocline are essentially the same. The halocline is based on an advective process described in detail by [RUDELS \(1998\)](#). On its way north, the characteristics of the Atlantic Water are modified by heat loss to the atmosphere and net freshwater input in the Arctic Mediterranean Sea. In the Nordic Seas, it is present in the east as surface water, which is advected by the Norwegian Atlantic Current and in the west as intermediate water underneath the East Greenland Current, where it is called returning Atlantic Water ([RUDELS ET AL., 1999](#)). It enters the Arctic Ocean through the BSO and with the West Spitsbergen Current. In the Barents Sea, the Atlantic Water is diluted by melt water and cooled by heat loss to the atmosphere. It moves north between Franz–Josef–Land and Severnaja Zemlja, where it sinks as intermediate water. The Fram Strait branch is isolated from the atmosphere and from the sea ice cover by Polar Water. Thus the characteristics of the Fram Strait branch and the Barents Sea branch of the Atlantic Water differ when they meet again north of the Kara Sea. Atlantic Water continues to spread as a boundary current along the continental slope. The characteristic temperature maximum of Atlantic Water erodes on its way through the Arctic Mediterranean Sea, but it is still detectable in the Canadian Basin. The salinity is higher than in the surface water and slightly less than in the deep water. The sketch of [AAGAARD ET AL. \(1985\)](#), Fig 2.3, illustrates, in which depth horizons Atlantic Water or

^{IV}often referred to as “cold halocline” ([STEELE AND BOYD, 1998](#)), because it separates the cold, fresh surface water from the warmer, saltier Atlantic Water beneath

Main Characteristics of the Arctic and North Atlantic Ocean

its mixing products occur (approximately 200-1000 m). RIGOR ET AL. (2002) pointed out, that the deep currents of the Arctic Ocean flow counterclockwise and thus are decoupled from the anticyclonic surface currents (i.e. Beaufort Gyre, Fig. 2.2). The deep basins of the Arctic Ocean are filled with Arctic Bottom Water, where the densest fraction is found in the Canadian basin, with salinities higher than 34.95 (TOMCZAK AND GODFREY, 1994). In the Nordic Sea, Greenland Sea Deep Water and Norwegian Sea Deep Water is formed by open ocean convection, which will be explained in the section 2.1.5. The freshwater budget of the Arctic Mediterranean Sea was estimated by AAGAARD AND CARMACK (1989).

Atlantic Ocean

The hydrography of the Atlantic Ocean is very complex and only the most important aspects are discussed here. A more detailed overview can be found in TOMCZAK AND GODFREY (1994) or SCHMITZ (1996).

At the Greenland–Scotland Ridge an outflow of approximately 5.6 Sverdrup (1 Sv = $10^6 \text{ m}^3/\text{s}$) leaves the Arctic Mediterranean Sea in three branches (DICKSON AND BROWN, 1994) (Fig. 2.2). In the west, the export through the Denmark Strait contributes 2.9 Sv to the total transport. The overflow over the Iceland–Faroe sill and the Faroe Bank Channel together transport approximately another 2.9 Sv (DICKSON AND BROWN, 1994). The composition of this overflow water is highly variable and many studies have been undertaken to estimate its sources, its exact pathways and variability (to name just a few: SWIFT (1984); STRASS ET AL. (1993); DICKSON AND BROWN (1994); RUDELS ET AL. (1999); HANSEN ET AL. (2001); KÄSE ET AL. (2003)). On its way south, the overflow water is compelled by the Coriolis force to follow the western boundaries, which are the Greenland and Iceland shelves and the Mid–Atlantic Ridge. It sinks down according to its high density. During this process the water mass properties are changed by mixing and entrainment^V of ambient water masses (especially the intermediate water from the Mediterranean Sea and Antarctic Bottom Water). The three modified overflow branches are united at the southern tip of Greenland (Cape Farewell), where the transport of the deep western boundary current (DWBC) has increased to 13 Sv. The water mass at this point is called Lower North Atlantic Deep Water (LNADW). In the Labrador Sea, Labrador Sea Water (LSW) is produced by deep convection during winter months. LNADW and LSW mix and form Upper NADW (UNADW). LNADW and UNADW can be separated by their distinct temperature and salinity characteristics. Additional information to distinguish more precisely the age and sources of the individual components can be achieved by measuring tracers such as chlorofluorocarbons (CFCs) or helium/tritium (e.g. PICKART (1992), RHEIN (1994)). Fractions of NADW spread to the east and north, but the majority is transported southward (Fig. 2.2), between 500 and 2000 m with the DWBC (RHEIN, 2000). The DWBC is part of the lower branch of the global ocean circulation, sometimes called the global conveyor belt (BROECKER, 1991). In

^Vsurrounding water is mixed into the flow, therefore the properties and the transport of the flow are changed

Fig. 2.2 the main concept of the conveyor belt is indicated. Warm and salty water masses are transported at the surface from the tropics to the north. On its pathway the water is cooled and sinks down in distinct areas (Greenland Sea, Norwegian Sea and Labrador Sea). The dense water spreads as NADW southward in the South Atlantic, where it is advected to the east with the Antarctic Circumpolar Current. The Circumpolar Deep Water shows characteristics of the NADW and its pathway can be followed into the Indian and Pacific Oceans. There, the deep water is converted to surface water. The surface currents transport the warm water via the Indonesian throughflow and past South Africa back to the tropical Atlantic Ocean, thus closing the conveyor belt. GORDON (1986) proposed an alternative pathway ("cold water path"). Due to upwelling in the Antarctic Circumpolar Current, NADW is advected as intermediate water to the east through Drake Passage and enters the South Atlantic Ocean from the west. There are still uncertainties about the exact pathway and transport rates of the conveyor belt, because of sparse data availability and the long time scales involved. To travel one cycle of the thermohaline circulation, a water parcels needs about 1000 years. The circulation of the conveyor belt is driven by density gradients (horizontal and vertical) and governed by surface heat and fresh-water fluxes and sea ice formation. Thus it is mostly called the thermohaline circulation (THC). A detailed review of the THC can be found in SCHMITZ (1995), a quantification of water mass transports in MACDONALD AND WUNSCH (1996) and in GANACHAUD AND WUNSCH (2000). The THC plays an important role in the climate system, because of the large meridional heat transport it causes. ROEMMICH AND WUNSCH (1985) estimated a transport of 1.2 PW (1 Peta Watt= 10^{15} W) across 24°N towards the North Atlantic. Variability of this northward heat transport has large impacts of the climate on the northern hemisphere.

2.1.4 Sea ice

Sea ice is part of the cryosphere, which comprises all kinds of frozen water in the climate system. Since it acts as a barrier for the transfer of moisture, heat and momentum between the ocean and the atmosphere, sea ice is of great importance for the climate system. The main effects of sea ice in the climate system are outlined in the following.

The solar irradiation is the main source of heat for the ocean. The ocean can absorb 90% of the insolation, whereas the white surface of sea ice cover absorbs only about 20%, the remaining 80% are reflected to the atmosphere. An additional snow cover absorbs even less of the insolation. The discrepancy between the reflection characteristics of open ocean and sea ice cover causes the ice–albedo^{VI} temperature feedback (EICKEN AND LEMKE, 2001). When the sea ice starts to melt in early summer, the areas of uncovered ocean increase. As a consequence, the insolation penetrates the exposed ocean and heats the surface water mass. This increases the melting of the sea ice and the positive feedback loop is closed. As the ice–albedo temperature effect modulates the energy balance, it is an important contribution for the variability in the climate system.

^{VI}proportion of incident radiation reflected by a surface

Main Characteristics of the Arctic and North Atlantic Ocean

The temperature gradient between the relatively warm ocean and the cold atmosphere in high latitudes is very large resulting in a positive heat flux from the ocean to the atmosphere. The presence of sea ice reduces this heat flux substantially according to the thickness of the cover. Furthermore, the momentum balance between atmosphere and ocean is modified by the sea ice cover. The individual floes can collide or they are stacked onto each other or they are simply compressed. Finally, the sea ice drift vanishes, when the internal forces in the pack ice are too high. This reduces the momentum flux from the atmosphere to the ocean significantly. When the water temperature is at the freezing point of sea water, sea ice is formed. About two thirds of the salt is rejected initially (AAGAARD AND CARMACK, 1989), because pure water freezes first enclosing small cavities of sea water with high salinity. Most of the salt which remains in the sea ice is subsequently released to the ocean. At the end of a melting season, the salinity of the sea ice is very small, approximately 2 (EICKEN ET AL., 1995). The salt, which is expelled by the sea ice formation, enhances the density of the upper ocean layer. This process is called brine rejection or brine formation. Since the process of sea ice formation separates “pure water” and salt, AAGAARD AND CARMACK (1989) denoted it as a high-latitude analog to evaporation. Both components, the dense water and the sea ice can be transported away from the ice formation region, being on the one hand a source of dense intermediate or bottom water and on the other hand a source of freshwater, when the sea ice is melting. Thus, sea ice formation redistribute the salinity in the polar oceans. Deep water formation is important for the global THC and ice export and associated freshwater fluxes influences the density driven surface circulation and open ocean convection (described in the next section).

2.1.5 Convection

Water mass formation and modification in the Arctic Mediterranean is governed by freezing and melting of ice as well as atmospheric heat fluxes. In the Arctic Ocean, the majority of sea ice is formed in the shelf regions, where the brine rejection increases the salinity in the upper ocean layers and the densified water sinks to the bottom. The salinity characteristics of this water mass vary over time and space, whereas the temperature is mostly close to the freezing point. Parts of the shelf water sinks to intermediate depth, where it mixes with Atlantic Water. Another fraction can sink to the bottom of the Arctic Ocean as Arctic Bottom Water, if the density is high enough and where the bottom topography permits it (NANSEN (1906), Fig. 2.3). Numerical model experiments by BACKHAUS ET AL. (1997) stress the importance of sea ice formation in polynyas^{VII} and the subsequent dynamic removal of ice for the high density of the shelf water. The occurrence of polynyas and the export of ice from the formation region is mostly effected by wind stress. Besides this shelf convection, another source of deep water formation is open ocean or mid-gyre convection. In the Arctic Mediterranean Sea, this is taking place in the Greenland and

^{VII}areas of open water in the sea ice

Norwegian Seas (MALMBERG AND JÓNSSON, 1997). Certain factors are necessary that qualify a region to deep convection. The atmosphere must favour a strong cooling of the surface layers, which is mostly associated with the passage of a low pressure system and cold and dry air masses. The stratification of the sub-surface layers must be weak and the doming of the isopycnals, which accompanies a cyclonic circulation, is necessary to expose the sub-surface layers to the atmosphere. In the Greenland Sea, the brine rejection due to the ice formation increases the surface layer density additionally. Mixing starts where the sinking of dense water is compensated by the upwelling of warm water. The last phase of the convection is sinking and spreading, where the mixed water spreads under the influence of gravity and geostrophy to depth according to its density. A detailed description can be found in the review of MARSHALL AND SCHOTT (1999). AAGAARD AND CARMACK (1989) stress the importance of the salinity stratification at the convection sites, which is highly sensitive to changes in the freshwater flux. Another important site for open ocean convection is the Labrador Sea. The convection process there is similar to that described for the Nordic Seas (see LAB SEA GROUP (1998), LAVENDER ET AL. (2000), LAZIER ET AL. (2002), PICKART ET AL. (2002), RHEIN ET AL. (2002), BÖNING ET AL. (2003); the whole issue of the J. of Physical Oceanography, Vol.32(2) is about the Labrador Sea). Recently, BACON ET AL. (2003) presented evidence for the occurrence of open ocean convection in the Irminger Sea. Convection is important for the ventilation of the oceans and it is an important link in the chain of the THC.

2.2 Variability

The hydrography and processes which were described in the last sections are not constant in time. Variability in the North Atlantic and Arctic Ocean is observed in positions and transports of currents, water mass composition, heat and freshwater transports and distribution and thickness of sea ice. An important mode of variability in the northern hemispheric atmosphere (DESER, 2000) is the North Atlantic Oscillation (NAO) having large impacts on the ocean. In the following sections, a short overview is given on variability in the Arctic and North Atlantic Ocean in general and on the NAO in particular.

2.2.1 NAO

In the year 1924, WALKER published an article, where he classified the monthly sea level pressure (SLP) anomalies of worldwide weather recordings in “Southern Oscillation” and “Northern Oscillation” for the first time. The Northern Oscillation was further separated in two distinct patterns, the “North Atlantic Oscillation” (NAO) and the “North Pacific Oscillation” (STEPHENSON ET AL., 2003). WALKER recognised that an enhanced pressure difference between the Azores and Iceland in the winter season influenced the Gulf Stream, the air temperatures over Scandinavia and Greenland and the sea ice dynamics in the North Atlantic. The seesaw of the mean winter temperature between

Greenland and northern Europe has been known since the 18th Century (VAN LOON AND ROGERS, 1978). Basically, the NAO is a teleconnection pattern^{VIII} of the Northern Hemisphere with two centres of action: the Iceland Low and the Azores High. The NAO is often viewed as a zonally asymmetric SLP distribution over the North Atlantic Ocean. The corresponding SLP pattern of the NAO was defined by WALLACE AND GUTZLER (1981) with the help of one point correlation maps, where the NAO is identified by regions of maximum negative correlation. Another possibility is to use rotated empirical orthogonal functions (rotated EOFs) as shown by BARNSTON AND LIVEZEY (1987). The authors found that the NAO is the only teleconnection pattern in the Northern Hemisphere, which is present throughout the year, and it accounts for more than one-third of the total variance of the SLP field during the winter season. Recently, THOMPSON AND WALLACE (1998) presented an EOF analysis of the SLP anomaly field north of 20°N, comprising the whole Northern Hemisphere and not only the North Atlantic sector. The resulting pattern and its first principal component were called the Arctic Oscillation (AO), or lately the Northern Hemisphere Annular Mode (NAM) (THOMPSON ET AL., 2003). The NAM includes not only the centres of action (Iceland and Azores), but it is a meridional dipole in SLP which comprises the fluctuations of the Arctic basin and the surrounding zonal ring (THOMPSON ET AL., 2003). Additionally, the NAM index is more strongly coupled to the Eurasian winter surface air temperature than the NAO index (THOMPSON AND WALLACE, 1998). On the other hand DESER ET AL. (2000) stated, that there was only a weak correlation between the North Atlantic and North Pacific sector and thus the NAM could not be a teleconnection pattern. This conclusion was supported by AMBAUM ET AL. (2001) and MONAHAN ET AL. (2000). However, the differences between the NAO and the NAM are still the subject of ongoing discussions.

The temporal evolution of the NAO index is not unique and several definitions circulate in the literature. ROGERS (1984) defined the NAO index as the difference between the normalised SLP anomalies at the Azores and Iceland on the basis of December to February mean values. Later on, HURRELL (1995) used the mean winter (December to March) SLP anomalies between Portugal and Iceland to define the NAO index. The SLP anomalies at each station were divided by the long term standard deviation for the normalisation. A third NAO index was introduced by JONES ET AL. (1997), who took the SLP difference from Gibraltar to Iceland to calculate the index according to the method of HURRELL (1995). The temporal evolution of the NAO was investigated by several authors, which were summarised by GREATBATCH (2000). As discussed in the introduction, WUNSCH (1999) found indications for a weak red behaviour of the NAO time series spectrum. Apart from the red behaviour, the spectrum reveals some very weak structures near periods of 2 and 8–10 years. Therefore, the term oscillation is misleading, as the spectrum looks more like a random process (GREATBATCH, 2000; STEPHENSON ET AL., 2003). It is still an open question what are the reasons for the multidecadal vari-

^{VIII}Teleconnection patterns are simultaneous variations in climate, often of opposite sign, distributed over large distances (WALLACE AND GUTZLER, 1981; BARNSTON AND LIVEZEY, 1987)

ability of the NAO. The coupling between the atmosphere and the ocean with its large heat capacity could be an important factor in modulating the NAO variability (CZAJA ET AL., 2003; VISBECK ET AL., 2003).

As GREATBATCH (2000) stated, the geostrophic balance is the reason for stronger than usual westerly winds across the North Atlantic in years of high NAO index, and in low index years, the westerly winds are weaker than usual. This has large impacts on the climate over Europe and North America as already pointed out by WALKER (1924) and WALKER AND BLISS (1932). There are numerous known impacts of the NAO on the North Atlantic Ocean, which will be sketched in the following.

The convection is very sensitive to changes of the atmospheric conditions and DICKSON ET AL. (1996) investigated the influence of the NAO on the convection. The authors found that during the NAO minimum in the 60s, the convection in the Greenland and Sargasso Seas was at a maximum, while convection in the Labrador Sea was weak. With increasing NAO in the 80s and 90s, all convection sites evolved to their opposite extreme. Therefore DICKSON ET AL. (1996) concluded that the production of deep water in the Labrador and Greenland Seas was influenced by the NAO. The weak convection in the Labrador Sea was also found by LAZIER (1988), who assumed that it was caused by the GSA (see Section 2.2.3 below). CURRY ET AL. (1998) found a 2–4 year time lag between the NAO and the thickness of the LSW layer. Declining NAO led the thinning and warming of the LSW and vice versa. The time lag between the NAO and temperatures of the deep ocean at Bermuda was approximately 6 years. Further large scale effects were the weakening of the Gulf Stream and the NAC in times of low NAO (in the 60s) and a subsequent acceleration with high NAO index, with highest transport values in the 90s (CURRY AND MCCARTNEY, 2001). The production of LSW and Subtropical Mode Water (STMW) was investigated by JOYCE ET AL. (2000) and MARSH (2000). In periods of positive NAO index, the Gulf Stream shifted to a northerly position and the production of STMW and LSW was enhanced. BERSCH ET AL. (1999) found in annually repeated hydrographic section between Ireland and Greenland, that the Subarctic Front retreats to the west over the Iceland Basin between 1995 and 1996, accompanied by an increase in the salinity of the Subpolar Mode Water east of the Reykjanes Ridge and a decrease in salinity to the west in the Irminger Basin. In the western part of the North Atlantic Ocean, the upper ocean was anomalously warm in the winter 95/96 (REVERDIN AND VERBRUGGE, 1999). The authors analysed monthly repeated hydrographic sections between Iceland and Newfoundland and concluded that the heat fluxes at the surface alone could not explain the warming, thus changes in lateral advection of heat must also have been important. Additionally, the deep convection in the Labrador Sea was reduced in the second half of the nineties LAZIER ET AL. (2002). A basin wide response was found by ESSELBORN AND EDEN (2001) in sea level height. Sea level raised by about 6 cm in the subpolar gyre and dropped by the same amount in the subtropical gyre due to changes of the meridional heat transport.

CAYAN (1992) showed that the NAO is responsible for large scale patterns of air–sea

fluxes and SST in the North Atlantic. Other observational studies also found a connection between the SST anomalies and the atmospheric fields (DESER AND BLACKMON, 1993; KUSHNIR, 1994). On time scales less than ten years, the SST reacted only passively to the atmospheric forcing, whereas on longer time scales, the internal variability of the ocean drove the anomalies. SST anomalies were tracked from the North American coast to the Nordic Seas by SUTTON AND ALLEN (1997), who proposed a regular period of 12–14 years for this propagation. The time scale is comparable to the results of DESER AND BLACKMON (1993). The winter-to-winter persistence of the SST anomalies could be explained with the Namias–Born mechanism (NAMIAS AND BORN, 1970; ALEXANDER AND DESER, 1995): the anomalies are capped by the shallow summer mixed layer and reemerge in the following winter, when the summer mixed layer is eroded.

Several model studies investigated the influence of the NAO on the North Atlantic Ocean. A 40 year hindcast integration was accomplished by HALLIWELL (1998). In the region of the Gulf Stream, SST anomalies were simulated with basin scale atmospheric forcing, whereas the cooling of the subpolar gyre in the 70s was not accounted for. A comparable integration with a different model was performed by HÄKKINEN (1999b). In this study, the THC and the meridional heat transport were very strong in the 80s and 90s. The response to the atmospheric forcing fields were basin wide and found on decadal and interdecadal time scales, following closely the evolution of the NAO index. EDEN AND WILLEBRAND (2001) found that a large part of the variability of the ocean could be explained by the NAO. The reactions to onsetting positive NAO conditions are a fast barotropic response with substantially decrease northward heat transport near the subpolar front and a delayed baroclinic response with enhanced northward heat transport to the subpolar North Atlantic. On the basis of an NAO index, which started in the year 1865, EDEN AND JUNG (2001) reconstructed the atmospheric forcing for an ocean only model. In their integration, the SST anomalies were not caused by advection with the mean circulation but imposed by the overlying atmosphere. The interdecadal changes of the North Atlantic Ocean were mainly driven by the THC and the NAO, which is in agreement with KUSHNIR (1994). Comparable model analyses of VISBECK ET AL. (1998) and DELWORTH AND GREATBATCH (2000) agreed with the hypothesis that the SST anomalies in the North Atlantic Ocean do not force the NAO directly. A coupled air–sea mode on interdecadal time scales between the NAO and the Atlantic THC was proposed by TIMMERMANN ET AL. (1998).

A review on the NAO was written by GREATBATCH (2000). Recently, a monograph was published solely about the NAO (HURRELL ET AL., 2003). It comprises the state of the art knowledge of the nature of the NAO and its implications on the environment.

2.2.2 Variability in the Arctic Mediterranean

The inhospitable environment in the Arctic Mediterranean is the reason why sea ice conditions are so difficult to observe. Thus, only sparse observation were available until the late 70s. Since 1978, the data situation improved substantially with the passive mi-

crowave data from satellites. Sea ice extent and concentration can now be deduced over large areas. The interannual variability of sea ice extent and thickness in the Arctic Ocean has been a controversial issue in the last years, because it has been attributed to global warming, but this is still under investigation. Numerous publications have been dealing with this variability. Here, only a short overview will be given.

The average seasonal cycle of sea ice extent in the Northern Hemisphere has its minimum of $7.0 \times 10^6 \text{ km}^2$ in September (PARKINSON ET AL., 1999). In September, only the “inner” Arctic Ocean (not the shelf seas) is covered with sea ice. During winter the sea ice extent increases to a maximum of $15.4 \times 10^6 \text{ km}^2$ in March of which 14% is open water. In that month, the sea ice covers the entire Arctic Ocean, and large parts of the Barents Sea, the Greenland Sea and the Labrador Sea.

The largest variability of Arctic sea ice occurs within the annual cycle, but interannual variation can amount to about one third of the seasonal cycle (LEMKE ET AL., 1980). Generally, the variability is larger in summer, when the sea ice extent is not blocked by the land masses. WALSH AND JOHNSON (1979) investigated the interannual variability of sea ice extent over a period of 25 years and found fluctuations of 5° latitude in summer and also in winter. In the study of LEMKE ET AL. (1980), a retreat of the ice extent by 0.4% per year was pointed out. A decrease of summer sea ice extent in the years 1961 - 1990 became apparent in the study of CHAPMAN AND WALSH (1993), with minima in the years 1977, 1981 and 1990. Analysis of the total ice extent confirmed the reduction of Arctic sea ice extent by 3% since 1978 (CAVALIERI ET AL., 1997; JOHANNESSEN ET AL., 1999; VINNIKOV ET AL., 1999; SERREZE ET AL., 2000). A comparison of observations and data from a climate model led VINNIKOV ET AL. (1999) to the conclusion, that the decrease is stronger than model results suggested, which were driven by natural variability only. Climate model experiments which included anthropogenic forcing were able to produce a decrease of sea ice extent in the observed magnitude.

The inflow of warm Atlantic Water to the Arctic Ocean varies also over time, which could be a reason for the reduction of the sea ice extent (RIGOR ET AL., 2000). The first observed warming event in the early 90s was associated with an increase of the NAO to a positive period (GROTEFENDT ET AL., 1998). DICKSON ET AL. (2000) combined numerous atmospheric and oceanic observations and concluded that the warming event is a combination of warmer and stronger inflow of Atlantic Water and directly the effect of the NAO. A detailed study of the warming event with a numerical model revealed, that there is a connection between the high NAO state and the warmer Atlantic Water, but the inflow in the Arctic Ocean itself is not steady and modified by the local current systems (KARCHER ET AL., 2003). Another major change in the Arctic Ocean, which was attributed to the NAO index is the retreat of the cold halocline (STEELE AND BOYD, 1998). The authors found an increase of salinity in the halocline layer in the eastern Eurasian Basin in the early 90s.

Sea ice thickness is even more difficult to measure than sea ice concentration. SHY AND WALSH (1996) combined drifting buoy data and submarine-based sonar data and

found significant interannual variability at the North Pole, but no systematic decrease of ice thickness. Later on, [ROTHROCK ET AL. \(1999\)](#) and [WADHAMS AND DAVIS \(2000\)](#) reported an decrease of the average sea ice thickness in the Arctic Ocean by more than 40% in the last decades. For these studies, several submarine cruise were used. Contrarily, soundings from six different submarine cruises, which were analysed by [WIN-SOR \(2001\)](#), showed almost no trend. [HILMER AND LEMKE \(2000\)](#) investigated the decrease of Arctic sea ice volume with a sea ice model and concluded that the long-term change of [ROTHROCK ET AL. \(1999\)](#) is overestimated, as these observations could not capture the strong decadal variability. [HOLLOWAY AND SOU \(2002\)](#) compared the observed sea ice thickness with model results and concluded that the reported decrease is not an Arctic-wide phenomenon and not as large as proposed. An undersampling of the areas of the major variability, especially the Canadian sector of the Arctic Ocean, and infrequent cruises led to these interpretations. The model results showed an increasing volume from the 50s to the 60s, followed by 20 years with decadal variability and no apparent trend. Thinning of the sea ice occurred from the early 80s to the early 90s, with a steep decline after the mid 90s. The total sea ice volume had the same value in the year 1950 and 2000. The reason for the thinning was attributed to shifts in ice motion patterns and warmer atmospheric temperatures. This agrees with the results of [KÖBERLE AND GERDES \(2003\)](#). In this study, a long term warming trend for the period 1948–1998 could not be recognised, but the authors found a large decline of ice volume in the years 1965–1995. Long-term trends were masked by decadal and interdecadal variability. The question why the sea ice cover is thinning in general, was posed by [BITZ AND ROE \(2003\)](#). They found that thin ice reacts less sensitive to climate perturbation, because of a negative feedback loop: sea ice growth depends inversely on its thickness. The retreat of the sea ice margin is slowed down due to the negative feedback, but the ice gets thinner.

An early estimate of sea ice motion in the Arctic Ocean was done by [COLONY AND THORNDIKE \(1984\)](#), who analysed trajectories of buoys. The data revealed two main features: the ice drift due to the TPD and the anticyclonic ice drift with the Beaufort Gyre. A study with an idealised model by [PROSHUTINSKY AND JOHNSON \(1997\)](#) discerns between a cyclonic and an anticyclonic wind-driven motion in the Arctic Ocean, each with a persistence of five to seven years. In the cyclonic years, the Beaufort Gyre is substantially weakened and confined to the North American coast, or the Beaufort Gyre is completely absent, being dispelled by a cyclonic circulation in the central Arctic Ocean. In anticyclonic years, the typical circulation evolves (Fig. 2.2). Observations confirm the weakening of the Beaufort Gyre in the years 1988 - 1995, which is a cyclonic period after [PROSHUTINSKY AND JOHNSON \(1997\)](#) ([KWOK, 2000](#)). At the same time, the eastward sea ice transport from the Laptev Sea is enhanced, but the TPD is weakened. The ice export through Fram Strait is increased as well as the import through BSO and Kara Seas; the sea ice extent in the Nordic Seas is reduced. These changes are attributed to the NAO, which is in a positive phase in the relevant years. The results for the Arctic Ocean were confirmed by a model analysis of [ZHANG ET AL. \(2000\)](#). Observations of the ice ex-

port through Fram Strait revealed also significant year-to-year variations (VINJE ET AL., 1998). Strong correspondence between this export and the NAO was stated by DICKSON ET AL. (2000). A numerical hindcast study by HILMER AND JUNG (2000) dealt directly with the Fram Strait ice export. The authors found a high correlation between the ice export and the NAO index after 1977, but not in the years before. An analysis of the SLP revealed an eastward shift of the NAOs centres in this last 20 years, resulting in anomalous southward wind stresses over the Fram Strait. The influence of the enhanced cyclonic wind stress over the eastern Arctic Ocean on the Fram Strait ice export was confirmed by KÖBERLE AND GERDES (2003), but according to these authors, the presence of thick ice from a previous accumulation phase is equally important for an ice export event. DICKSON ET AL. (2000) summarised the variability in the Arctic Ocean, which can be attributed to the NAO. A more general overview of the changes in the northern high-latitude environment is written by SERREZE ET AL. (2000).

2.2.3 GSA

A minimum in sea surface salinity was observed in the years 1965 to 1982 at various locations of the subpolar North Atlantic. An “advective” explanation was suggested for this phenomenon and elaborated in detail by (DICKSON ET AL., 1988), who named it the “Great Salinity Anomaly” (GSA). The salinity anomaly was first observed northeast of Iceland, then crossing the Denmark Strait to the Labrador Sea, returning to the Norwegian Sea with the North Atlantic Current and vanishing in the Greenland Sea. Alternative hypothesis of the causes of the GSA were the shift of the Subpolar Front or the variability in water mass transports. BELKIN ET AL. (1998) summarised observations and theories and described another GSA passing the subpolar North Atlantic in the 80s and a further one in the 90s. According to BELKIN ET AL. (1998), the spreading of the 80s and 90s anomalies happened in a similar fashion as the GSA of the 70s and could also be explained by an advection mechanism. The origin of the anomalies are different from each other. The early anomaly of the 70s was triggered by a freshwater and sea ice pulse from the Arctic Ocean via Fram Strait (AAGAARD AND CARMACK, 1989). Several studies ascribed the large ice export event and the negative salinity anomaly in the Nordic Seas to atmospheric forcing (DICKSON ET AL., 1988; WALSH AND CHAPMAN, 1990; SERREZE ET AL., 1992). POLLARD AND PU (1985) suggested that the GSA resulted from changes of the evaporation-precipitation balance over the Greenland Sea. This was disproved by DICKSON ET AL. (1988), who concluded that the salt deficit was far too large to be initialised by the net precipitation. The analysis of sea ice concentrations and SLP fields by SLONOSKY ET AL. (1997) supports the theory, that large scale atmospheric patterns caused the GSA, but on interannual time scale, the sea ice anomalies led the atmospheric anomalies. The 80s and 90s anomalies were the local response of the Labrador Sea and Baffin Bay to severe winters. Several model studies were investigating the sources and pathways of the salinity anomalies and their impact on the THC (see HÄKKINEN (1993, 1999a, 2002); HAAK ET AL. (2003) for details).

2.2.4 Oscillations in ocean models

Many model studies of the ocean circulation are performed with simplified models, e.g. box models, models with very simplified topography or coarse resolution models. The main constraint is the computer capacity and thus surface boundary conditions are prescribed or simplified, instead of using a fully coupled ocean–atmosphere model.

Numerous model experiments investigated the stability of the thermohaline circulation to abrupt or long term changes of the surface thermohaline forcing. This is important to understand e.g. the oceanic circulation during the Last Glacial Maximum and natural climate variability in general. On the other hand, those experiments were used to integrate climate model and generate future climate scenarios. In this section, the main focus is on oscillations in ocean models and their causes.

A first study on the significance of mixed boundary conditions^{IX} was conducted by STOMMEL (1961) with a box model of the ocean (see also WELANDER, 1986). Two well mixed boxes represented the low and high latitude ocean, which were connected by an upper and lower hydraulic link (exchange of fluid according to the density difference). When the thermal response time was shorter than the haline one (mixed boundary conditions), two stable steady states existed: either a fast loop, which is thermally driven (strong poleward heat transport), or a slow haline driven loop (weak equatorward heat transport without sinking at the cold and fresh high latitudes). BRYAN (1986) investigated the impact of mixed boundary conditions on the ocean circulation. He used a coarse resolution model, which was symmetric at the equator. Sinking occurred at high latitudes and upwelling in the rest of the ocean. After a spin up calculation, the mixed boundary conditions were perturbed with an additional freshwater input at high southern latitudes. The consequence was a capping of the sinking region by a halocline and a single cell pole-to-pole circulation evolved over a time scale of 50 years. This result was called “halocline catastrophe”. Surprising was the time scale of the event, which was much less than the expected adjustment time scale of the THC (about 1000 years). The lateral friction acting on the THC was hold responsible for this. Analogue model experiments with a simplified model were conducted by WEAVER AND SARACHIK (1991a,b). Changing the surface forcing from restoring to mixed boundary conditions caused an adjustment process with variability on decadal to centennial time scales. The reason for the decadal oscillation (9 years) was the advection of warm and saline anomalies with the western boundary current, which ended in the subpolar gyre, where the deep water formation was increased. The magnitude of the surface freshwater flux was important for this oscillation (WEAVER ET AL., 1993); increasing the surface freshwater flux generated an oscillation with a time scale of 15–20 years. YIN AND SARACHIK (1995) proposed an advective and convective mechanism for a similar decadal oscillation. A more refined but still simplified model of the North Atlantic Ocean revealed an oscillation of about 20 years (WEAVER ET AL., 1994). The mechanism involved an interplay between the zonal pressure gradient and the meridional overturning in the Labrador Sea; neither the surface freshwater forcing

^{IX}SST is restored and salinity flux prescribed

nor the wind-driven gyre circulation was held responsible for that oscillation. A comparable decadal oscillation was found by [WEISSE ET AL. \(1994\)](#) in a global model with stochastic freshwater flux perturbation, but the mechanism differed. The Labrador Sea accumulated the surface freshwater flux and was flushed on time scales of 10 to 40 years. The resulting freshwater pulse was advected to the subpolar North Atlantic, where the deep water formation was reduced. Variability on longer time scale (approximately 350 years) was found by [MIKOLAJEWICZ AND MAIER-REIMER \(1990\)](#) with a global ocean model which was forced with stochastic freshwater flux forcing. The oscillation was sustained by the long residence time of salinities anomalies, which could be followed at the surface to the convection sites in the North Atlantic, where they influenced the deep water formation and further along the entire loop of the meridional overturning, surfacing again the Southern Ocean. The variability was therefore salinity driven and involved changes in the transport of the ACC (Antarctic Circumpolar Current) and the thermohaline circulation of the Atlantic. The authors concluded later on, that the time scale was shortened artificially by the type of surface boundary condition they used ([MIKOLAJEWICZ AND MAIER-REIMER, 1994](#)); with the corrected surface boundary conditions, the time scale was about 500 years. Similar response time scales (200–300 year) were found by [MYSAK ET AL. \(1993\)](#) with an zonally averaged, one basin ocean model. The forcing consisted of random freshwater fluxes, which produced an oscillation in the overturning. [DELWORTH ET AL. \(1993\)](#) integrated the GFDL coupled ocean–atmosphere model for 600 years and showed the presence of distinct variability of the THC^x in the North Atlantic with a time scale of about 40–60 years. The spectrum of the model variability was on shorter time scales very similar to observation at the Ocean Weather Ship India. The mechanism is driven by SST anomalies in the sinking region and fluctuations in the heat and salt transport associated with the horizontal circulation. A major constraint of the model is the flux correction between the atmosphere and the ocean model, which could act as an additional forcing and produce nonlinear interactions. The authors concluded that the variability is mainly driven by internal oceanic processes. This is one of the main questions regarding the variability of oceanic processes: whether the ocean is capable of sustaining an internal variability with a purely stochastic forcing from the atmosphere or whether the variability of the THC is the results of a coupled air-sea interaction. A similar oscillation was found by [GREATBATCH AND ZHANG \(1995\)](#) in an ocean model of an idealised North Atlantic with a period of 50 years. The ocean model was driven by constant, zonally uniform surface heat flux. According to the authors adding surface salt forcing weakened the oscillation and thus the phenomenon was primarily thermally driven. A work of [WEAVER AND VALCKE \(1998\)](#) reanalysed the variability of the THC in the GFDL coupled model and the authors concluded that the “interdecadal variability in the GFDL model is not an ocean-only mode and that it must exist as a coupled

^xThermohaline circulation denotes the global ocean circulation which is driven by temperature and salinity differences; often used in the same sense as meridional overturning in the North Atlantic as in [DELWORTH ET AL. \(1993\)](#)

phenomenon". A recent analysis of [DELWORTH AND GREATBATCH \(2000\)](#) contradicts this statement. According to their results, the variability of the THC is the response of the ocean to the surface flux forcing. A coupled air-sea mode is not necessary, but the coupling of ocean and atmosphere can change the amplitude and time scale of the variability. [TIMMERMANN ET AL. \(1998\)](#) found variability of the THC with a time scale of about 35 years in the coupled model of the Max Planck Institute (MPI). They related it to the presence of an extratropical air-sea coupled mode. While the mechanisms of the variability of the THC differ between the GFDL and MPI model, there are similarities in the modelled SST and SSS anomaly patterns in the North Atlantic, which are resembling the observed SST anomalies by [KUSHNIR \(1994\)](#).

3 Model description

The notation “model” in a physical context can be a somewhat misleading, because it is usually used for other, more substantial, concepts. For instance, a model of a train in toy train set or the model of a planned building. Nevertheless, all models have some features in common: they are simplifications and idealisations of reality. This, too, applies to physical models, which are used to simplify complex processes and aim at providing conceptual statements. On the one hand, there are conceptual models, which combine known facts in a wider, logical frame. On the other hand, there are highly developed computer models of physical context. They try to grasp as many relevant processes as possible to predict what is going to happen in the future. The spectrum between these extrema covers a wide range of models. The choice of model to be used depends on the problem which is to be addressed.

In this study, the main interest is the response of the ocean and sea ice to changes in the atmosphere. Thus, a model of intermediate complexity is chosen as the tool to conduct the experiments. It is a non eddy-resolving ocean model with a coarse resolution, which is coupled to a sea ice model with the same resolution. Practical reasons led to this choice as the computational expenses for decadal scale experiments lie in the range of a few weeks. The higher the resolution and/or the complexity of the model, the more expensive are these computing costs. Another equally important argument for coarse resolution is the reduced internal oceanic variability. In high resolution, eddy-permitting models, this internal variability is present at all time scales. The scope of this study is the response of the ocean–sea ice component to the time dependent signal forced by the atmosphere, which is hard to separate from any internal variability. As shown in previous studies carried out using the same model, it is capable of capturing the main circulation of the northern North Atlantic and Arctic Ocean reasonably well (GERDES AND KÖBERLE, 1995; GERDES AND SCHAUER, 1997). The atmosphere is represented by heat and fresh-water fluxes and therefore no feedback of the ocean–sea ice system to the atmosphere is possible. In this chapter, the basic equations of the two model components, ocean and sea ice, are introduced along with their numerical realisation. The setup of the models is explained in detail, as are the initial data, which are necessary for the experiments.

3.1 Ocean model

The experiments presented in this study are performed with the low resolution model (LRM) of the NAOSIM (North Atlantic Ocean Sea Ice Models) hierarchy of ocean–sea

ice models maintained at the Alfred Wegener Institute (KÖBERLE AND GERDES, 2003; KAUKER ET AL., 2003). Its oceanic component is based on the second version of the “Modular Ocean Model” (MOM-2) developed at the “Geophysical Fluid Dynamics Laboratory” (GFDL) in Princeton (PACANOWSKI, 1995), a general circulation model of the ocean. Primitive equation models of the GFDL type are widely used for large scale applications in simulating the North Atlantic Ocean and have been described BRYAN (1969), COX (1984) and PACANOWSKI (1995). The main equations will be outlined in section 3.1.1 and the actual model configuration employed in 3.1.2.

3.1.1 Equations

The model integrates the primitive equations derived from the Navier-Stokes equations (momentum conservation) and the conservation equations of energy, mass and salt (see MÜLLER AND WILLEBRAND, 1989).

To apply these equations to the earth system, they have been formulated in a rotated coordinate system with spherical coordinates. The spherical approximation is a first approximation, which treats geopotential surfaces as spherical. Further approximations are the *thin shell approximation* (the ocean depth is much less than the earth’s radius) and the *aspect ratio approximation* (the scale of vertical motion is smaller than the horizontal scale). Minor density variations are neglected when they affect inertia but retained when they affect buoyancy (*Boussinesq approximation*). The *hydrostatic approximation* assumes that the vertical pressure gradient is solely caused by density. Surface gravity and sound waves are excluded due to the *rigid-lid* and *hydrostatic* approximation. Reynolds averaging neglects the molecular fluxes and parametrises the eddy fluxes. Strictly, this is valid only for motions and regions where a distinct spectral separation between the mean flow and the turbulent motion exists. The primitive equations comprise four prognostic equations (the two horizontal components of the momentum equation, the thermodynamic equation of energy and the salinity equation) and three diagnostic equations (the continuity equation, the hydrostatic equation and the equation of state). A more detailed description of the approximations can be found in the work of MÜLLER AND WILLEBRAND (1989).

The whole set of primitive equations in spherical coordinates reads as follows:

$$u_t + \mathcal{L}(u) - \frac{uv \tan \phi}{a} - fv = -\frac{p_\lambda}{\rho_0 a \cdot \cos \phi} + (\kappa_m u_z)_z + F^u \quad (3.1)$$

$$v_t + \mathcal{L}(v) + \frac{u^2 \tan \phi}{a} + fu = -\frac{p_\phi}{\rho_0 a} + (\kappa_m v_z)_z + F^v \quad (3.2)$$

$$T_t + \mathcal{L}(T) = (\kappa_h \cdot T_z)_z + \nabla \cdot (A_h \nabla T) \quad (3.3)$$

$$S_t + \mathcal{L}(S) = (\kappa_h \cdot S_z)_z + \nabla \cdot (A_h \nabla S) \quad (3.4)$$

$$w_z = -\frac{1}{a \cos \phi} \cdot (u_\lambda + (\cos \phi \cdot v)_\phi) \cong \mathcal{L}(1) = 0 \quad (3.5)$$

$$p_z = -\rho \cdot g \quad (3.6)$$

$$\rho = \rho(T, S, p) \quad , \quad (3.7)$$

with the latitude λ set to zero at the equator and ± 90 at the North/South Pole. ϕ denotes the longitudinal direction starting with zero at Greenwich eastward positive, depth z is positive upwards defined with zero at ocean surface and a is the mean radius of earth.

The horizontal friction terms (F) and the advection operator ($L(\alpha)$) are given by

$$F^u = \nabla \cdot (A_m \nabla u) + A_m \left[\frac{(1 - \tan^2 \phi) \cdot u}{a^2} - \frac{2 \sin \phi \cdot v_\lambda}{a^2 \cos^2 \phi} \right] \quad (3.8)$$

$$F^v = \nabla \cdot (A_m \nabla v) + A_m \left[\frac{(1 - \tan^2 \phi) \cdot v}{a^2} + \frac{2 \sin \phi \cdot u_\lambda}{a^2 \cos^2 \phi} \right] \quad (3.9)$$

$$L(\alpha) = \frac{(u\alpha)_\lambda}{a \cdot \cos \phi} + \frac{(\cos \phi \cdot v \cdot a)_\phi}{a \cdot \cos \phi} + (w \cdot \alpha)_z \quad . \quad (3.10)$$

Here u, v, w are the zonal, meridional and vertical velocity components, T and S are potential temperature and salinity, t is time, p is pressure, ρ is the in situ density with ρ_0 as reference density, g is the mean acceleration due to gravity (980.6 cm/s^2), κ_m and κ_h are the vertical eddy viscosity and diffusivity coefficients, A_m and A_h are horizontal eddy viscosity and diffusivity coefficients and $f = 2\Omega \sin \phi$ is the Coriolis parameter, where Ω is the angular velocity of the earth. The independent variables in the subscripts denote partial derivatives with respect to those variables.

The horizontal velocities (u, v) can be divided into a depth independent or external mode representing the barotropic flow (\bar{u}, \bar{v}) and the internal, baroclinic mode (u', v'). Due to the rigid lid approximation ($w = 0$ at $z = 0$), the external mode is horizontally non-divergent and can be expressed by a streamfunction.

To solve the equations numerically, they are discretized by finite difference techniques into a three dimensional lattice of rectangular shaped cells of arbitrary size, which represent the ocean volume (BRYAN, 1969). In case of MOM 2, the Arakawa B grid formulation is used (MESINGER AND ARAKAWA, 1976). Its layout is shown in Fig. 3.1. The scalar components are solved at the crossing of grid lines, marked by (h) in Fig. 3.1, whereas both vector velocities are calculated on a grid which is shifted in the zonal and meridional directions by half a grid cell each. In the vertical, the scalar components and the horizontal velocities are defined on the same layer, while the vertical velocity points (w) are shifted vertically by half a grid cell.

The physics outlined above is the backbone of the model. Apart from that, the model structure allows one to choose between differing representations of physical processes (e.g. for boundary conditions) as well as for numerical methods. The name MOM is the abbreviation for *Modular Ocean Modelling*, which should emphasise this flexibility. To address specific problems, it is necessary to provide initial conditions for the parameters and to specify boundary conditions. This will be done in section 3.3. In the following section, the setup used in this work is described.

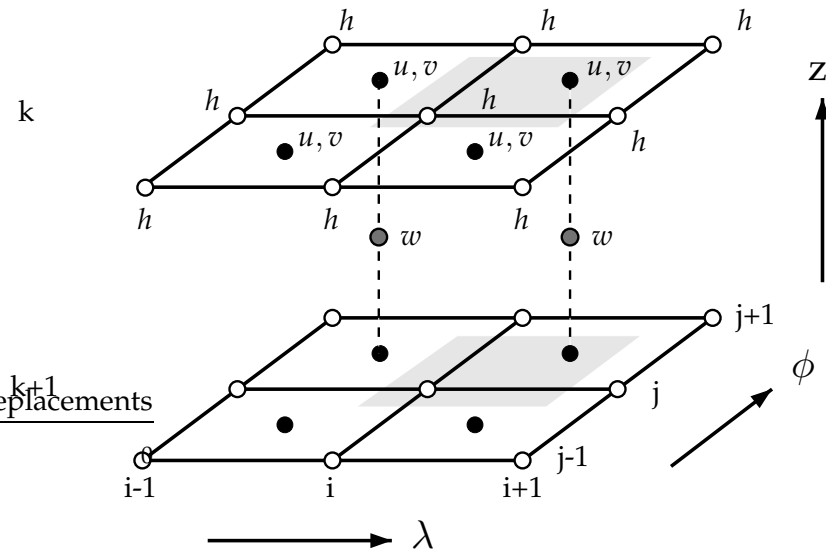


Figure 3.1: Sketch of the Arakawa B grid in spherical coordinates; the shaded areas mark tracer (h) and vector points (u, v, w) at (i, j)

3.1.2 Setup

The model domain includes the entire the Arctic Ocean and extends into the Atlantic Ocean to approximately 20°S and has a horizontal resolution of $1^\circ \times 1^\circ$. The depth is discretized with 19 non-uniformly spaced vertical levels. The thickness of these layers increases from 20m at the surface smoothly to 800m near the bottom (Fig. 3.2). The resolution of the upper layers is high to allow a good representation of the vertical structure of the major currents.

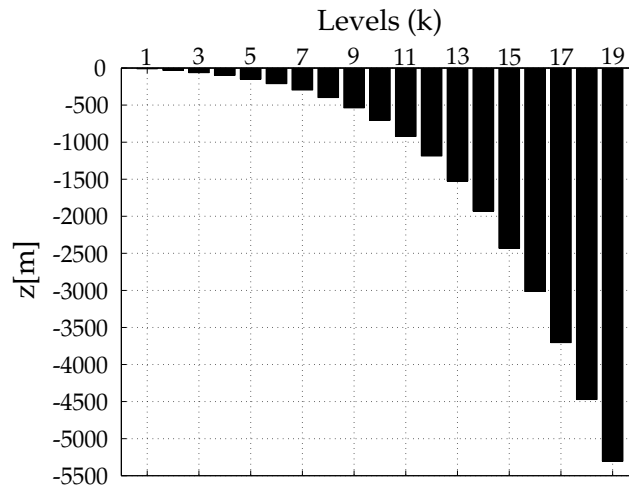


Figure 3.2: Depth levels of the scalar points, denoted as “ k ” in Fig. 3.1

The topography was box-averaged from the NOAA (1988) data set of the National Geophysical Data Center by KÖBERLE AND GERDES (2003). In addition to the averaging, the Denmark Strait and the Faeroe Bank Channel were virtually dug out to achieve a realistic throughflow. Furthermore, the Davis Strait, which could not be resolved by the standard averaging procedure, was opened artificially to allow an exchange between the Arctic Ocean and the Labrador Sea. The resulting topography is shown in Fig. 3.3.

The model grid is rotated to avoid the pole singularity such that the grid equator coincides with the geographical 30°W meridian and the pole lies at 60°E on the geographical equator. All boxes are approximately 100 km×100 km, and irregular resolution due to convergence of the meridians is prevented. At the southern boundary at 20°S open boundary conditions are implemented, following the approach of STEVENS (1991), with prescribed inflow of temperature and salinity with a time constant of 30 days towards climatological values (LEVITUS ET AL., 1994). The outflow of tracers is ensured, combined with a radiation condition for the waves. The baroclinic part of the horizontal velocity at the open boundary is calculated from a simplified momentum balance while the barotropic velocities normal to the boundary are specified by annual mean values of the streamfunction of the vertically integrated flow taken from the FLAME 4/3° Atlantic ocean model (DIETERICH, 2003). The Strait of Gibraltar and the Bering Strait are closed. The horizontal velocities parallel and perpendicular to these boundaries and along all other lateral boundaries are set to zero, which is called a “no-slip” condition.

At the bottom, the “free-slip” condition for the horizontal velocity is used (i.e. $\kappa_m \vec{u}_z = 0$). The bottom drag coefficient, c_d , is set to zero.

A distorted physics scheme was used as introduced by BRYAN (1984). This deals with the fact, that there is a wide range of time scales in the ocean reaching from high frequency waves like internal gravity or Rossby waves down to ultra low frequencies associated with slow diffusion of water mass properties below the main thermocline. Hence, calculations would take a long time to reach an equilibrium solution¹. Distorted physics compresses the frequency band of the ocean model by slowing down gravity and Rossby waves. This is accomplished by choosing a different time step for the external mode, the internal mode and the tracers. Baroclinic instabilities have a reduced growth rate, but they are present over a wider range. Since only the local time derivative is changed, the results should correspond to the non-distorted equilibrium solution, at least for coarse resolution models and for problems which only have one solution (BRYAN, 1984). In this setup, the external and internal time scales are set to one hour, whereas the time step for the tracer equations (3.3 and 3.4 respectively) is six hours. No abyssal acceleration is employed. All chosen parameters are listed in Tab. 3.1. The tracer time is the model time.

The discretisation of the time derivative in the momentum and tracer equations follows the *leapfrog scheme*, which applies a central step in time (for a detailed explanation see MESINGER AND ARAKAWA, 1976). An Euler backward step is added every 17th time

¹This is a quite subjective term, because equilibrium depends on the processes which are important for the experiment. Advective adjustment, for example is faster than diffusive.

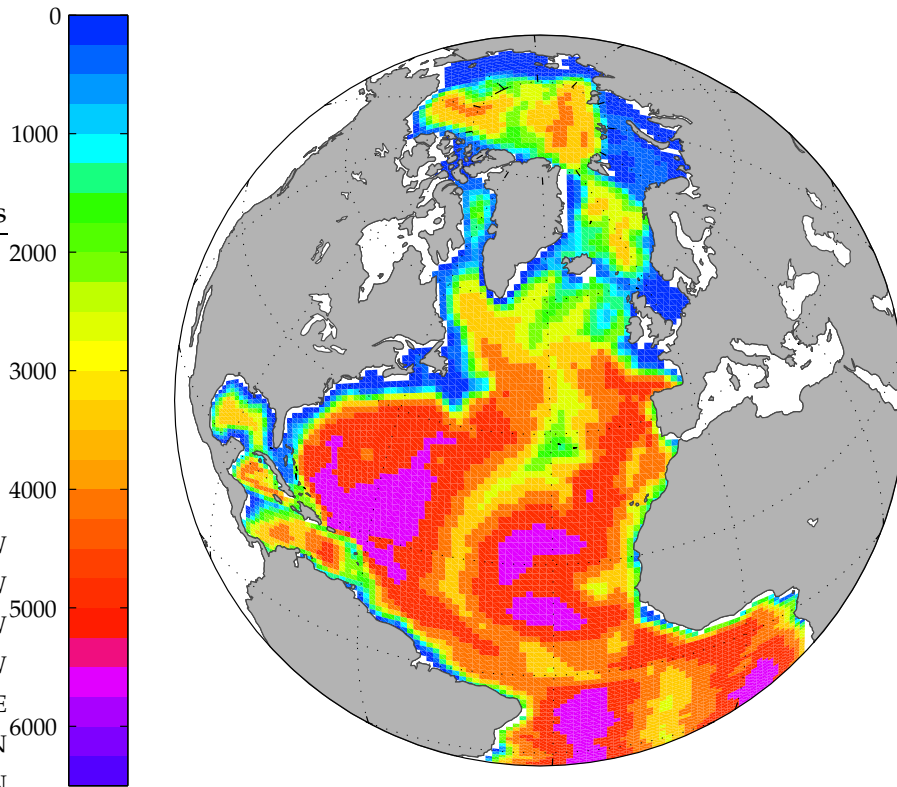


Figure 3.3: Model topography, depths in metres

step to prevent a strong divergence from the physical solution.

In the momentum and tracer equations, the task of the parameters A and κ is to quantify the turbulent fluxes associated with the sub-scale mixing processes, e.g. mesoscale eddies. In the momentum equation, the divergence of these fluxes is implemented as Laplacian or harmonic diffusion. The horizontal viscosities in equations (3.8) and (3.9) and the vertical viscosities (in equations (3.1) and (3.2)) are set to constant values (independent of space and time) of $A_m = 2.5 \cdot 10^4 \text{m}^2/\text{s}$ and $\kappa_m = 10^{-3} \text{m}^2/\text{s}$, respectively.

The advection of tracers is handled by the flux corrected transport “FCT” scheme (ZALESAK (1979), GERDES ET AL. (1991)). FCT calculates the flux difference between a central difference and an upstream scheme. This anti-diffusive flux is added to the equation locally such that no under- (e.g. negative tracer concentrations) and overshoots are introduced. The main disadvantage of the FCT scheme is its time consumption. However, no additional explicit diffusion is necessary in the tracer equation.

A parametrisation to mix statically unstable stratifications is essential in this model, because the hydrostatic approximation disregards vertical accelerations due to vertical density variations. In this approach, an explicit convection scheme is used as proposed by (RAHMSTORF, 1993) and explained in PACANOWSKI (1995, chap 11.11) as the “fast

Description	Parameter	Value	Unit
Time step for internal/external mode velocities	$\tau_{u,v}$	3600	s
Time step for tracers	τ_h	21600	s
Vertical eddy viscosity coefficient	κ_m	10^{-3}	m^2/s
Horizontal eddy viscosity coefficient	A_m	$2.5 \cdot 10^4$	m^2/s
Vertical eddy diffusivity coefficient	κ_h	0	m^2/s
Horizontal eddy diffusivity coefficient	A_h	0	m^2/s
Bottom drag coefficient	c_d	0	
Restoring time constant for SSS	Δt_{rS}	180	days

Table 3.1: Parameterisations used in the ocean model

scheme". The whole water column is processed by mixing consecutively unstable boxes in one pass.

3.2 Sea Ice model

Beside the ocean model, a sea ice model is necessary. The ocean model alone is not able to represent the heat, freshwater and momentum fluxes between atmosphere and ocean in the Arctic region realistically, because the ice cover plays a central role in between. [HILBLER \(1979\)](#) introduces a dynamic-thermodynamic sea ice model, with a formulation for the ice interaction applying a viscous-plastic rheology. The thermodynamic growth and melting of sea ice is derived from an energy balance outlined by [PARKINSON AND WASHINGTON \(1979\)](#). A prognostic snow layer was added ([OWENS AND LEMKE, 1990](#)) and the rheology was improved by [HARDER \(1996\)](#). The following sections summarise the underlying model equations and the configuration used in the present study.

3.2.1 Equations

Sea ice reduces the atmosphere-ocean heat exchange substantially, so it is important to know the extension of the sea ice cover and the distribution of leads in it. Furthermore, the ice thickness controls the heat transport through the ice. Coarse resolution models idealise the various sea ice classes as a continuum ^{II}, where only the mean values over a larger area (e.g. a grid box) are taking into account. Thus, a set of prognostic, two-dimensional variables can be defined as horizontal mean values over a grid box:

- *Ice volume per area (h_i):*
 h_i has the dimension of length and denotes the vertically averaged ice thickness.

^{II}The continuum hypothesis is based on the assumption, that the mean values enclose a large number of ice floes, whose spatial extension is much smaller than the resolution of a grid cell.

Sea Ice model

- *Snow cover* (h_{sn}):
This is defined in analogy to the ice volume.
- *Ice concentration or spatial coverage* (A_i):
 A_i takes values between 0 and 1 (resp. 0% and 100% coverage), indicating the fraction of the grid cell, which is ice covered.
- *Ice age* (a_i):
The age of ice has the dimension time and it is positive definite ($a \geq 0$).
- *Ice drift velocity* (\vec{u}_i):
The vector \vec{u}_i describes the horizontal drift velocity in metres per second.

The extent and properties of sea ice are mainly dominated by two processes: thermodynamic growth (including sources and sinks of sea ice volume and connected heat exchange) and advection. The latter denotes the lateral exchange of ice with the adjacent regions. The spatial and temporal evolution of h_i , A_i , $h_i a_i$ and h_{sn} can be expressed as continuity equations:

$$\frac{\partial h_i}{\partial t} + \nabla \cdot (\vec{u}_i h_i) = S_i \quad (3.11)$$

$$\frac{\partial h_{sn}}{\partial t} + \nabla \cdot (\vec{u}_i h_{sn}) = S_{sn} \quad (3.12)$$

$$\frac{\partial A_i}{\partial t} + \nabla \cdot (\vec{u}_i A_i) = S_A \quad (3.13)$$

$$\frac{\partial (h_i a_i)}{\partial t} + \nabla \cdot (\vec{u}_i h_i a_i) = S_a \quad (3.14)$$

The S-terms on the right hand sides are the thermodynamic sources and sinks for the prognostic variables, except for the sea ice concentration source (S_A), where the ridging must be taken into account. If the right hand sides were zero, the equations would consist only of the local time derivative ($\frac{\partial}{\partial t}$) and the advection and the prognostic variables would be conservative. These balance equation have a modified upstream scheme for the advection term (after [SMOLARKIEWICZ, 1983](#)), which includes implicit diffusion and avoids unphysical solutions for e.g. negative ice concentration. No explicit diffusion is used. The calculation of the ice drift velocity is described below and the thermodynamic growth in equations (3.11)–(3.13) is illustrated.

Momentum balance

The overall forces acting on the ice determining the ice drift velocity u_i can be expressed as a momentum balance ([HIBLER, 1979](#)):

$$m \frac{D\vec{u}_i}{Dt} = \vec{\tau}_a + \vec{\tau}_w + \vec{K}_c + \vec{F} + \vec{K}_H \quad , \quad (3.15)$$

where m is the ice mass per unit area, $m\vec{u}_i$ the momentum of ice per unit area, $\vec{\tau}_a$ the atmospheric shear stress, $\vec{\tau}_w$ the shear stress between sea ice and ocean, \vec{K}_c the Coriolis

force, \vec{F} the internal forces due to the interaction between the floes and \vec{K}_H the force generated by the tilt of the ocean surface.

HARDER (1996) showed that the inertia term on the left hand side of equation (3.15) is one order of magnitude smaller than the terms on the right hand side, when the time scale of the surface forcing is at least one day. The ice drift velocity can now be solved diagnostically.

The shear stresses $\vec{\tau}$ can be described by an empirical relation (MCPHEE, 1979) as a squared dependency on the relative velocity difference (atmosphere-ice and ice-ocean, resp.). The wind velocity is two orders of magnitude larger than the ice drift velocity, therefore the atmospheric shear stress is expressed solely by the wind stress^{III}. The ocean velocity and ice drift are of the same order of magnitude and therefore the ocean drag is parametrised as follows:

$$\vec{\tau}_w = \rho_w c_w |\vec{u}_w - \vec{u}_i| \left[(\vec{u}_w - \vec{u}_i) \cos \Theta + \vec{k}_z \times (\vec{u}_w - \vec{u}_i) \sin \Theta \right] , \quad (3.16)$$

where ρ_w is the density of water, c_w is the ocean drag coefficient and \vec{u}_w is the ocean drift velocity. \vec{k}_z is the unit vector in the z-direction and Θ describes the deflection angle between the ocean shear stress $\vec{\tau}_w$ and the velocity difference $\vec{u}_w - \vec{u}_i$ (set to $\Theta = 25^\circ$, matching the geostrophic velocity of the second layer of the ocean model).

The Coriolis force and the force due to ocean tilt are

$$\vec{K}_c = -mf\vec{k}_z \times \vec{u}_i \quad (3.17)$$

$$\vec{K}_H = -mg\nabla H \quad , \quad (3.18)$$

with H denoting the height of the ocean surface relative to the geoid^{IV}. ∇H is approximated from the geostrophic velocity \vec{u}_w of the ocean model:

$$\nabla H = -\frac{f}{g}\vec{k}_z \times \vec{u}_w \quad (3.19)$$

The terms K_c and K_H are one order of magnitude smaller than the main forcing terms (i.e. the shear stresses and the internal forces) as shown by HARDER (1996). Thus, the tilt of the ocean surface can be neglected. The Coriolis term on the other hand, deflects the direction of the ice drift and must be taken into account. The equation (3.15) is then reduced to:

$$\vec{\tau}_a + \vec{\tau}_w + \vec{K}_c + \vec{F} = 0 \quad , \quad (3.20)$$

The heart of the momentum balance is horizontal friction term \vec{F} , which is described as a viscous-plastic rheology. For a continuum mechanic medium, the internal forces can be written as the divergence of the stress tensor $\vec{\sigma}$:

$$\vec{F} = \nabla \cdot \vec{\sigma} \quad . \quad (3.21)$$

^{III}The wind stress is prescribed by data, which will be presented in detail in 3.3.

^{IV}Surface of constant geopotential

The stress tensor $\vec{\sigma}$ is a function of the deformation rate tensor which is the symmetrical part of the vector gradient ($\nabla \vec{u}_i$), describing the deformation without rotation:

$$\dot{\epsilon}_{ij} = \dot{\epsilon}_{ji} = \frac{1}{2} \left\{ \frac{\partial u_i}{\partial x_j} + \frac{\partial u_j}{\partial x_i} \right\} . \quad (3.22)$$

The rotational part is neglected, because in ice dynamics it is assumed that internal forces cause a modification only in the shape. The deformation rate is a kinematic term, whereas the stress tensor is a dynamic term. The relation between kinematics and dynamics is determined by a law of rheology $\vec{\sigma} = \vec{\sigma}(\dot{\epsilon})$. For instance, the stress tensor is proportional to the deformation (and the deformation rate) for elastic or viscous behaviour. In contrast, plastic behaviour means no deformation occurs until a certain limit is reached, after which a plastic flow sets in. According to measurements during the *Arctic Ice Dynamics Joint Experiment* (AIDJEX),^V sea ice has

- a larger resistance against convergence and shear compared to divergence,
- no obvious elastic behaviour except for very small deformations ,
- almost no link between the internal forces and the rate of deformation.

Hence, the viscous-plastic approach is suitable for sea ice, because it is deformable to a certain extent and starts to flow afterwards with a constant deformation rate.

In this model, the connection between the stress tensor and the deformation is formulated in a way which is generally valid for viscous, isotropic media (see [HIBLER, 1979](#)):

$$\vec{\sigma} = \begin{pmatrix} \eta(\dot{\epsilon}_{11} - \dot{\epsilon}_{22}) + \zeta(\dot{\epsilon}_{11} + \dot{\epsilon}_{22}) - P/2 & 2\eta\dot{\epsilon}_{12} \\ 2\eta\dot{\epsilon}_{12} & \eta(\dot{\epsilon}_{22} - \dot{\epsilon}_{11}) + \zeta(\dot{\epsilon}_{11} + \dot{\epsilon}_{22}) - P/2 \end{pmatrix} . \quad (3.23)$$

This is a general formulation that has to be specialised by defining the pressure P . The shear viscosity η and the bulk viscosity ζ are defined as non-linear functions of the deformation rate. This is carried out as recommended by [HIBLER \(1979\)](#) in the form of an elliptical yielding curve, with the transition from viscous to plastic behaviour modified according to [HARDER \(1996\)](#).

$$\zeta = \frac{P_p}{2(\Delta + \Delta_{min})} \quad (3.24)$$

$$\eta = \frac{\zeta}{e^2} \quad (3.25)$$

$$P = \frac{P_p \Delta}{2(\Delta + \Delta_{min})} . \quad (3.26)$$

The parameter e regulates the eccentricity of the elliptical yielding curve and Δ_{min} is the regime parameter. Values for this parameters are chosen following the studies by

^VAIDJEX results have been described by, amongst others, [COON ET AL. \(1974\)](#)

KREYSCHER (1998) and listed in Table 3.2. P_p is the ice strength, expressed through the ice thickness and open water fraction ($1 - A_i$):

$$P_p(h_i, A_i) = P^* h_i \exp \left[-C(1 - A_i) \right] \quad . \quad (3.27)$$

C and P^* are also empirical constants (see Table 3.2). Further dependencies on temperature, salt and porosity are neglected. Δ is the kinematic measure for the entire deformation of the ice cover:

$$\Delta(\vec{\epsilon}) = \sqrt{(\dot{\epsilon}_{11}^2 + \dot{\epsilon}_{22}^2)(1 + e^{-2}) + 4e^{-2}\dot{\epsilon}_{12}^2 + 2\dot{\epsilon}_{11}\dot{\epsilon}_{22}(1 - e^{-2})} \quad (3.28)$$

The delimiter Δ determines whether the ideal-plastic range ($\Delta \rightarrow \infty$) or the linear-viscous range ($\Delta = 0$) is occupied. $\Delta_{min} \ll \Delta$ simulates a plastic behaviour and for increasing Δ_{min} the sea ice reacts in a viscous manner. A more detailed description of this rheology can be found in the theses of HARDER (1996) and KREYSCHER (1998).

Thermodynamic

Ice is built, when the water at the ocean surface freezes. This is a transformation from the liquid to the solid phase, due to a cooling of the water beyond the freezing point. The melting is the reversed process, initiated by a heat supply.

The representation of the thermodynamics of sea ice is based on an energy balance between ocean and atmosphere. The net heat flow into the upper layer of the ocean can be written as follows:

$$Q_a + Q_o + L_i(\rho_i S_i + \rho_{sn} S_{sn}) = 0 \quad . \quad (3.29)$$

Q_a and Q_o are the net heat fluxes from the atmosphere and from the ocean (Q_a and Q_o are assumed to be positive downward). S_i is the thermodynamic change of ice volume per area and S_{sn} for snow, resp. @. ρ_i and ρ_{sn} are the densities of sea ice and snow and L_i is the specific melt energy for sea ice. The difference between the heat fluxes from ocean and atmosphere in equation (3.29) is directly balanced by the melting or freezing of sea ice via a release or gain of latent heat. SEMTNER (1976) split this balance into two separate equations for each interface. This yields

$$Q_a + Q_c + \rho_i L_i \frac{\partial h_i}{\partial t} \Big|_a = 0 \quad (3.30)$$

for the upper, atmosphere–ice boundary and

$$Q_o - Q_c + \rho_i L_i \frac{\partial h_i}{\partial t} \Big|_w = 0 \quad (3.31)$$

for the lower, ice–ocean boundary.

The term Q_c is the conductive heat transport through the ice, which will be explained later on. The net atmospheric heat flux Q_a is composed of sensible and latent heat fluxes as well as short and long–wave radiation. The heat fluxes are parametrised through bulk

formula as described by PARKINSON AND WASHINGTON (1979). The short-wave radiation is composed of the cloudiness factor and an empirical equation for a cloudless sky, which depends on the solar zenith angle and the evaporation pressure (see PARKINSON AND WASHINGTON, 1979, for details). It also includes reflection with a set of albedos adjusted to the underlying surfaces (see Table 3.2), since snow-covered ice has a different albedo to melted ice, for instance. The net long-wave radiation depends on the surface temperature (T_s) of the ice according to the Stefan-Boltzman law, the atmospheric temperature (T_a) and the vapour pressure. The complete formulation can be found in the publication of ROSATI AND MIYAKODA (1988) and it is based on an empirical relationship of M.E. and T.G. Berliand (BUDYKO, 1974).

The boundary layer theory of the upper ocean is based on the formulation of the heat flux between ice and ocean by MORISON ET AL. (1987):

$$Q_o = \rho_w c_p c_h u_* (T_o - T_b) \quad (3.32)$$

The heat flux is a function of the temperature differences between the bottom of the ice T_b and the upper ocean layer T_o and the friction velocity u_* . The bottom temperature is fixed to the freezing point of sea water ($T_b = -1.83^\circ\text{C}$). The other parameters are c_p , the specific heat of sea water at sea level pressure and c_h , the transfer coefficient for sensible heat. u_* is a parametrisation of the turbulent mixing in the upper ocean:

$$u_* = \sqrt{c_w} |\vec{u}_w - \vec{u}_i|, \quad (3.33)$$

where c_w is the ocean drag coefficient as introduced in equation (3.16). The term Q_c in equations (3.30) and (3.31) is the conductive heat transport through the ice. In this approach, the ice has no heat capacity, thus the conductive heat transport appears in both equations but with inverse signs. It is proportional to the temperature difference between the surface (T_s) and bottom (T_b) of ice and snow. As snow has a much smaller heat conductivity (k_{sn}) than ice (k_i), it is an even better insulator. So Q_c can be described as follows:

$$Q_c = \frac{A_i}{h_i/k_i + h_{sn}/k_{sn}} (T_b - T_s) \quad (3.34)$$

The surface temperature T_s is determined iteratively, so that the energy budget is balanced at the surface:

$$Q_a(T_s) + Q_c(T_s) = 0. \quad (3.35)$$

When T_s reaches a temperature above the freezing point of snow (0°C), then it is set back to zero and the surplus of energy is used for melting snow or ice, according to equation (3.30). It is assumed that, at first, all snow (if present) is melted before diminishing the ice cover. The conductive heat transport is now fixed subsequently and used in equation (3.31) to determine whether there is freezing or melting at the bottom of the ice.

Sources and sinks of the ice concentration (S_A), which describe a lateral change of the

ice cover, are determined by an empirical relation:

$$S_A = \underbrace{\frac{1 - A_i}{h_0} G_i}_{\text{freezing}} + \underbrace{\frac{A_i}{2h_i} M_i}_{\text{melting}} + \underbrace{C_i}_{\text{ridging}} \quad (3.36)$$

Freezing is proportional to the open water area ($1 - A_i$) and the freezing rate ($G_i = \max(S_i, 0)$). The empirical parameter h_0 controls the velocity of lead closing. Melting reduces the ice area depending on the melting rate $M_i = \min(S_i, 0)$ and it is inversely proportional to the actual ice thickness h_i/A_i . It is thereby taken into account that thin ice melts faster than thicker ice. The last term, C_i , describes the ridging due to shear deformation. For details see [HARDER \(1996\)](#).

The source of snow in equation (3.12) is precipitation, which is defined as snow when the air temperature falls below the freezing point ($T_a = 0^\circ\text{C}$). Snow can only fall over the ice covered region. Melting processes have already been discussed in the context of an energy surplus between the oceanic and atmospheric heat fluxes. As snow reflects more of the incoming radiation than ice, it reduces the amount of energy available for melting. Thus a special albedo was set for the snow and melting snow.

The ice age is a scalar variable describing, besides the ice thickness and the ice concentration the properties of the sea ice cover. Recurring freezing and melting cycles add vertical layers of ice with different ages, which can not be resolved by coarse resolution models. Thus, the ice age is vertically averaged over all layers. The mean ice age of a grid box comprises the mean ice age of the actual ice at one time step, the new vertically built ice and the inflowing ice from neighbouring boxes. The prognostic equation (3.14) for the ice age is therefore based on the product of ice age a and ice volume per area h . The source term of ice age (equation 3.14) is composed of the ice thickness and the melting rate (M_i):

$$S_a = h_i + a_i M_i \quad (3.37)$$

When new ice is built, it has an ice age of zero. Assuming no changes in ice thickness, i.e. no melting or freezing, the ice ages every day by one day. The melting process leaves the age of the ice unchanged, whereas freezing reduces the ice age to the same degree as new ice being built. The ice age can be used as a tracer in the investigations. The thesis of [HARDER \(1996\)](#) focuses on the ice aging.

“Flooding” is also taken into account in the model. The accumulation of snow can push the boundary between snow and ice layer under water and the floe is flooded. The drowned part of the snow layer is converted to ice, so that the boundary between ice and snow reverts to the water-line. Flooding is rare in the Arctic Ocean because the ice layer is usually too thick and, moreover, the snow layer is not heavy enough.

3.2.2 Setup

The ice model runs on the same rotated grid as the ocean model. The grid cells also have the size of approximately $1^\circ \times 1^\circ$. The only difference lies in the ice model’s south-

Sea Ice model

ern boundary, which is further to the north, located at roughly 50°N. Outflow is allowed only across this boundary, where the ice melts immediately. All other boundaries are closed. The numerics are formulated on the Arakawa B grid, described by [HILLER \(1979\)](#). Table 3.2 summarises all important parameters for the ice model. They are based on the results of the Sea Ice Model Intercomparison Project (SIMIP), which are detailed in [KREYSCHER ET AL. \(2000\)](#). This project includes the testing of different rheology schemes. Many observations, such as ice thickness calculated from upward looking sonars (ULS), buoy drift data, ice concentrations and ice-drift estimates from satellite measurements, were used to validate the results. Furthermore, the above-mentioned parameters were varied to achieve results which are as realistic as possible. It was found that the viscous-plastic scheme predicts the spatial patterns of ice thickness, large-scale ice drift and ice export through the Fram Strait better than other tested approaches. The

Description	Parameter	Value	Unit
Dynamic parameter:			
Drag coefficient for the ocean	c_w	$5.5 \cdot 10^{-3}$	
Rheological parameters:			
Ice strength	P^*	15000	Nm^{-2}
Ice concentration parameter	C	20	
Eccentricity of the yield curve	e	2	
Regime parameter	Δ_{min}	$2 \cdot 10^{-9}$	s^{-1}
Thermodynamic parameters:			
Specific heat of sea water	c_p	4098	$J kg^{-1} K^{-1}$
Transfer coefficient for sensible heat	c_h	$1.75 \cdot 10^{-3}$	
Density of sea ice	ρ_i	910	$kg m^{-3}$
Density of snow	ρ_{sn}	300	$kg m^{-3}$
Density of water	ρ_w	1025	$kg m^{-3}$
Specific melt energy for sea ice	L_i	$3.32 \cdot 10^5$	$J kg^{-1}$
Lead closing parameter	h_0	1	m
Thermal conductivity of ice	k_i	2.1656	$W m^{-1} K^{-1}$
Thermal conductivity of snow	k_{sn}	0.31	$W m^{-1} K^{-1}$
Radiation parameters:			
Albedo for open water	α_w	0.1	
Albedo for ice (without snow)	α_i	0.65	
Albedo for melting ice (without snow)	α_m	0.60	
Albedo for snow	α_{sn}	0.80	
Albedo for melting snow	α_{sm}	0.70	

Table 3.2: Parameters used in the ice model.

ice model settings used here are based upon the works of [HARDER \(1996\)](#), [KREYSCHER \(1998\)](#) and [KREYSCHER ET AL. \(2000\)](#).

3.3 Data exchange

Atmospheric forcing

The atmospheric forcing is provided by a data set including wind stress forcing (λ - and ϕ - components and the mean scalar wind), air temperature and dew point temperature at two metres above sea level, precipitation and total cloud cover. Observations were assimilated into models to give consistent data on a uniform grid. On the one hand, the model results from the NCEP/NCAR reanalysis ([KALNAY ET AL., 1996](#)), covering the years 1948 - 1998, are used. The data are stored every six hours and are computed on a global grid with approximately 2° spatial resolution. For the present study, the data is interpolated onto the model grid, as daily mean values for wind stress and monthly mean data for the scalar fields. On the other hand, data of the ECMWF reanalysis project from 1979 - 1993 ([GIBSON ET AL., 1997](#)) are applied. The ECMWF data have been interpolated to the model grid in a similar way as the NCEP/NCAR data. A detailed description of which data set is actually chosen and how the data have been prepared, will be given in the chapter 4.

The wind stress field is used in the model directly as a source of momentum acting on the surface. The other parameters are necessary to calculate the heat and freshwater fluxes for the sea ice and the ocean model. The heat flux from the atmosphere to the ice has been described briefly in the discussion of the energy balance of the ice model; it is determined similarly in the ocean model. The air temperature, dew point temperature and the cloud cover are used to derive the sensible and latent heat fluxes and the net short-wave and net long-wave radiation. The freshwater flux into the ocean is calculated from precipitation, evaporation and river runoff. Evaporation is a function of latent heat including the dew point temperature. Precipitation is prescribed.

The ocean model needs special treatment for the sea surface salinity. This is done using a weak linear restoring to a climatological field (see Table 3.1). This treatment is necessary to parametrise the lateral freshwater input through the Bering Strait and the river run off into the Arctic ocean. The climatology used is obtained from the data of [LEVITUS ET AL. \(1994\)](#) and the EWG-atlas ([EWG - ENVIRONMENTAL WORKING GROUP, 1997](#)) for the area north of 72°N .

Models communicate

The models are computed with the same time step (tracer time step) of 21600s. Upon completion, the ice model provides heat, freshwater and momentum fluxes for the ocean. The ocean model, in turn, supplies current and heat exchange information for the ice model.

The sea ice and the ocean model calculate the atmospheric heat fluxes separately, because they depend on the surface properties of the underlying medium (such as temperature and albedo). In addition, the ice model needs the ocean surface temperature T_o to compute the heat fluxes at the bottom of the ice. The energy balance of the ice model has been discussed in detail in the thermodynamic part of section 3.2.1. For grid boxes which are partly covered by sea ice the fluxes into the ocean are weighted according to the percentage of ice coverage:

$$Q_{ocean} = (1 - A_i) \cdot Q_{open_water} - A_i \cdot Q_o \quad (3.38)$$

The open-water fraction is calculated by the ocean model, the ocean-ice part Q_o by the ice model (compare equation 3.32).

Beside the heat flux, the freshwater flux is also altered by the ice due to snow and ice formation or melting. Net precipitation (precipitation minus evaporation) which falls over ice-covered regions will be snow when the air temperature is below the freezing point. It is also weighted with the snow covered area according to equation 3.38. When the temperature is above the freezing point, the net precipitation of the grid box flows into the open water. The fraction belonging to the ice model is multiplied by the average salinity of sea water and transferred to the ocean as an additional term to the salinity restoring. This formulation is chosen because it conserves the salt budget. The fact that the sea ice retains a small amount of salt when ice forms and releases a brine while aging is neglected. The ice model also needs the geostrophic velocity to calculate the heat flux, Q_o , and the shear stress, τ_w .

The technique of coupling of the two models has been described by [HIBLER AND BRYAN \(1987\)](#). The numerical representation of the temporal dependencies of the momentum exchange has been illustrated by simplified one-dimensional equations:

$$\frac{\partial u_i}{\partial t} = F(u_i) + \frac{\partial p}{\partial x} - D(u_i - u_w) + \tau_a \quad (3.39)$$

$$\frac{\partial u_w}{\partial t} = \frac{\partial p}{\partial x} + F(u_i) + \tau_a \quad (3.40)$$

The nonlinear ice interaction terms are embodied in F , and D denotes the drag term. The most important feature of this approach is that the sea ice is handled as a part of the uppermost layer of the ocean. The wind stress transmitted into the ocean is equal to the wind stress plus the internal ice stress. Additionally, the convergence of ice must be considered in the Ekman convergence. When ice is present, the whole mixed layer is at the freezing temperature. The ocean transfers heat to the ice by warming up this layer. This implicit procedure therefore forces the ice cover and the SST to stay in balance and at the same time ensures conservation of heat.

The leapfrog scheme is used as the time-stepping discretisation:

$$u_i^{i+1} - u_i^{i-1} = 2\Delta t \left[F(u_i^{i+1}) + \frac{\partial p^i}{\partial x} - D(u_i^{i-1} - u_w^{i-1}) + \tau_a^i \right] \quad (3.41)$$

$$u_w^{i+1} - u_w^{i-1} = 2\Delta t \left[\frac{\partial p^{i+1}}{\partial x} + F(u_w^i) + \tau_a^i \right] . \quad (3.42)$$

The past is labelled $i - 1$ and the future time steps $i + 1$. The exchange terms are centred differences wherever this is possible. A detailed discussion of the discretisation can be found in the publication of [HIBLER AND BRYAN \(1987\)](#).

Starting point

The surface forcing fields consist of monthly mean data sets for the scalar properties such as air and dew point temperature, cloud cover and mean scalar wind. The wind stress data is given to the model as daily data.

Ice and ocean models start from a state of rest, but they need hydrographic starting values. Thus, the ocean below the surface is assigned salinity and potential temperature data as initial conditions, which are spatially interpolated from the Levitus data set ([LEVITUS ET AL., 1994](#)). The continental run-off is not taken into account, and the lateral boundaries are closed except in the south, where the barotropic streamfunction of the FLAME 4/3° Atlantic ocean model is prescribed as described in section 3.1.2. The sea surface salinity (SSS) gets an initial climatological data field, which is also used for restoring. The data are based on the climatology of [LEVITUS ET AL. \(1994\)](#) and the EWG-atlas ([EWG - ENVIRONMENTAL WORKING GROUP, 1997](#)) for the area north of 72°N, because of the regional unreliability of the Levitus data. The same procedure is adopted for the initialisation of the sea surface temperature (SST). However, there is no restoring of the sea surface temperature in the model calculation.

The initial sea ice concentration is a climatology calculated from the SSM/I data for the period 1986-1992. The initial sea ice thickness is a linearly interpolated field between 0m for ice free grid cells and a maximum of 4m thickness for completely ice covered areas.

4 Atmospheric forcing

Circulation models are sensitive to their forcing. Before this sensitivity is described in the following chapters, the three different sets of forcing fields that will be used to drive the model are presented and discussed in this chapter: OMIP, NAO+ and NAO–.

4.1 OMIP data

The ocean model intercomparison project (OMIP) compared two different coupled ocean–sea ice models: the Hamburg Primitive Equation model (HOPE) (WOLFF ET AL., 1997) and the Modular Ocean Model (MOM). Details about the project and its results can be found in FRITZSCH ET AL. (2000). In order to separate the effects of model characteristics from external effects, a forcing data set common to both models was constructed. The data set comprises a mean year calculated for the period 1979 to 1993 using data from the ECMWF reanalysis project. This mean year consists of monthly mean values for the fifteen year period, but it is also necessary to account for the daily wind stress variability, which is important for the high frequency variability of sea ice. The year 1982, having the maximum variance, was chosen to provide the daily variability. This is based on the consideration that the variance is reduced due to filtering and the aim is to preserve as much variability as possible. This daily variability was added to the individual monthly mean values. The OMIP year is very convenient for the spin-up calculation of the model, because it has no unphysical jump between the end of December and the beginning of January. The set of atmospheric fields for the mean or typical year will be referred to as OMIP year in the following.

In Fig. 4.1 the wind stress fields of the mean over the months November to April (NDJFMA) are shown. In the Nordic Seas, the wind stress is cyclonic, with northward winds at the Norwegian coast and southward winds along the coast of Greenland. In the Labrador Sea, north–west wind stresses are dominant, representing the eastern branch of the cyclonic circulation which is centred between Greenland and Iceland. Trade winds and the mid–latitude westerlies dominate the large scale structure of the wind stress field. Strong offshore winds blow along the North American continent. An atmospheric pressure dipole with a high at the Azores in the eastern North Atlantic and a low between Iceland and Greenland governs the pathway of air masses crossing the North Atlantic. In the case of the OMIP year, the main path of the westerlies starts north of 45°N at the coast of North America and extends north–eastward into the Norwegian Sea. In the Nordic Seas, the wind stress is also cyclonic, with northward winds at the Norwegian

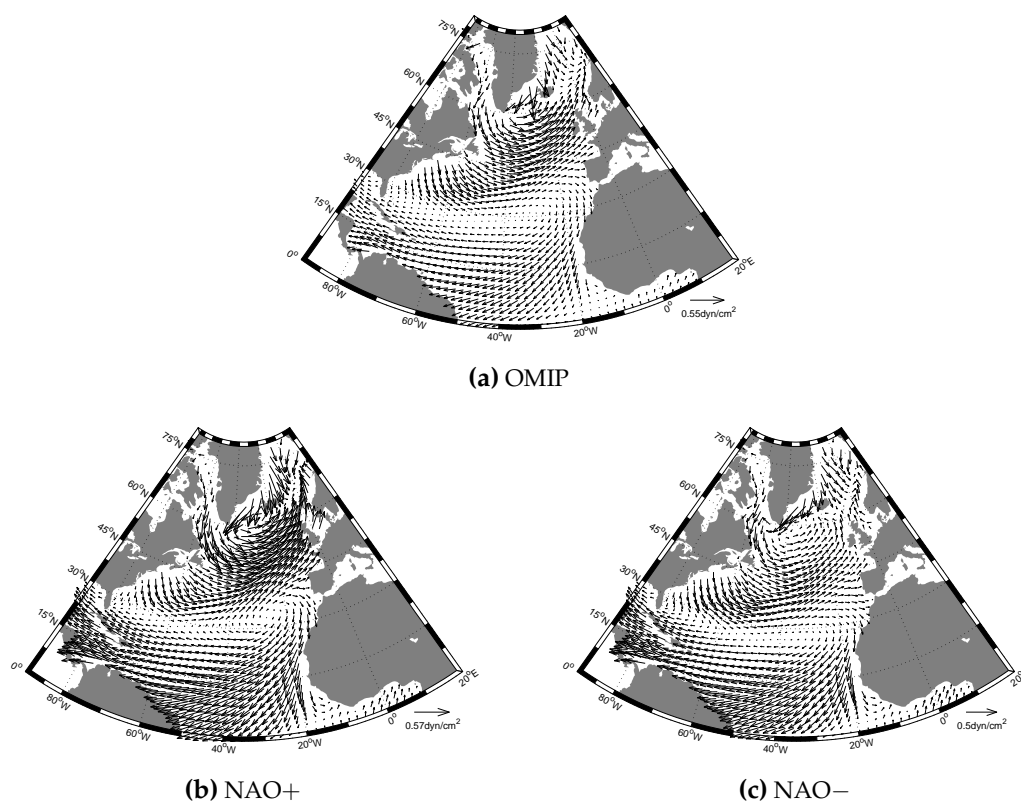


Figure 4.1: NDJFMA mean of the windstress fields (in dyn/cm^2); a) OMIP year, b) NAO+ composite, c) NAO– composite

coast and southward winds at the coast of Greenland. In the Labrador Sea, north–west wind stresses represent the eastern branch of the cyclonic circulation which is centred between Greenland and Iceland.

The winter air temperature reveals a zonally asymmetric pattern, with warm air masses over the eastern North Atlantic and cold air over the western North Atlantic (Fig. 4.2). In the OMIP year, the warm air extends into the Barents Sea, and the east coast of Greenland is influenced by cold polar air. In the Labrador Sea, the front, which separates warm subtropical air masses from cold polar air masses, is located in the south. In the Arctic Ocean, the air temperature is characterised by nearly uniform air temperature of -25°C .

4.2 NAO+ and NAO– composites

The NCEP/NCAR reanalysis project provides the data from which the NAO composites are generated. These data have the advantage over the ECMWF data that they cover a longer time period from 1948 until now, and thus contain long periods of positive and negative NAO years. Here, the NAO index of JONES ET AL. (1997) was chosen, which

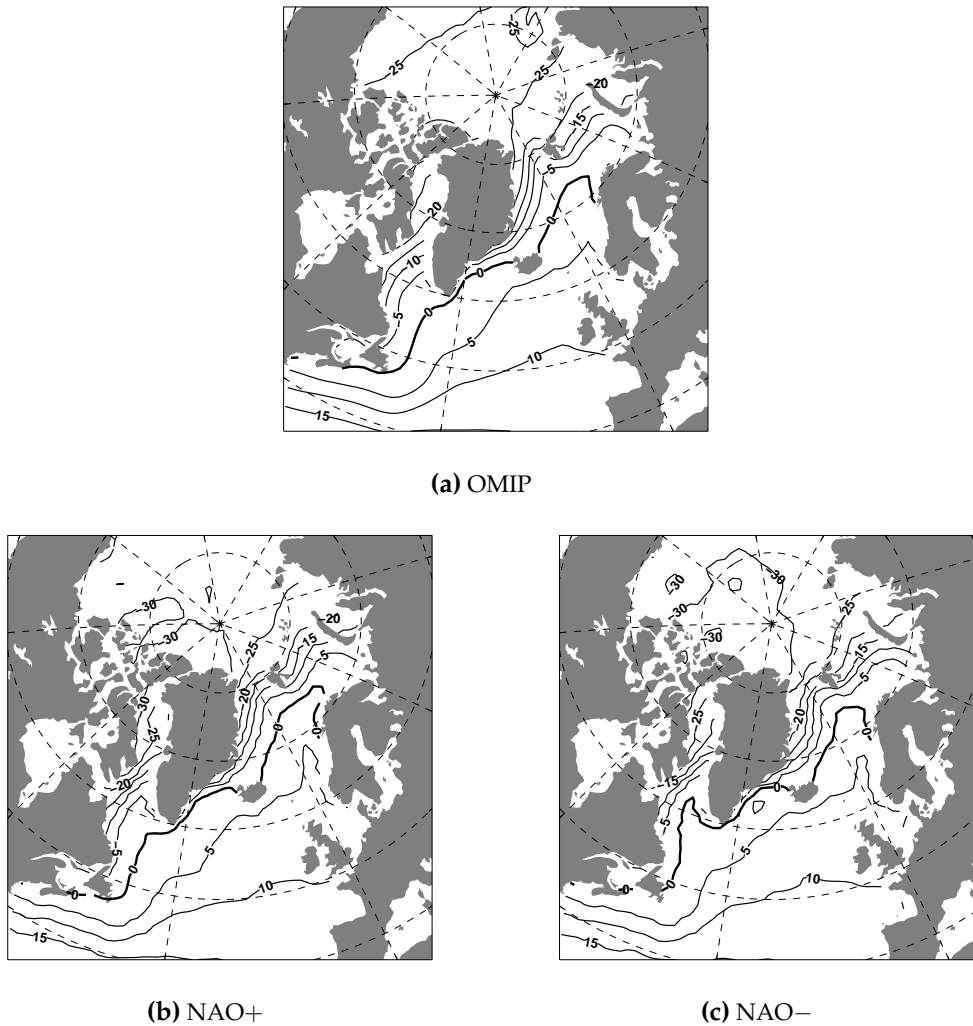


Figure 4.2: NDJFMA mean of the surface air temperature (in °C); a) OMIP year, b) NAO+ composite, c) NAO– composite

is defined as the difference between the normalised sea level pressure (SLP) between Gibraltar and Iceland. According to [OSBORN ET AL. \(1999\)](#), this index has a higher correlation between high and low pressure centres for the winter month (DJFM) than the SLP difference between the Azores and Iceland ([HURRELL, 1995](#)). The time series from 1948 until 2000 is normalised to zero mean and unit variance. The years with standard deviation larger than one are selected for the NAO+ composite (1957, 1961, 1967, 1983, 1989, 1990, 1994, 1995); values of less than minus one standard deviation constitute the years for the NAO– composite (1955, 1956, 1963, 1965, 1969, 1977, 1979, 1996). A year in this study begins in July and ends the following June; January defines the corresponding year. The monthly mean fields are averaged over the above NAO+ years. An EOF anal-

NAO+ and NAO– composites

ysis shows that the year 1983 is the year with the strongest variability in the daily wind stress. The daily wind stress anomaly of this year is added to the monthly mean wind stress values to ensure consistent day-to-day variability. For the NAO– composite, the year 1979 is chosen for daily wind stress values following the same criteria.

The largest difference of the winter half year (NDJFMA) between the NAO+ and NAO– composites is found over the North Atlantic with the prominently strengthened wind stresses in the west wind drift zones for NAO+ conditions. This is visible in Fig. 4.3(a), where the difference in the wind stress pattern between the NAO+ and NAO– composites is shown. The cyclonic low pressure system over Iceland is stronger than normal, bringing warm, humid air to northern Europe. This is apparent in the position of the 0° isotherm in Fig. 4.2(b), which reaches far north into the Barents Sea. In

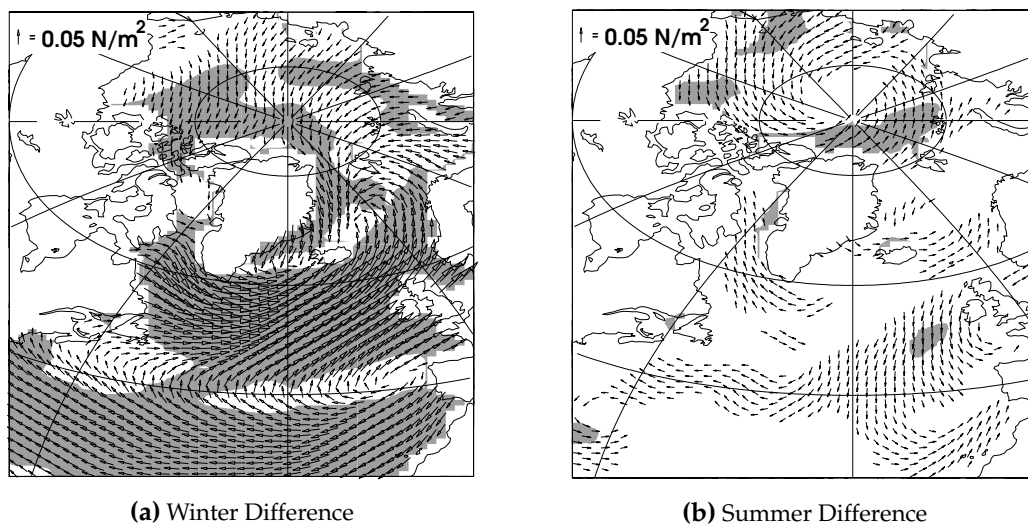


Figure 4.3: *Difference between the NAO+ and NAO– composite of the wind stress (in N/m^2 ; significant regions are the shades; quadratic scale of arrow length)*

the Barents Sea and all along the coast of Siberia an intensification of the cyclonic circulation is visible in northward, offshore wind stresses for the NAO+ composite (Fig. 4.3(a)). The air temperature is homogeneously -25°C over the Arctic Ocean, with patches of colder air masses over the Canadian Archipelago, whereas in the NAO– composite, a larger area has air temperatures below -30°C (Fig. 4.2(c)). Over the Greenland Sea, the enhanced low pressure of the NAO+ composite with stronger southward wind stresses shifts the front between cold and warm air towards the coast of Greenland. As a consequence, the air temperature in this area is warmer than in the NAO– composite. Strong offshore wind stresses occur at the coast of Newfoundland entailing cold outbreaks of continental air masses over the Labrador Sea. The 0° isotherm is therefore relocated to the southern rim of the Labrador Sea (Fig. 4.2(b)). In the NAO– composite on the other hand, the 0° isotherm reaches north into the Labrador Sea. The winter air temperature

difference shows a dipole structure with a minimum of -8°C centred in the Labrador Sea and maxima of 4.5°C in the Barents Sea and 6.5°C in the Greenland Sea (Fig. 4.4(a)). In the central Arctic Ocean the temperature is raised by 2°C , with differences up to 3°C over the Eurasian shelf. The temperature differences south of 50°N are very small and thus not shown here. However, in the NAO+ composite, the wind stress in the west wind zone and the trade winds are strongly enhanced. Fig. 4.3(b) shows the difference

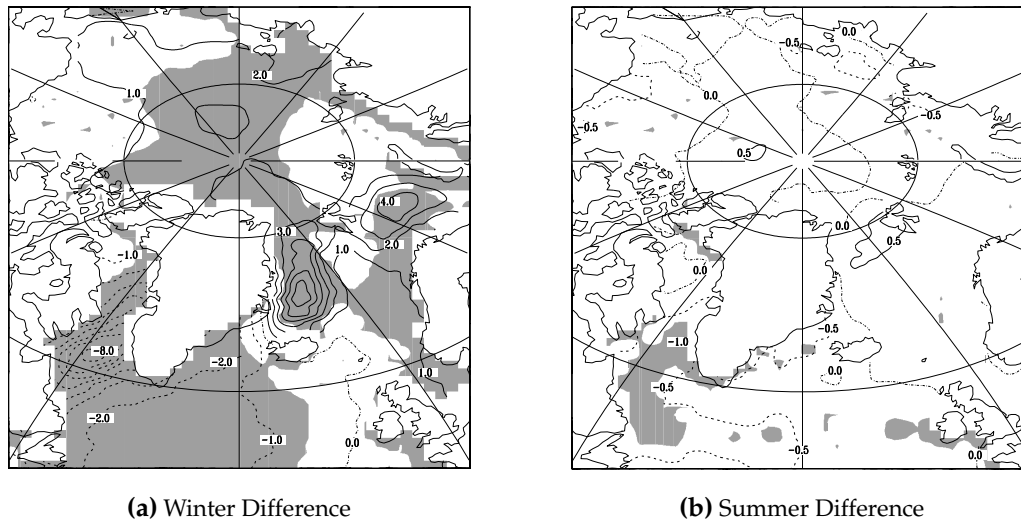


Figure 4.4: Difference between the NAO+ and NAO– composite of the two metre temperature in $^{\circ}\text{C}$ (significant regions are shaded)

between the NAO+ and NAO– wind stress in the summer (MJJASO). The absolute values of wind stress are much lower than in winter and the mean fields between NAO+ and NAO– composites are very similar. Over almost the whole North Atlantic, no differences are distinguishable. Driven by an anticyclonic circulation in the NAO– composite in summer, the anticyclonic circulation becomes stronger in the western Arctic Ocean. In contrast, the NAO+ composite displays very weak winds in the margins of the Beaufort and Bering Seas.

To decide whether the differences between the two composites are significant, a Student's *t* test was performed (VON STORCH AND ZWIERS, 1999). The means of the two composites are determined to be separable when the significance is greater than 90%, which corresponds to the shaded areas of Fig. 4.3. In winter, the differences in the wind stress over almost the whole North Atlantic ocean are significant. In the Arctic Ocean only the differences north of the Canadian Archipelago and along the coast of the East Siberian and Kara Seas are significant.

In summer, the differences between the composites are insignificant over large areas of the North Atlantic. An exception is the Arctic Ocean in the region of the Bering Strait and Beaufort Sea as well as north of Greenland and the Fram Strait, where the differences are

significant. The differences in air temperature for the summer composites are very small (Fig. 4.4(b)). The Labrador Sea is the only region where temperature differences greater than 0.5°C are present.

4.3 Discussion

The forcing fields which will be used in the following chapters are introduced here for a general overview, but it is also important to know their differences and similarities. The 15 years of the ECMWF reanalysis data lie in a period of positive NAO. The first year, 1979, is the only year with a significant negative NAO index. The first half of the eighties also has some years with negative index, but the NAO index is less than one standard deviation from the mean. Thus, the OMIP year appears to be biased towards a positive NAO index.

In the NAO+ composite, the westerlies cross the North Atlantic bringing the associated air masses to northern Europe and into the Nordic Seas (Fig. 4.1(b)). Here, the southward wind stresses at the coast of Greenland are very strong and in the Labrador Sea, the north-west wind stresses along the coast of Newfoundland are intensified. In the NAO- composite, the westerlies pathway is shifted to 35°N at the North American coast, transporting the associated air masses to southern Europe with a weak extension into the Nordic Seas. The pathway of the westerlies in the OMIP year is comparable to the pathway in the NAO+ composite, which is not surprising keeping in mind that the OMIP year is a mean field from primarily NAO+ index years. However, the wind stresses are not as strong as in the NAO+ composite. This is pronounced in the tropics south of 30°N , where the OMIP wind stresses are weak compared to the NAO composites. The NAO has its strongest impacts in the northern North Atlantic and the region south of 30°N is far from the centre of action. The significant differences between the NAO composites and the OMIP year are nevertheless important, because they will have consequences for the large scale circulation.

The illustration of the magnitude of the wind stresses of the three forcing fields can further illuminate these differences. The wind stresses in the OMIP year have the greatest magnitude between 45°W and 10°W and 45°N and 55°N (Fig. 4.5(a)). This position corresponds with the greatest magnitudes in the NAO+ composite. In the NAO- composite, the greatest wind stresses are found over the Sargasso Sea, which is south-west compared to the NAO+ composite. The wind stresses in the Labrador Sea differ between the NAO+ composite and the OMIP year, where the latter shows only a small increase in magnitude. The same is true for the wind stress distribution at the east coast of Greenland, where the NAO+ composite reveals significantly stronger wind stresses than the NAO- composite, whereas the OMIP year corresponds with the NAO- distribution. Thus, in mid-latitudes, the OMIP year is biased towards the NAO+ situation, but south of 30°N and north of 60°N the wind stresses are much weaker than in the NAO+ composite and partly also weaker than in the NAO- composite. This is due to the general

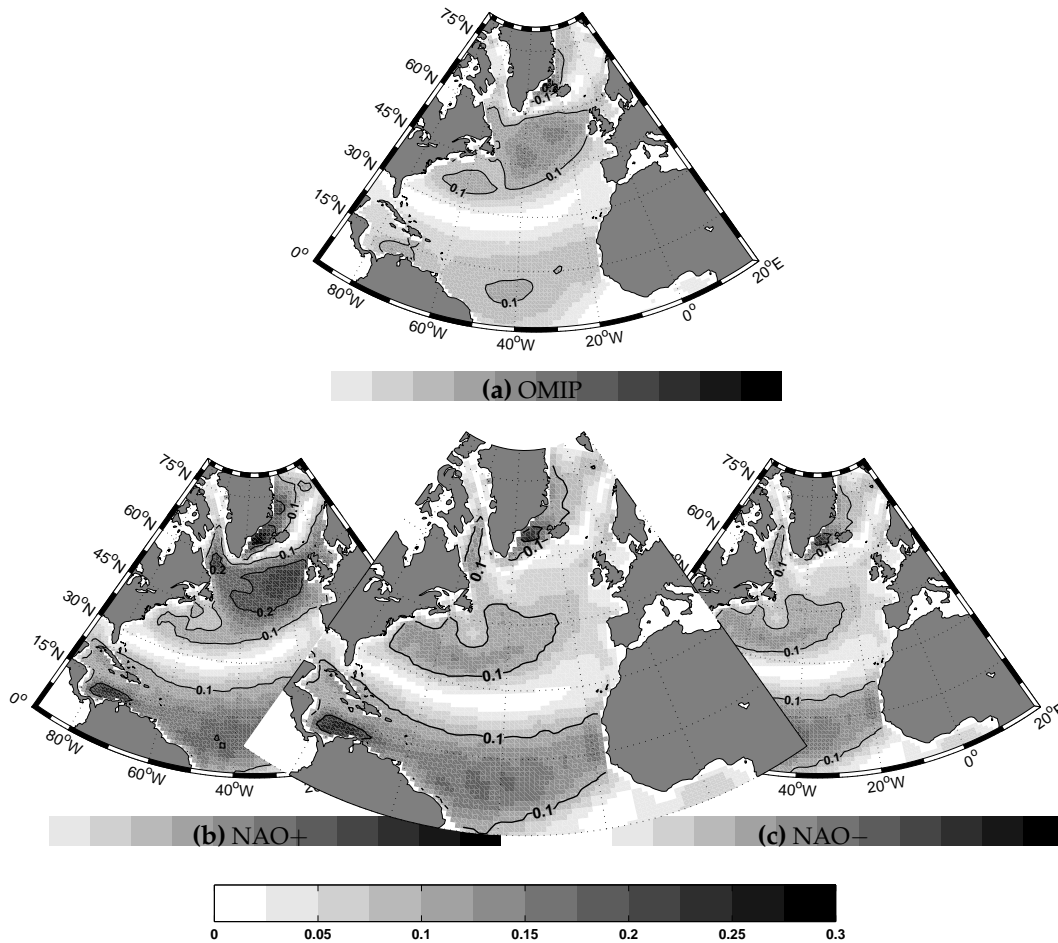


Figure 4.5: NDJFMA mean of the magnitude of the wind stress vector (in N/m^2); a) OMIP year, b) NAO+ composite, c) NAO- composite

differences between the ECMWF and the NCAR/NCEP reanalysis data. In the sensitivity experiments, which are presented in the following chapters, the two products are not used side by side because of these differences and their impact on the circulation which have to be taken into account.

The air temperature of the OMIP year and the NAO+ composite agree fairly well in the Labrador Sea. Over the Barents Sea and the Greenland Sea, on the other hand, the gradient between the cold and warm air masses corresponds better with the NAO- composite than with the NAO+ composite.

The analysis of the differences between the NAO+ and NAO- composite revealed that the main observed effects of the NAO are included in the forcing fields, such as the shift of the westerlies and the dipole pattern in air temperature. The differences in wind stress and air temperature are greatest during winter months. This is also found in the observations, where the correlation between high and low pressure is highest for the

Discussion

winter months DJFM. The differences in the summer distribution are very small except for the wind stresses in the Arctic Ocean.

The OMIP year has the advantage of a smooth seasonal cycle, which allows long experiments to be run, but it is important to keep in mind that it is a typical year of a special period over the years 1979 to 1993 from a distinct reanalysis (ECMWF). Systematic differences between the forcing fields can have a wide range of consequences such as strength of the subtropical gyre and meridional overturning, which will be the topic of the following chapter.

5 Spin up

The influence of the various model parameters on the hydrography and circulation in the models in general and the reason for certain model shortcomings have already been discussed comprehensively in the context of coarse resolution models and this is not within the scope of this study (see GERDES (1989) and GERDES AND KÖBERLE (1995)). However, the response of the model to changes in surface fluxes depends on its mean state. Therefore, the mean states of three basic experiments are compared in this chapter. The experiments are calculated with different sets of atmospheric forcing fields, namely the OMIP year, the NAO+ and the NAO– composites. These forcing fields have been discussed in chapter 4. The presentation of the mean states and their differences is also important for sensitivity experiments, which will be presented in the following chapters.

5.1 Hydrography

Three experiments with different atmospheric forcing fields are discussed here. The first experiment is called OMIP and is calculated with the OMIP year of the ECMWF reanalysis period as described in section 4.1. This forcing data set consists of monthly mean thermohaline atmospheric forcing (i.e. air temperature, dew point temperature at two metres above sea level, precipitation, total cloud cover and mean scalar wind) and daily wind stress forcing for one year. In two other experiments the model is driven by the NAO+ and NAO– composites, which were introduced in section 4.2. All model parameters are listed in Tab. 3.1 and Tab. 3.2 and kept fixed for all experiments. All experiments are initialised from a state of rest and integrated for 250 years. Two different time average periods have been chosen for illustrating the mean state: years 10 to 60 and years 150 to 200.

The temperature¹ fields at 300 m depth are chosen for the discussion (Fig. 5.1). The results are compared with the 1° resolution climatology of GOURETSKI AND JANCKE (1998). These data are a product of the hydrographic programme of the World Ocean Circulation Experiment (WOCE) and combine measured hydrographic parameters from the field phase of WOCE and historic data.

At first sight, the model results and the observations are in good agreement. The simulations reflect the temperature maximum in the centre of the subtropical gyre and the shallowing of the thermocline towards the equator. The north–eastward transport of

¹All temperatures referred to in this study are potential temperatures

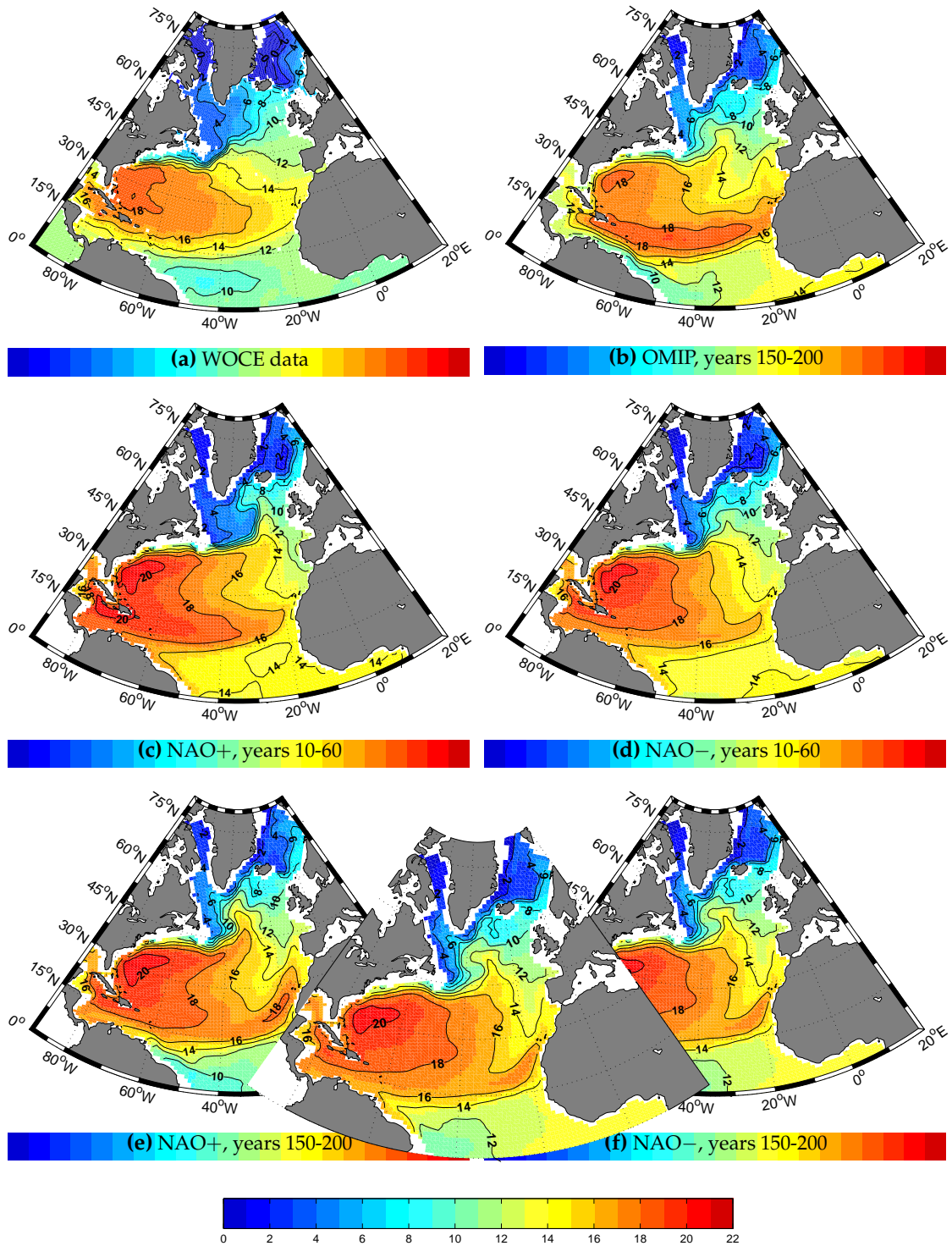


Figure 5.1: Potential temperature in 300 m depth of the North Atlantic, averaged over 50 years (in °C). a) The climatology of GOURETSKI AND JANCKE (1998), b) OMIP experiment, mean of years 150-200, c) NAO+ experiment mean of years 10-60, d) NAO- experiment, mean of years 10-60, e) NAO+ experiment mean of years 150-200, d) NAO- experiment, mean of years 150-200.

warm water by the Gulf Stream across the North Atlantic and into the Nordic Seas is present in all experiments and at all displayed times, as well as the southward transport of cold water by the East Greenland Current (EGC) and the Labrador Current. This results in a zonal temperature gradient in the subpolar North Atlantic and Nordic Seas. The model is capable of maintaining the sharp gradients in fronts such as the Gulf Stream. This is due to the numerical formulation of the advection of tracers in the model. The flux corrected transport scheme (FCT) is used, which features little implicit diffusion and is free of numerical dispersion, thus no explicit diffusion is needed and the erosion of the gradients is prevented (as described in section 3.1.2).

One difference between model simulations and observations is the location of the isotherms east of New Foundland, which represent the path of the NAC. In observations, it leaves the coast near Cape Hatteras at 35°N, whereas in model simulations this separation is shifted to the north offshore of the Grand Banks. This is a known problem common in coarse resolution models and visible in all three experiments. Another problem is the position of the Subpolar Front. This is the separation between the warm, subtropical water masses and the cold, polar water masses spanning from 35°N, 30°W to 55°N, 30°W. In the mean of the NAO– experiment, years 10 to 60 (Fig. 5.1(d)), the position of the front agrees very well with the observations. The NAC is visible as a sharp temperature gradient, taking a stepwise north–easterly direction. In the NAO+ experiment, the NAC stays on a zonal path downstream of New Foundland and the Subpolar Front is shifted to the east (Fig. 5.1(c)). The cold water in the subpolar gyre spreads therefore over a large area. The inflow of warm water into the Nordic Seas is close to the observations between 8° and 10°C. Further downstream the temperature gradient at the Norwegian coast is an indication for the position of the Norwegian Atlantic Current, which agrees with measurements. The EGC, which carries cold water of Arctic origin to the south, is very pronounced in all model results. The Irminger Sea is warmer in the NAO+ experiment, where the 8°C isotherm passes right through the area along with a branch of the NAC. This branch is more zonally oriented in the NAO– experiment and shifted to the south, thus the Irminger Sea is colder. The Nordic Seas show in the centre a circular patch of temperatures below 2°C, which is not resolved in the WOCE data (Fig. 5.1(a)) but closely linked with the doming of the Greenland gyre. Ekman suction brings cold water from deeper layers to the surface. In the eastern North Atlantic ocean, the Azores Current should be present at 34°N, 25°W, but the mode water production of the model is quite strong, which modulates the isotherms in this area. Thus, an Azores Current is not distinguishable. The model can produce a prominent layer of mode water by convection, which is mixed only moderately with the surrounding water masses, but transported to the south–west. Level models with a Gent–McWilliams parametrisation of tracer advection (GENT AND MCWILLIAMS, 1990) are too diffusive in the eastern North Atlantic to represent the mode water accordingly (e.g. NEW ET AL., 2001).

After 200 years of integration, the mean states have changed. In all experiments, the Subpolar Front is relocated to the north–west. The individual experiments have diverged

further from each other. The temperature distribution of the OMIP experiment at 40°W (Fig 5.1(b)) shows a broad northward NAC that turns east at 55°N. In the NAO+ experiment, this front is sharper and focused in the west, almost touching the central Labrador Sea on the way to the north (Fig 5.1(e)). As a result, the Labrador Sea is warmer than in the observations. East of 30°W, the NAC flows zonally towards the Norwegian Sea, depriving the Irminger Sea of warm water inflow. The NAO− experiment also shows a front south of Greenland, but it is not as sharp as in the NAO+ experiment. The temperature distribution in the Irminger Sea is similar to that in the NAO+ distribution. The temperature in the Greenland gyre is warmer in the mean of year 150 to 200 in all experiments. The NAO+ and NAO− experiments have temperatures above 20°C in the subtropical gyre, whereas the observations and the OMIP experiment reach only 18°C. In the Sargasso Sea, 18°C mode water forms and is clearly visible in the observations. This mode water is also present in the model results, but is warmer than observed. The structure of the subtropical gyre is close to reality and does not change dramatically during the long integration. The eastern North Atlantic is unusually warm at 20°N in all experiments. In the area of the Canary Current, strong equatorwards winds parallel to the coast lead to an enhanced offshore Ekman transport. The water which is missing at the surface has to be supplied by water from below in an upwelling motion. This upwelling of cold water is missing in all three experiments. A hint of this anomalous warm water at the North African coast is already visible in the early means (year 10 to 60), but it is more obvious in the mean distributions of years 150 to 200 (Fig. 5.1(b), Fig. 5.1(e) and Fig. 5.1(f)). A cell of cold water west of South America is in the observations. This is not present in the early years of the three experiments, but all the mean fields of years 150–200 show this relatively cold water in the south. Associated with this cold water cell is a better representation of the gradient between the cold water in the south and the warm water in the Sargasso Sea.

Fig 5.2 illustrates the salinity distribution at 300 m. The Subpolar Front separates not only warm and cold water masses, but also freshwater from the north and saline water from the subtropics, which is visible in the observation and model results 5.2. The general deficiencies of the salinity distribution are similar to the temperature distribution, but in addition the model shows much higher salinities than the observations almost everywhere. However, the most prominent model–data difference is the mode water in the eastern North Atlantic, which is not only noticeable in the temperature but also in the salinity distribution. Shortly after the beginning of the integration, the Subpolar Front has a more realistic position, where the NAO+ experiment displays the best agreement with measurements. This experiment also results in a large area of freshwater in the Labrador Sea. In the NAO− experiment, the front is located at 40°W, which reduces the amount of freshwater in the Labrador Sea.

After 200 years of integration, the subtropical gyre has become more saline in the NAO experiments than in the observations. The OMIP experiment has more reasonable values in the Sargasso Sea, but due to the missing upwelling of cold, fresh water at the coast of

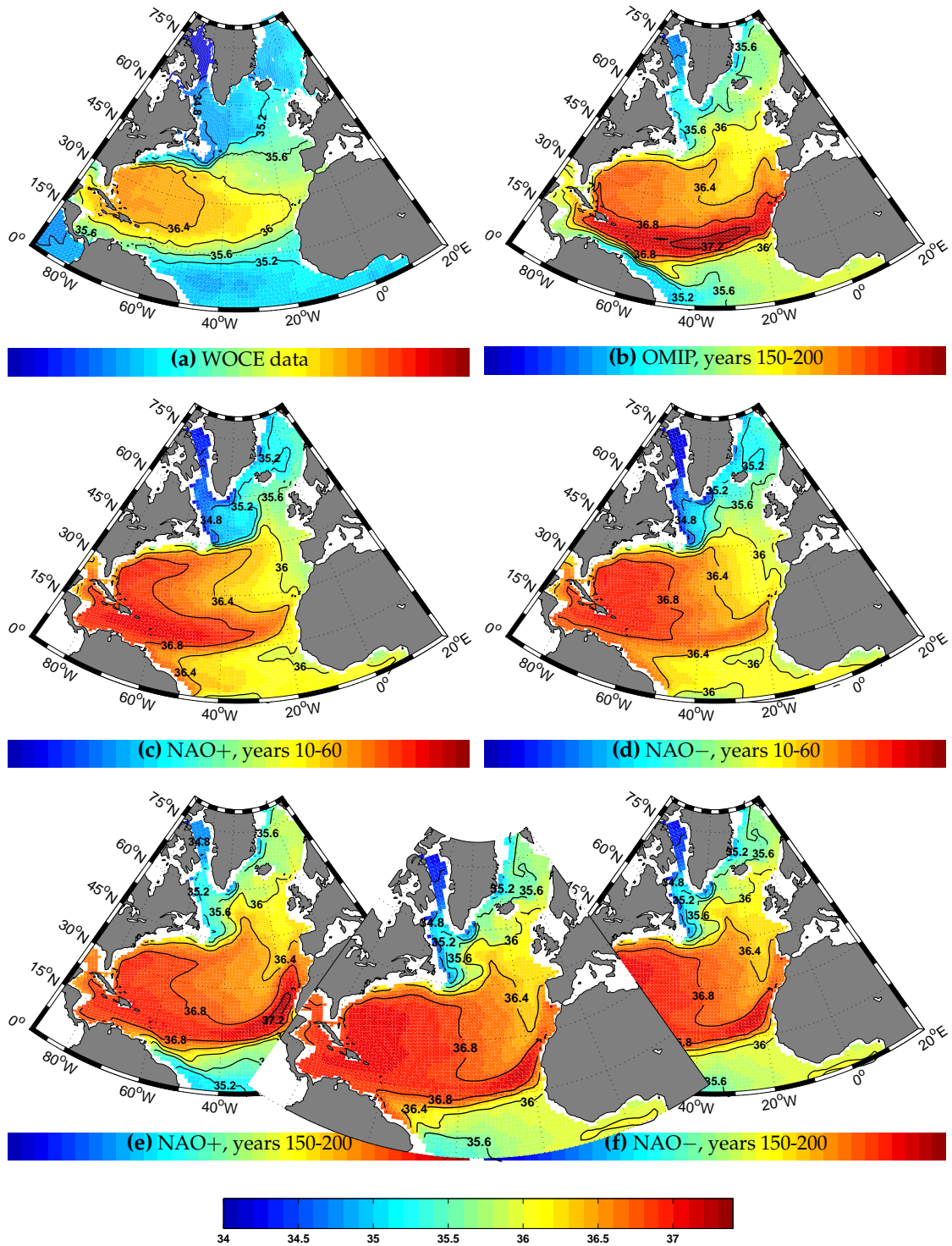


Figure 5.2: Salinity in 300 m depth of the North Atlantic, averaged over 50 years. a) The climatology of [Gouretski and Jancke \(1998\)](#), b) OMIP experiment, mean of years 150-200, c) NAO+ experiment mean of years 10-60, d) NAO- experiment, mean of years 10-60, e) NAO+ experiment mean of years 150-200, d) NAO- experiment, mean of years 150-200.

North Africa, there is a lens of very saline water in this area as well. The Nordic Seas and the Labrador Sea have in all experiments a much higher salinity than observations suggest, but the lens of fresher water north of the equator is more realistic after 200 years of integration than in the early years.

5.2 Circulation

The circulation of the three experiments reflects the tracer distribution. As a diagnostic for the circulation, consider the barotropic streamfunction, Fig. 5.3. It is defined as

$$\frac{1}{a} \frac{\partial \Psi}{\partial \phi} = - \int_{-H}^0 u dz \quad \text{and} \quad \frac{1}{a \cos \phi} \frac{\partial \Psi}{\partial \lambda} = \int_{-H}^0 v dz \quad (5.1)$$

The strongest gyre in all experiments is the anticyclonic subtropical gyre with the maximum of the streamfunction close to the North American coast, near Florida. In the north, the cyclonic circulation cell is the subpolar gyre. The positions of the gyre boundaries remain unchanged during the integrations of the individual experiments, but the strength and the position of the maximum of the circulation within the gyres change. The subtropical gyre is strongest in the NAO+ experiment. The mean field of years 150 to 200 has a maximum of 70 Sverdrup (1 Sv = $10^6 \text{ m}^3/\text{s}$). The maximum streamfunction values for all experiments are listed in Tab. 5.1.

	OMIP	NAO+	NAO-
Strength of subtropical gyre	51 Sv	70 Sv	65 Sv
Strength of subpolar gyre	-33 Sv	-37 Sv	-31 Sv
MLD in Labrador Sea, years 10 to 60	507 m	305 m	404 m
MLD in Greenland Sea, years 10 to 60	2722 m	2988 m	2426 m
MLD in Labrador Sea	1001 m	1972 m	628 m
MLD in Greenland Sea	1987 m	2453 m	2494 m
Max. meridional overturning	23 Sv	27 Sv	19 Sv
Max. northward heat transport	1.18 PW	1.46 PW	1.22 PW
Std. Dev. of the northward heat transport	0.13 PW	0.28 PW	0.17 PW

Table 5.1: Maxima of important quantities for the three spin up experiments for years 150 to 200, if not mentioned otherwise; MLD stands for the maximum of the mixed layer depth; the standard deviation of the northward heat transport at 20°N is calculated with the monthly mean values for years 150 to 200

As measured directly by SCHOTT ET AL. (1988), the Florida Current between Florida and Grand Bahama Island transports 20–40 Sv north. At 73°W, SCHMITZ AND MCCARTNEY (1993) estimated the transport of the Gulf Stream above 7°C with 67 Sv and below 7°C with 28 Sv. The values of Tab 5.1 represent the maximum of the vertically averaged

transport of the subtropical gyre, which is hard to compare to individual observations. NAO+ has a strong transport due to the strong windstress forcing of the westerlies at the northern boundary of the subtropical gyre (compare Fig. 4.1). The subpolar gyre is also strong in this experiment (more than 30 Sv) and its extent is large. In the NAO– and OMIP experiments, the maxima are reduced and the subtropical gyre is confined to a smaller region. The mean of years 10 to 60 of the NAO+ and OMIP experiments show the position of the maximum of the streamfunction of the subpolar gyre to be east of 35°W (not shown). In Fig. 5.3 this maximum has shifted to the west for years 150–200.

Convection depths can be represented via the depth of the mixed layer. The mixed layer depth is identified as the depth where the density difference to the surface is larger than $\Delta\sigma$. Here $\Delta\sigma$ is chosen to be $\Delta\sigma = 0.02\text{kg/m}^3$ in analogy with MCCARTNEY AND TALLEY (1982) and BÖNING ET AL. (1996). The mean mixed layer depths in

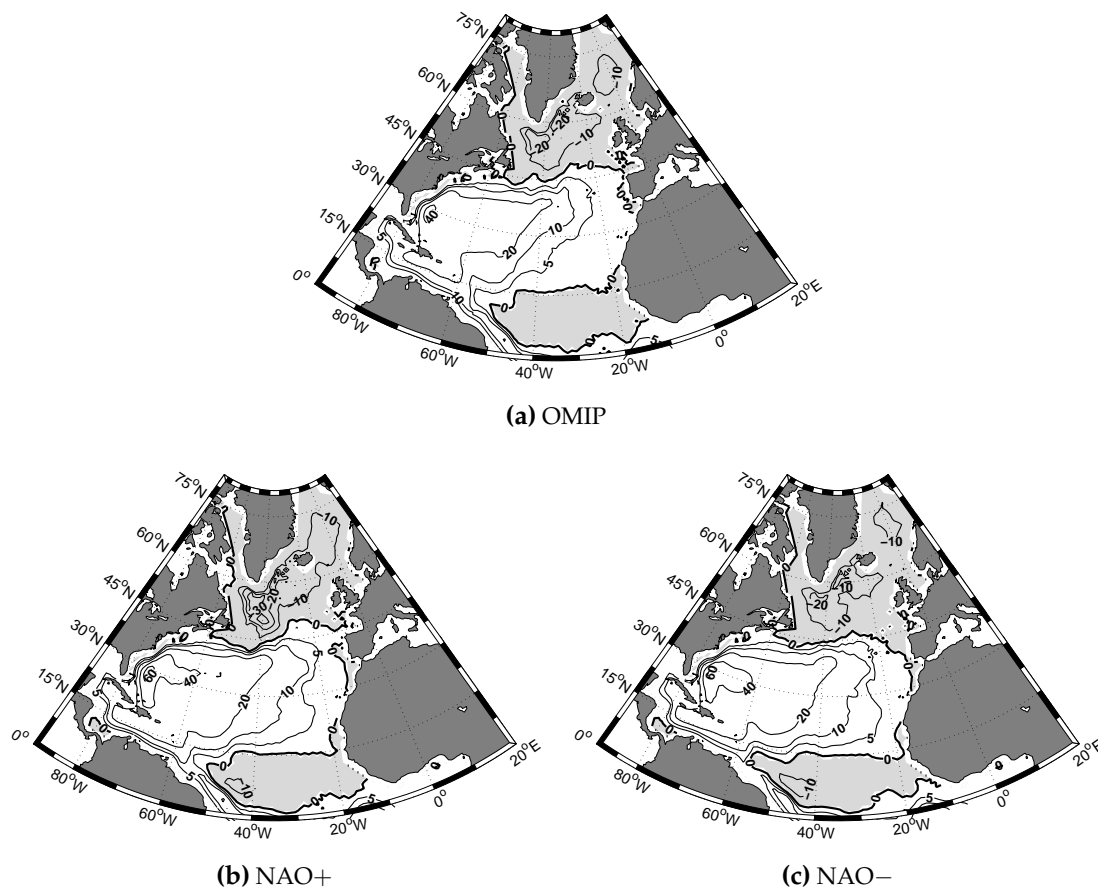


Figure 5.3: Mean vertically integrated streamfunction of the North Atlantic in Sverdrup ($1\text{ Sv} = 10^6\text{ m}^3/\text{s}$), averaged over the years 150 to 200. Areas of negative values are shaded; a) 50 year mean of OMIP experiment, b) 50 year mean of NAO+ experiment and c) 50 year mean of NAO– experiment.

March are shown in Fig. 5.4. The mixed layer depth criterion for the observations is $\Delta\sigma = 0.125\text{ kg/m}^3$ and the depths are restricted to the upper 1000 m. MONTEREY AND LEVITUS (1997) state that this criterion is more robust for climatological density data. All

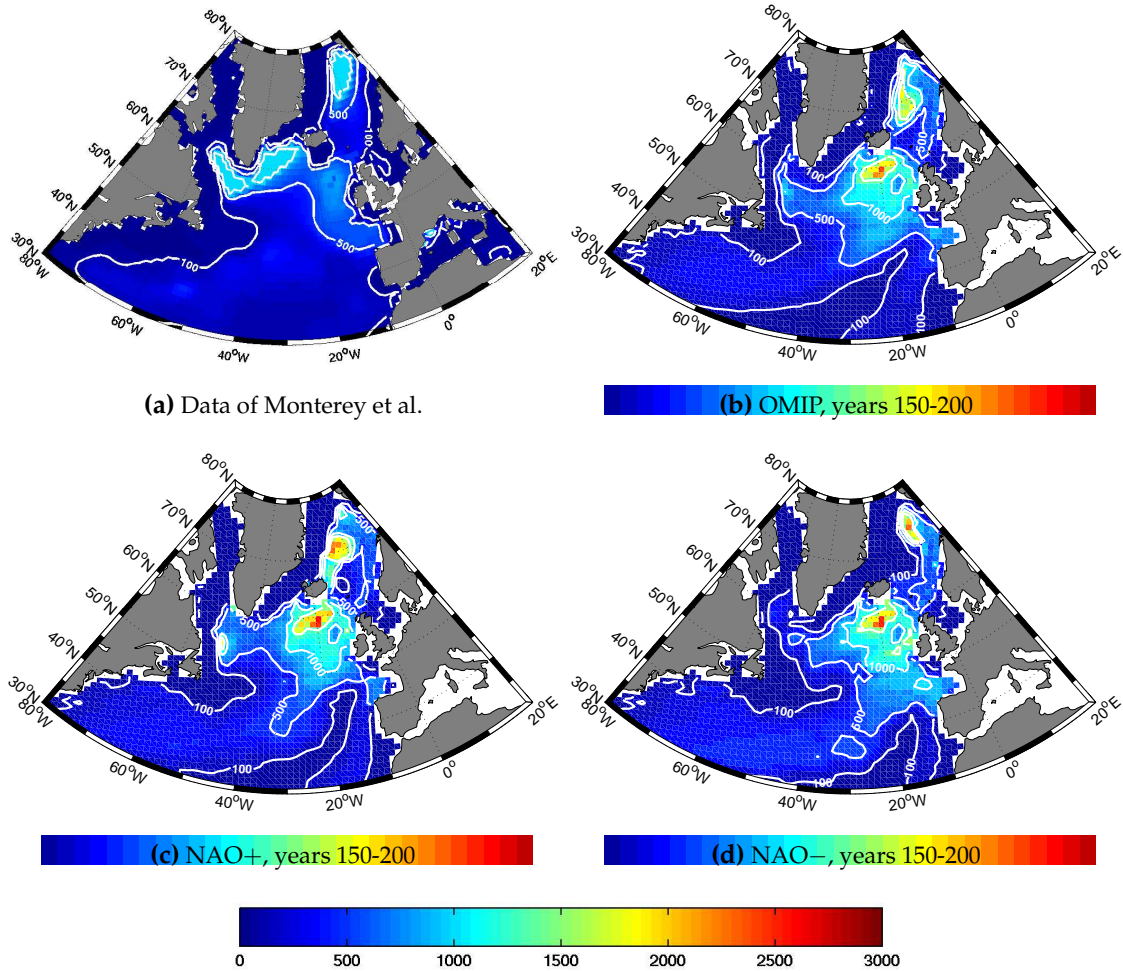


Figure 5.4: Mean mixed layer depth in March, averaged over years 150 to 200 (in metres); a) Climatology of March of MONTEREY AND LEVITUS (1997), b) 50 year mean of OMIP experiment, c) 50 year mean of NAO+ experiment and c) 50 year mean of NAO- experiment.

three experiments show an increase of mixed layer depths towards the north-east subpolar North Atlantic that corresponds to the observations (Fig. 5.4(a)). According to MCCARTNEY AND TALLEY (1982), this is the effect of continuously cooling along the NAC and the cyclonic circulation in the subpolar gyre that results in the formation of subpolar mode water. The maximum of this mixed layer strip is situated south of Iceland in the model results, whereas in the observations it is smaller and lies further south. This patch of deep mixed layers remains fairly unchanged throughout the integration.

In the Labrador Sea, the mixed layer depths are highly variable. In the mean of years 10 to 60 the mixed layer depth hardly exceeds a value of 500 m in any of the experi-

ments (compare Tab. 5.1). In the mean from years 150–200, the NAO+ experiment has the deepest mixed layer depths of almost 2000 m (Fig. 5.4(c)). In a wide area around this maximum, the mixed layers are deeper than 500 m. The situation of the mixed layer in the Labrador Sea is comparable to the OMIP experiment, but the maximum is shallower and deep mixed layers are restricted to only two grid boxes (Fig. 5.4(b)). In the NAO– experiment, the mixed layer reaches a maximum of only 630 m. In the surrounding areas, the mixed layer is shallower than 500 m, which is by and large a similar distribution as for years 10–60. The observations show mixed layer depths of 1000 m in the Labrador Sea. The deep mixed layer extends over larger areas. This could be the consequence of smoothing of the data. The observed deep mixed layers in the Irminger Sea are not present in any of the model experiments, because the freshwater transport with the East Greenland Current strongly stratifies over a large area.

The Nordic Seas show large differences in the location of deep mixed layers for the three experiments. The NAO+ composite reveals a deep mixed layer in the central Greenland Sea in the early and later mean fields, whereas the NAO– experiment has this deep mixed layer situated in the north of the Greenland Sea just south of Svalbard. The OMIP experiment has great mixed layer depths in the mean of years 10 to 60 (Tab. 5.1), but later only intermediate convection in the whole area, which is also the case in the observed mixed layer depths. The mixed layer depth at the coast of Norway is similar in all experiments.

The overall meridional transport can be described by the streamfunction of the zonally integrated volume transport, which is

$$\Phi(\phi, z) = \int_z^0 \int_{\lambda_W}^{\lambda_E} a \cos\phi v(\lambda, \phi, z') d\lambda dz'. \quad (5.2)$$

The meridional velocity, v , is integrated over depth and from the western (λ_W) to the eastern boundary (λ_E) of the model domain. a denotes the earth's radius.

North of the equator the trade winds generate Ekman transports that diverge and lead to a shallow upwelling cell in the NAO experiments. In Fig. 5.5, these equatorial upwelling cells are visible between 10°N and 20°N, reaching down to 200 m. The Ekman transports also produce two counter-rotating cells that meet at the Subpolar Front. They do not show up clearly in Fig. 5.5 because of the strength of the thermohaline circulation.

In the OMIP experiment, water in the upper 1000 m is transported to the north with the western boundary currents (North Brazil Current, Florida/Antilles Current, Gulf Stream and NAC). About 15 Sv of water sink down between the Greenland-Scotland Ridge and 60°N. This area is larger than observed, because of the coarse resolution of the model and parameterisation of the convection. The dense water is transported south as North Atlantic Deep Water (NADW) at depths between 2000 m and 3000 m. An additional enhancement of the meridional overturning cell is caused by downwelling at 45°N. The maximum in the cell is 23 Sv. It is located between 30°N and 40°N and at 1500 m depth (Tab. 5.1).

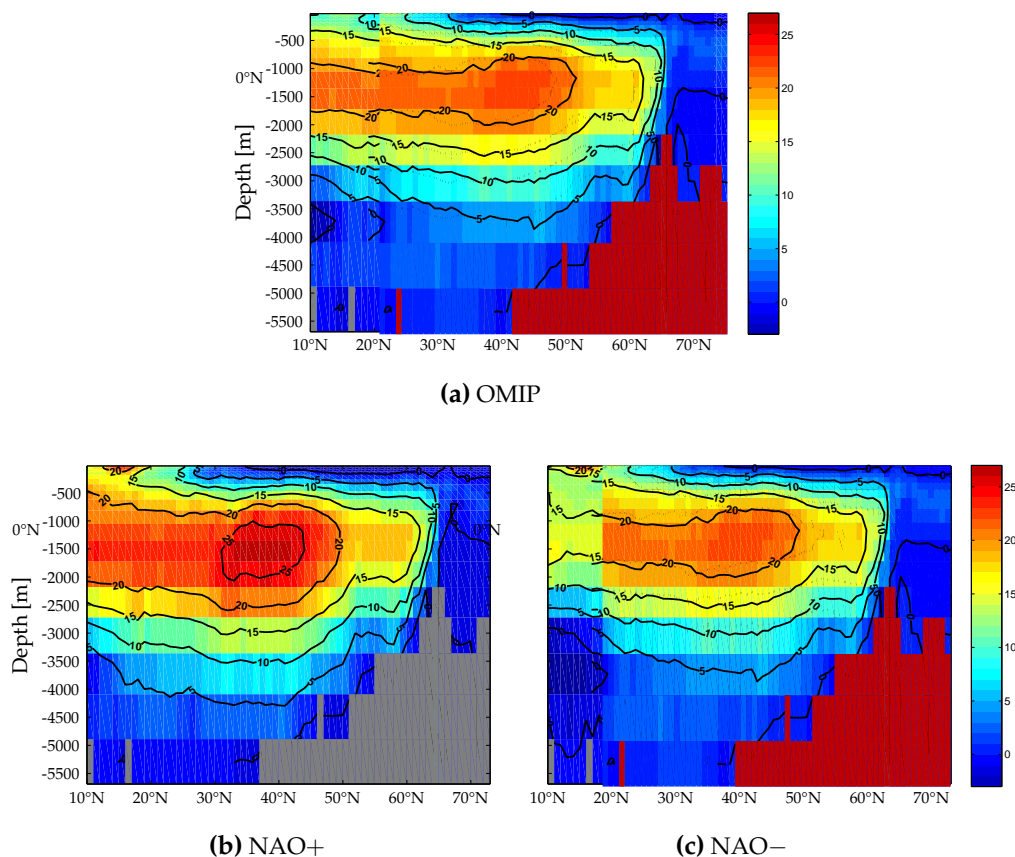


Figure 5.5: Mean zonally integrated overturning streamfunction of the North Atlantic, averaged over years 150 to 200 (in Sverdrup). a) 50 year mean of OMIP experiment, b) 50 year mean of NAO+ experiment, c) 50 year mean of NAO– experiment.

In the NAO+ experiment, the overturning cell is much stronger, with a maximum of 27 Sv, and the cell reaches further down. The lower branch of the deep water is located at 4000 m. The position of the maximum is the same as in the OMIP experiment.

The weakest meridional overturning is found in the NAO– experiment. Its maximum is 19 Sv, located at 35°N and 1000–1500 m depth. The lower branch does not reach as far down as in the other experiments. The Deep Western Boundary Current (DWBC)^{II} flows south between 2000 m and 3000 m, and there is still about 15 Sv of southward transport at 10°N. This is the only experiment where a cell of bottom water from the south enters the North Atlantic between 3500 m and 4500 m depth. It can be traced up to 20°N.

ROEMMICH AND WUNSCH (1985) determined, by applying inverse methods to data, a southward transport of NADW of 17 Sv at 24°N. The net deep water production rate was

^{II}NADW is a water mass with distinct temperature and salinity characteristic and DWBC is the name of the current which transports NADW

estimated with a different data set by GANACHAUD AND WUNSCH (2000) to be 15 ± 2 Sv. According to SCHMITZ AND MCCARTNEY (1993), 13 Sv of DWBC water cross the equator. The rate of deep water formation is then in the same range as the cross-equatorial transport. In OMIP and NAO+ the circulation is stronger than these estimations suggest, and only the NAO- experiment has comparable transportation rates. However, the magnitude and strength of the meridional streamfunction is hard to compare with observations, since there are no direct estimates of this integrated circulation.

5.3 Heat transport

The total advective meridional oceanic heat transport can be written as follows:

$$Q = \rho_0 c_p \int_0^L \int_{-H}^0 a \cos \phi v T dz d\lambda \quad (5.3)$$

The diffusive heat transport is small compared to this advective transport. The 50 years average of the advective northward heat transport is shown in Fig. 5.6. The latitudinal

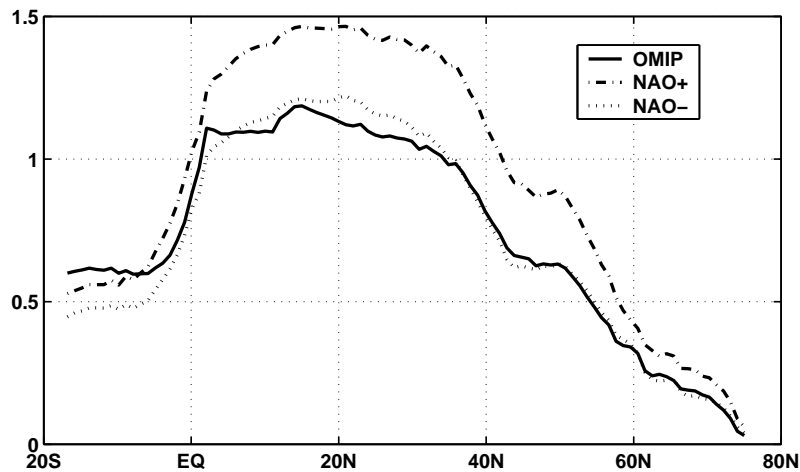


Figure 5.6: Northward heat transport as a mean over year 150 to 200 (in Petawatt, $1 \text{ PW} = 10^{15} \text{ W}$).

dependence of the northward heat transport in all experiments corresponds to substantial northward transport of heat over the equator with a maximum between 15°N and 20°N and a decline towards almost zero at the latitude of the Nordic Seas (75°N).

The OMIP experiment has a northward heat transport of 0.8 PW ($1 \text{ PW} = 10^{15} \text{ W}$) over the equator, reaching a maximum of 1.18 PW at 15°N (values listed in Tab. 5.1). 0.2 PW are transported north at 70°N . The NAO- experiment transports more heat to the north at 20°N than the OMIP experiment, but apart from that, the values are very similar in the North Atlantic in these two experiments. In the NAO+ experiment, the northward heat transport is strongest with 1.46 PW at 20°N (Tab. 5.1), and north of the equator the

Heat transport

transport is about 0.2 PW higher than in the OMIP or NAO– experiment. The heat transport in the North Atlantic at 24°N was estimated by [MACDONALD AND WUNSCH \(1996\)](#) to be 1.1 ± 0.3 PW and more recently by [GANACHAUD AND WUNSCH \(2000\)](#) to be about 1.3 ± 0.2 PW, both of these estimates are in good agreement with all three experiments.

The total advective heat transport is decomposed as suggested by [BRYAN \(1962\)](#):

$$Q = Q_{over} + Q_{gyre} = \rho_0 c_p \left[\int_0^L \int_{-H}^0 a \cos \phi \bar{v}^\lambda \bar{T}^\lambda dz d\lambda + \int_0^L \int_{-H}^0 a \cos \phi \overline{v'T'} dz d\lambda \right], \quad (5.4)$$

where \bar{v}^λ denotes a zonal average and v' is the deviation from this average. The first integral gives the transport due to correlations in the vertical, called the overturning component, and the second integral gives the transport due to correlations in the horizontal plane, called the gyre component. The diffusive heat transport is small compared to the total advective heat transport. The decomposition is illustrated for the three experiments in Fig. 5.7. South of the equator, in the NAO+ and NAO– experiments, the gyre com-

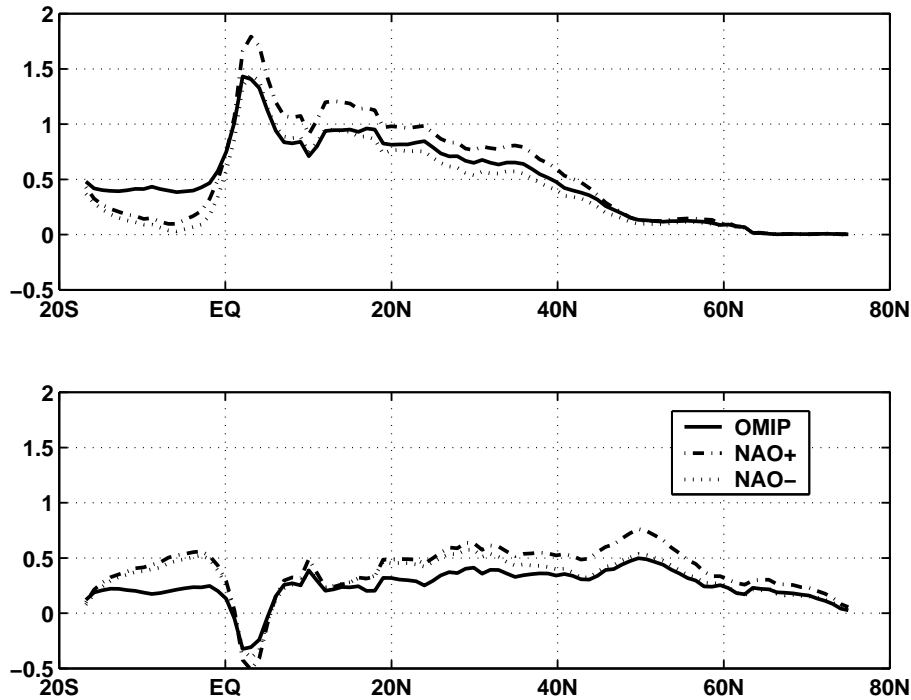


Figure 5.7: *Decomposition of the northward heat transport as a mean over year 150 to 200 (in Petawatt); the upper panel shows the overturning component, the lower panel the gyre component of the total advective heat transport*

ponent dominates, whereas in the OMIP experiments, the overturning component is the most important. It is obvious, that the main contribution to northward heat transport between the equator and 45°N comes in all experiments from the overturning component. At 50°N, both components have the same strength and north of this latitude the heat transport is governed by the gyre component.

The variability of the total advective heat transport at 20°N for the NAO– experiment is depicted in Fig. 5.8. 20°N is the position of the maximum northward heat transport.

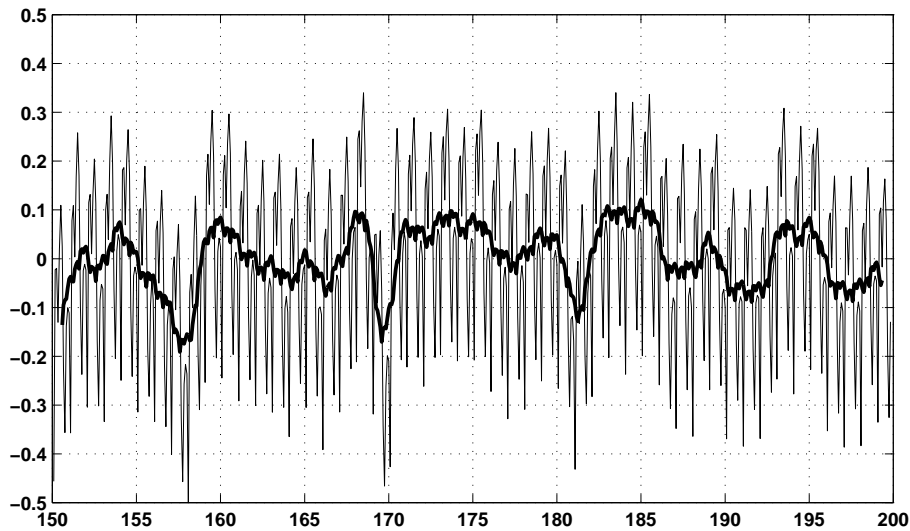


Figure 5.8: *Anomaly of the northward heat transport of NAO– for the years 150 to 200 as monthly means at 20°N (in Petawatt); the thick line is a running mean over 13 months*

The standard deviation of the heat transport in this experiment is 0.17 PW, which is 14% of the mean value. The mean value is superimposed with seasonal and decadal variability. The seasonal variations are mainly caused by changes in the Ekman transport. The forcing does not contain components with longer than seasonal period. The longer time scale variability in the heat transport depicted in Fig. 5.8 is due to internal variability of the ocean model. The other experiments show also seasonal and decadal variability, with standard deviations as listed in Tab. 5.1.

5.4 Ice distribution

The ice field depends strongly on the atmospheric conditions. On time scales shorter than one year, the motion of sea ice is mainly governed by wind stress; and only on longer time scales are the ocean currents roughly as important as the wind stress (RIGOR ET AL., 2002). As discussed in section 4.2, there is a significant difference between the wind stress distributions of the NAO+ and the NAO– composites, which ought to have an impact on the sea ice distribution and motion. The mean sea ice motion for the three experiments is shown in Fig. 5.9 as the ice velocity times thickness.

The NAO– experiment (Fig. 5.9(c)) reveals an enhanced sea ice motion from the Beaufort Sea to the East Siberian Sea. The Beaufort gyre itself is stronger because of the sustained anticyclonic wind stresses throughout the year in this composite as discussed in section 4.2. The sea ice accumulates in the central Arctic Ocean, where the sea ice thickness increases. The sea ice export through the Fram and Davis Straits is reduced as can

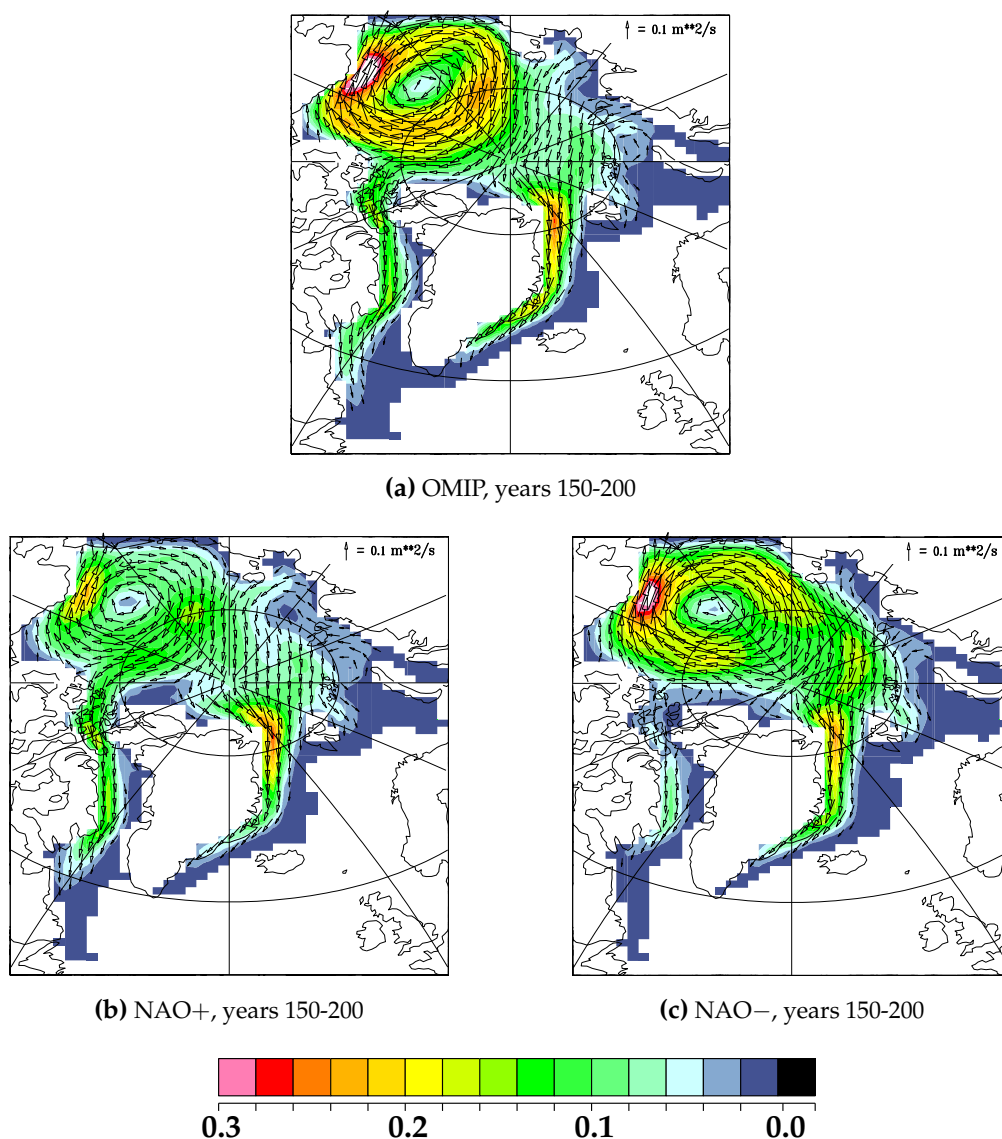


Figure 5.9: Mean ice transport averaged over year 150 to 200 (in $\bar{u}h$)

be seen in Tab 5.2. The transport of sea ice from the Kara and Laptev Seas to the central Arctic Ocean is small in the NAO- experiment, because of the weaker offshore wind stress. However, the ice export between Svalbard and Novaja Semlja is supported by the wind stress.

The NAO+ composite (Fig. 5.9(b)) has only weak wind stresses over the Beaufort and Bering Seas. The Beaufort gyre is therefore confined to the western Arctic Ocean and is less pronounced than in the NAO- experiment. On the Siberian coast the situation is reversed. Stronger offshore winds over the Kara and the Laptev Seas favour sea ice production and northward transport, but the sea ice does not accumulate in the central Arctic

ocean. The predominant winds between Svalbard and Novaja Semlja prevent the sea ice from being transported southwards into the Barents Sea. Instead, it is exported mainly through the Fram Strait into the Nordic Seas, additionally forced by strong southerly wind stresses north of the Fram Strait (Tab. 5.2). The axis of the transpolar drift is shifted to the west into the Beaufort Sea in this experiment. The export through the Davis Strait is strongly enhanced, mainly because of the southerly wind stresses over this strait. The sea ice volume is smaller than in the NAO– experiment, which can be attributed to the substantial ice export through the Davis and Fram Straits and to the wind stress at the Eurasian shelf, where the sea ice is blown away from the coast.

In the OMIP year, the anticyclonic wind stresses over the Beaufort Sea are even stronger than in the NAO– composite (not shown). As a result, the sea ice motion in the Beaufort gyre is very strong. On the Siberian coast, the offshore winds in the Kara and Laptev Seas are comparable to those in the NAO+ composite, thus sea ice is formed in the open leads and exported to the central Arctic Ocean. The strong Beaufort gyre prevents the accumulation of the sea ice north of Greenland and the ice export through Davis Strait is enhanced, whereas the ice export through the Fram Strait is reduced compared to the NAO+ experiment

5.5 Discussion

The only difference between the three experiments is the atmospheric forcing. The numerical parameters of all experiments are identical and even the initialisation is the same. But different forcing alone causes large differences in the circulation and sea ice distribution of the model.

In the NAO+ experiment, the horizontal circulation, the meridional overturning and the meridional heat transport are very strong compared to other model results and observations. The convection in the Labrador Sea is strong in times of positive NAO, consistent with [DICKSON ET AL. \(1990\)](#) and [KHATIWALA ET AL. \(2002\)](#). This is caused by strong winds in the Labrador Sea and the related thermohaline surface fluxes. The wind stresses of the OMIP year are comparable to the NAO+ composite in the mid latitudes,

	OMIP	NAO+	NAO-
Fram Strait	3055	3202	3025
Barents Sea Opening	400	247	510
Davis Strait	1568	1589	476
Denmark Strait	1011	414	477
Ice volume	33.5	33.4	38.5

Table 5.2: Mean ice export through miscellaneous straits in km^3/yr and mean ice volume of the whole ice covered area in 10^3km^3 ; all for years 150 to 200

but of lower magnitude as discussed in section 4.3. The period out of which the OMIP year was taken comprises mainly NAO+ years. As a consequence, the resulting distributions of tracers and the streamfunction in the northern North Atlantic fall between the NAO+ and the NAO− experiment results. This is visible in the meridional overturning and also in the strength of the subpolar gyre. In the subtropical North Atlantic, however, the wind stresses of the OMIP year are even lower than in the NAO− composite, which results in a weaker horizontal circulation compared to the NAO experiments. The subtropical gyre is reduced in strength and the gyre component of the meridional heat transport is lowest here among the experiments. The situation is again different in the Arctic Ocean. The anticyclonic wind stresses over the Beaufort gyre are strongest in the OMIP year, leading to an increased sea ice motion. This resembles the sea ice motion of the NAO− experiment. However, over the Eurasian Shelf, the strong offshore winds of the NAO+ composite are present in the OMIP year. Thus the position of the transpolar drift is similar in the OMIP experiment and the NAO+ experiment. In summary, the OMIP year resembles neither a NAO+ nor a NAO− condition, but is a mixture of both.

During the temporal evolution of the long spin up integration important features change in the northern North Atlantic, such as the position of the NAC. In the mean distribution of the temperature and salinity in the early years (10-60), the NAC is found in the western North Atlantic in the NAO− experiment, whereas in the NAO+ experiment the position is shifted to the east. This large range of variability is reduced after 200 years of integration, when the NAC is confined to the western North Atlantic in all experiments. Also, the water masses north of the Subpolar Front are warmer and more saline compared to the early years and to observations. This is the same in all three experiments. The tracer distribution in the subtropical North Atlantic, on the other hand, is closer to the observations after 200 years. The adjustment of the upper layer tracer fields to the atmospheric forcing should happen rapidly at low latitudes because the important adjustment processes are very fast. Thus, the long term change must be due to an adjustment process in the layers beneath the thermocline. The variability of the Gulf Stream position is underrepresented in this model (this will be discussed in detail in Section 7.3). This is because of the separation problem, which confines the Gulf Stream to the North American coast, leaving no room for variability.

The degree of variability of the model is most clearly visible in the time series of the maximum of the meridional overturning at 48°N and 1500 m depth, which is shown in Fig. 5.10. After an initial reduction of the meridional overturning in the first ten years, there is a long-term increase of the overturning in all three experiments. Thus, even if the previously discussed means of this period are in good agreement with observations, this overlying trend has to be taken into account. The most surprising result is the behaviour of the meridional overturning maximum in the OMIP experiment, which starts to oscillate after approximately 80 years of integration. This will be discussed in detail in chapter 7. The NAO experiments have similar values of overturning strength in the first 70 years, but afterwards the meridional overturning in the NAO+ experiments is sub-

stantially increased, whereas, in the NAO– experiments, the strength of the overturning increases more slowly. The standard deviation of the latter is 1.3 Sv for years 150 to 200, compared to 2.5 Sv in the NAO+ experiment. Possibly a certain strength of the meridional overturning must be reached to enable a strong internal variability in the model. OMIP and NAO+ pass this threshold, but in the NAO– experiments the overturning remains too small.

The spin up integrations are necessary to give the model time to adjust the circulation and stratification to the imposed atmospheric forcing. The surface currents adjust faster than the deep circulation, where the velocities are very small. Thus, after an integration of the order of 100 years we expect the regions of the ocean to be in equilibrium with the forcing that are ventilated by relatively swift currents, namely the near surface ocean and the subtropical and subpolar mode waters, including the Labrador Sea Water. It should be noted that many circulation features associated with the THC, like the meridional overturning, adjust to changes in the surface forcing on a time scale of decades because the meridional overturning is governed by western (and eastern) boundary layer currents. While the meridional overturning is part of the mechanisms that are responsible for the ventilation of the global deep ocean, it is only indirectly (through the changes of background stratification) coupled to the renewal time scale of the deep ocean.

It is interesting to note that the spin up integrations for most model integrations of the North Atlantic Ocean circulation are shorter than 100 years. For example, [HÄKKINEN \(1999a\)](#) starts sensitivity simulations for the GSA with a coupled-ocean sea ice model of the North Atlantic and the Arctic Ocean after a ten year spin-up. The temporal evolution of the meridional overturning to changes in the thermohaline forcing near the Greenland-

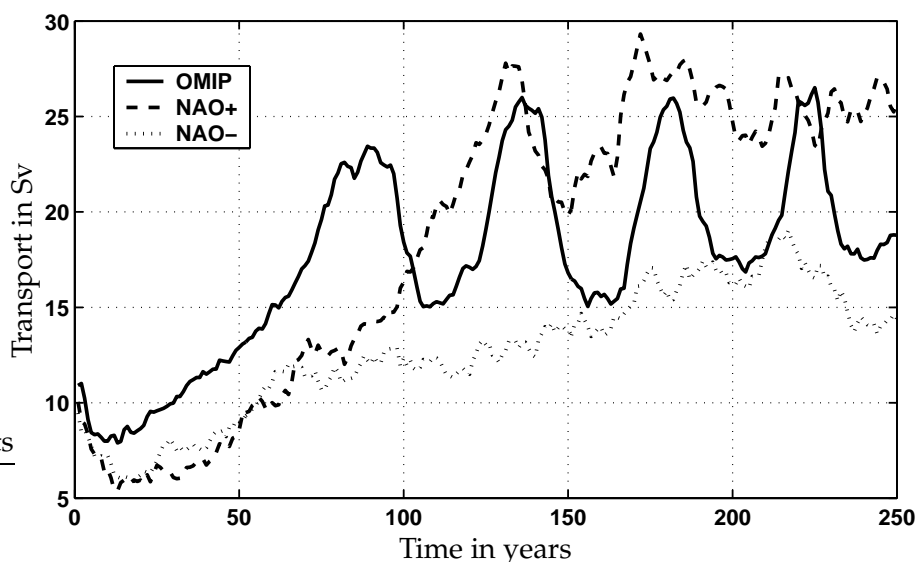


Figure 5.10: Annual mean of the maximum of the meridional overturning at 48°N and 1500 m depth for 250 years of the three experiments (in Sverdrup)

Scotland Ridge^{III} was examined by DÖSCHER ET AL. (1994) with an ocean model of the North Atlantic showing an adjustment to quasi-dynamic equilibrium within 10–15 years. Similar simulations were conducted by GERDES AND KÖBERLE (1995) with a model of the North Atlantic and Arctic Ocean. In that study, the 10th integration year was taken as a start for the discussion. EDEN AND WILLEBRAND (2001) use a 50 year integration period of an ocean model of the Atlantic from 70°S to 70°N to study decadal variability. A global ocean–sea ice model is used by HAAK ET AL. (2003) for simulations of the GSA. A period of 50 years was repeatedly integrated and for the analysis, the first two cycles (100 years) were neglected because of the model spin up.

The individual characteristics of each model and the employed surface forcing make it necessary to choose individual time scales for the spin up period. For example, regional models are constrained by lateral boundary conditions and contain smaller volumes (as the global ocean) and thus shorter renewal times. This justifies shorter spin up calculations. In our model study, we look at the average of the years 10 to 60 with the spin up times of comparable model studies in mind. The temperature and salinity fields at that time are still close to the initial data. The variability of the overturning time series in Fig. 5.10 makes it clear that the model is still not adjusted to the boundary conditions during this period.

The sensitivity experiments which have been conducted throughout this study depend strongly on the mean state and the internal variability of the model and therefore it is important to choose reasonable starting conditions. Year 200 of the NAO+ experiment is chosen as this starting point. At this time, the long-term trend abates and the internal variability has settled into a regular oscillation. The following ten years are characterised by a standard deviation of 0.35 Sv corresponding to the calmest period in this run. Thus the response of ocean and ice to changes in the atmospheric forcing is probably least affected by internal variability. Though it is not possible to separate the two influencing factors (external forcing and internal variability), year 200 of the NAO+ experiment is, under these considerations the best time for the sensitivity experiments. Although the decadal trend is small, it should be kept in mind that the experiments start in a phase of internal oscillation with minimum overturning and minimum meridional heat and salt transport.

^{III}northern boundary of the model

6 Sensitivity experiments

The North Atlantic Oscillation (NAO) is the dominant pattern of decadal to interdecadal variability over the North Atlantic (HURRELL, 1995). The NAO index defined as the sea level pressure difference between the Azores High and the Iceland Low as described by CAYAN (1992). This atmospheric mode is linked to a large variety of variability in atmospheric fields like changes in storm tracks (ROGERS (1997) and HURRELL (1995)) and precipitation over Europe, as well as in sea ice and oceanic parameters. The reaction of sea ice to the NAO was investigated by HU ET AL. (2002) and DESER ET AL. (2000) with the focus on sea ice extent. KWOK AND ROTHROCK (1999), DICKSON ET AL. (2000) and HILMER AND JUNG (2000) linked ice export through the Fram Strait to the NAO. The motivation for this study is the abrupt transition from NAO+ conditions in 1995 to NAO- conditions in 1996 (Fig. 6.1) the consequences of which can be observed in various phenomena: The Subpolar Front between Ireland and Greenland retreats to the west (BERSCH ET AL., 1999), the upper ocean in the western North Atlantic warms anomalously (REVERDIN AND VERBRUGGE, 1999) and the sea level height is raised in the subpolar gyre. ESSELBORN AND EDEN (2001) explain this rise as due to an increase of the northward heat transport. A reduction in ice export through the Fram Strait also reflects the drop of the NAO index in the winter 95/96 (VINJE ET AL., 1998) (Fig. 6.1).

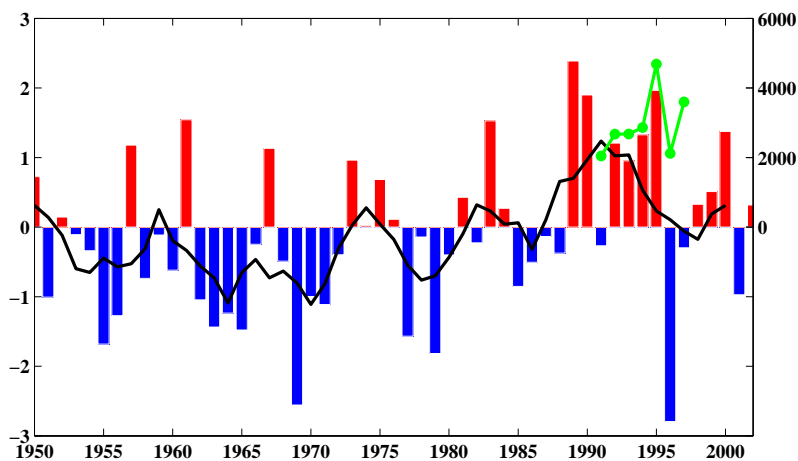


Figure 6.1: NAO Index (Dec - Mar): SLP difference Gibraltar-Stykkisholmur as defined by JONES ET AL. (1997) (updated); the black line is the running mean over five years; the green line denotes the ice export through Fram Strait as measured by VINJE ET AL. (1998) (in km^3/yr)

Here, the response of a coupled ocean–sea ice model to such a sharp transition in the atmospheric conditions is studied. We shall investigate the instantaneous (months to years) as well as the interannual to decadal adjustment processes in the model. By the design of the numerical experiments, the impact of the atmospheric conditions that relate to the NAO can be isolated from disturbances on other spatial and time scales.

In the first section, the experimental design of the sensitivity experiments is introduced. The response of the sea ice fields are presented in section 6.2.1 and, in section 6.2.2, the oceanic quantities are discussed. The results are discussed and summarised in the last two sections.

6.1 Design

Three experiments are presented which differ in the type of transition between NAO+ and NAO– forcing applied (Fig. 6.2). The model is spun up with NAO+ forcing for 200

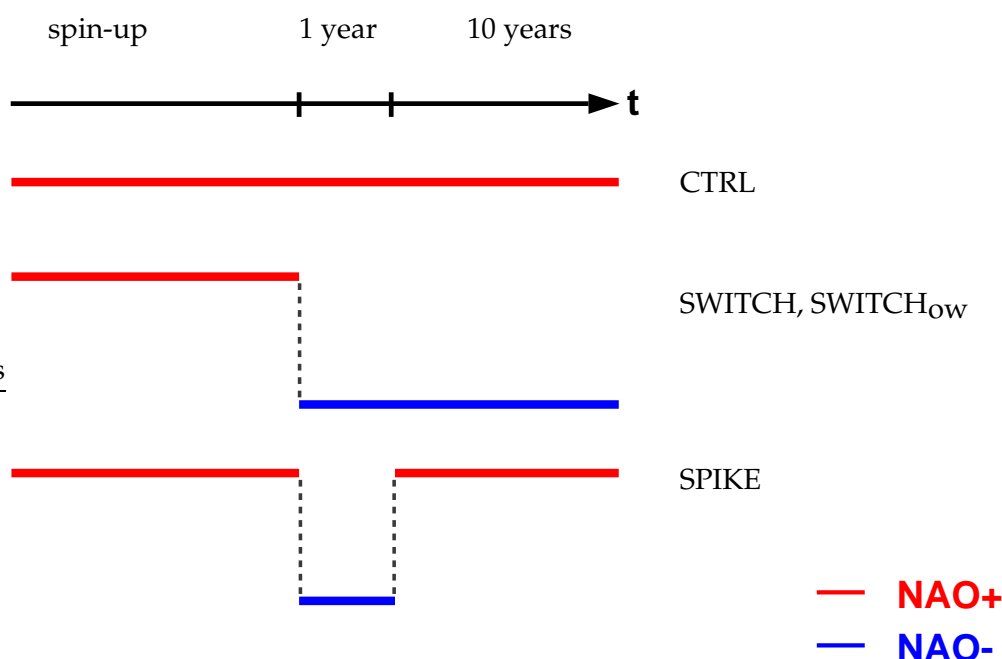


Figure 6.2: *Experimental design*

years and continued for 10 years (hereafter referred to as CTRL). The long spin-up was necessary because the maximum of the meridional overturning reveals an initial trend for almost a hundred years, followed by a period of large internal variability. At 200 years, the model is settled into the quasi-equilibrium. The forcing reflects the high NAO index state of the atmosphere that was predominant in the 1980s and 1990s. Moreover, this is a suitable spin-up for experiments that address the sudden change from relatively

long-term NAO+ conditions to NAO– conditions as occurred in 1995. This is an approximation as there is no reason to believe that the ocean is in an equilibrium with a real atmospheric forcing that is changing on all time scales. In the first sensitivity experiment, all atmospheric forcing fields are changed to the NAO– composite (after 200 years of spin-up) and calculated for ten more years. This experiment, called “SWITCH” from here on, should reveal the consequences of a sudden but sustained shift in the atmospheric conditions. In the second experiment, we try to separate the influence of wind stress field and thermohaline surface fluxes. In this experiment, which we call “SWITCH_{ow}”, only the wind stress field is switched to NAO–, while the other atmospheric quantities remain unchanged i.e. the NAO+ composite (ow stands for “only wind”). In the third experiment, the atmospheric conditions are switched from NAO+ to NAO– and after one year back to NAO+ again (“SPIKE” hereafter). This investigates the consequences of a sudden and short lived shift in the atmospheric circulation, similar to the observed shift of the winter 1995/1996 and the following recovery of the NAO. The switch is always applied in summer, because the differences in the wind stress and scalar fields between the composites are smallest at that time.

6.2 Results

6.2.1 Response of the ice fields

Sea ice reacts fastest to changes in the wind field, as long as the sea ice is thin or the sea ice cover is small (WALSH AND JOHNSON, 1979). Thus, we expect a rapid response to switches in NAO forcing along the ice margins in winter and over large areas of the Arctic in summer. The differences in the sea ice concentration between SWITCH and CTRL are represented in Fig. 6.3. The ice margin shifts to the south in the Barents Sea and in the Greenland Sea, whereas in the Labrador Sea, it takes a more northerly position. This dipole character of the sea ice cover response to the NAO–like forcing is consistent with observational results from DESER ET AL. (2000) and a combined model and observational analysis by KAUKER ET AL. (2003).

The wind stress direction in the northern opening of the Barents Sea favours enhanced ice advection from the central Arctic Ocean into the Barents Sea, where the ice covered area spreads further south (Tab. 6.1). Over the Greenland Sea, less sea ice melts because of the lower air and mixed layer temperatures which increase the sea ice cover. This shift is in good agreement with the observations of DICKSON ET AL. (2000), who found a reduction of the ice covered area between the sixties and the early nineties. The strong north-west winds over the Labrador Sea are much weaker in the NAO– years, hence cold outbreaks are absent and the sea ice margin is displaced to the north. This is evident in less sea ice formation in the northern Labrador Sea and less melting in the southern part. The influx of sea ice from the central Arctic Ocean through Davis Strait is much weaker than in CTRL (Tab. 6.1). In general, the sea ice extent as well as the ice volume are

Results

	CTRL	SPIKE	SWITCH	SWITCH _{ow}
Fram Strait	3500	3400	3000	2800
Barents Sea Opening	250	380	500	400
Denmark Strait	440	650	500	550
Davis Strait	1500	1100	500	750
Ice volume [10^3km^3]	29.8	30.5	33.8	31.8
Ice area [10^6km^2]	7.84	7.86	7.95	7.91

Table 6.1: Ice export to the south (in km^3/yr) and total ice volume and area after ten years (SPIKE values for the second year)

reduced in the Labrador Sea. The Beaufort gyre is stronger in this experiment, because of the sustained anticyclonic wind stresses. Thus the ice thickness increases by more than two metres in the East Siberian Sea and the central Arctic Ocean and is reduced by two metres at the coast of the Beaufort Sea (Fig. 6.4). This redistribution is similar to that discussed by [HOLLOWAY AND SOU \(2002\)](#) for the differences between the NAO– dominated 1960s and the NAO+ period in the 1990s. The differences in ice extent between the NAO+ and NAO– conditions are strongest in the summer months and very small in winter, where the ice cover is over 90% almost everywhere. The sea ice thickness of the previous winter governs the sea ice concentration of the following summer, due to a positive feedback during NAO+ conditions as documented by [RIGOR ET AL. \(2002\)](#), [HU ET AL. \(2002\)](#), [KÖBERLE AND GERDES \(2003\)](#) and [KAUKER ET AL. \(2003\)](#). This feedback

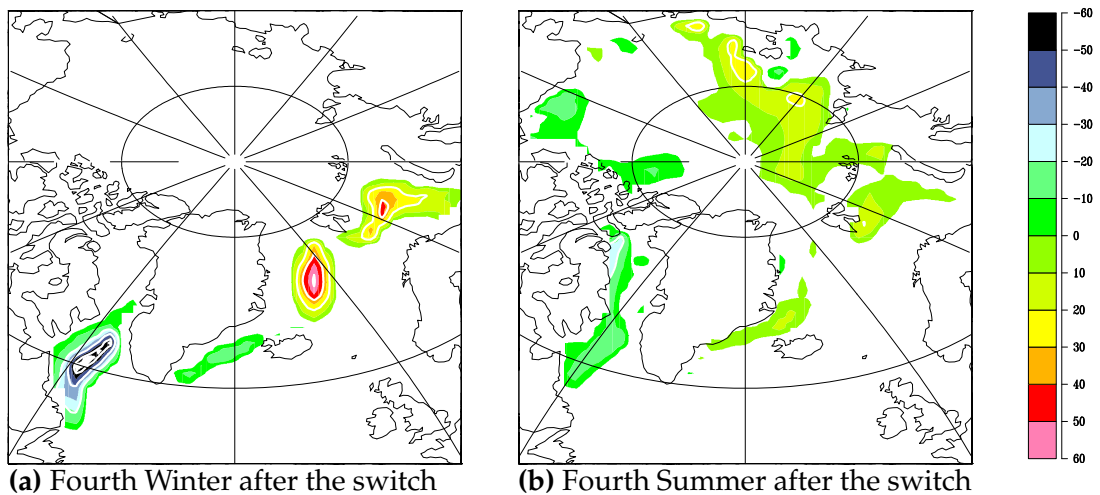


Figure 6.3: Difference of sea ice concentration between SWITCH and CTRL (in percent); contour interval is 20%, values less than 5% are omitted

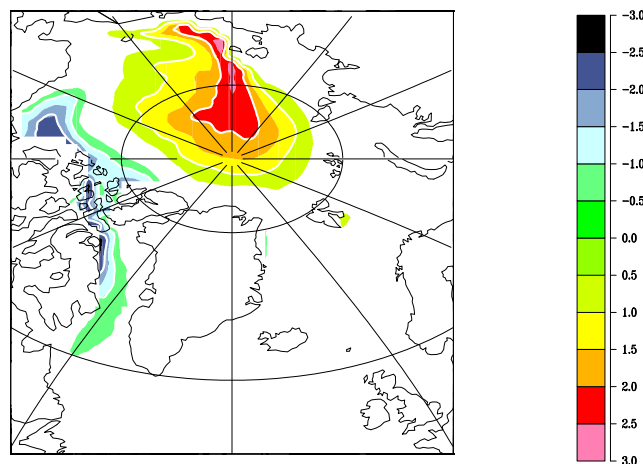


Figure 6.4: Difference of sea ice thickness between SWITCH and CTRL of the fourth year (in metres); contour interval is 1 m, values less than 0.5 m are omitted

is the ice–albedo temperature effect described in Section 2.1.4. This positive feedback is prevented in SWITCH and the sea ice can accumulate in the central Arctic Ocean over the years, resulting also in changes of the thickness distribution in the adjacent seas, such as the Barents Sea, and a reduction of the sea ice export through the Fram Strait (Tab. 6.1). A cold sea surface temperature anomaly (not shown) in the SWITCH experiment confirms the missing feedback. In the following summer, the sea ice thickness anomaly is increased by the advection of the Beaufort gyre. The thickness anomalies intensify over the ten years of integration, due to the advanced changes of the ocean mixed layer temperature, and converge at the end to $34 \times 10^3 \text{ km}^3$.

In the SWITCH experiment, the sea ice concentration in summer increases in the east Siberian Sea and the central Arctic Ocean. The strong off-shore winds of the NAO+ forcing are missing and the summer sea ice cover stretches to the coast in the Laptev and Kara seas. A negative anomaly in the Labrador Sea is caused by the reduced ice advection in this area, and the export through the Davis Strait is also reduced (Tab. 6.1). According to KAUKER ET AL. (2003) this distribution of the summer sea ice concentration is a lagged response to the sea ice thickness distribution of the previous winter.

The SWITCH_{OW} experiment has the same wind stress forcing as SWITCH, but all the other forcing fields are based on the NAO+ composite. The position of the sea ice concentration anomalies is quite similar to the SWITCH experiment (see Fig. 6.3a), but the actual values are modified by the different surface forcing. Compared to SWITCH, sea ice extent in the Barents Sea and the Greenland Sea is reduced due to the warmer air temperature in this area and warmer mixed layer temperature, which increases the lateral melting. Overall, the Arctic ice volume is smaller than in SWITCH due to higher air temperatures in winter (Fig. 4.4(a)). The thinner ice causes a reduced ice export through the Fram Strait and the Barents Sea (Tab. 6.1). The ice export through Davis Strait is reduced compared to the CTRL experiment, because the southerly wind stresses are reduced in

Results

strength.

The SPIKE run shows an enhancement in sea ice extent of $0.03 \times 10^6 \text{ km}^2$ for two years after the switch to NAO– conditions and it reaches the value of CTRL four years after the switch back to NAO+ conditions. Thus, ice cover reacts very quickly to the changes in atmospheric forcing, but there is also a longer time scale as heating of the ocean mixed layer retards the adaption of the sea ice volume back to the CTRL experiment.

The mean of the summer half year exhibits melting over the whole ice covered area, with the largest values in the vicinity of the sea ice margin, namely the Beaufort Sea, Davis Strait, Labrador Sea, Nordic Seas and the East Greenland Current. The differences between CTRL and SWITCH are shown in Fig. 6.5. The right panel shows the anomalous

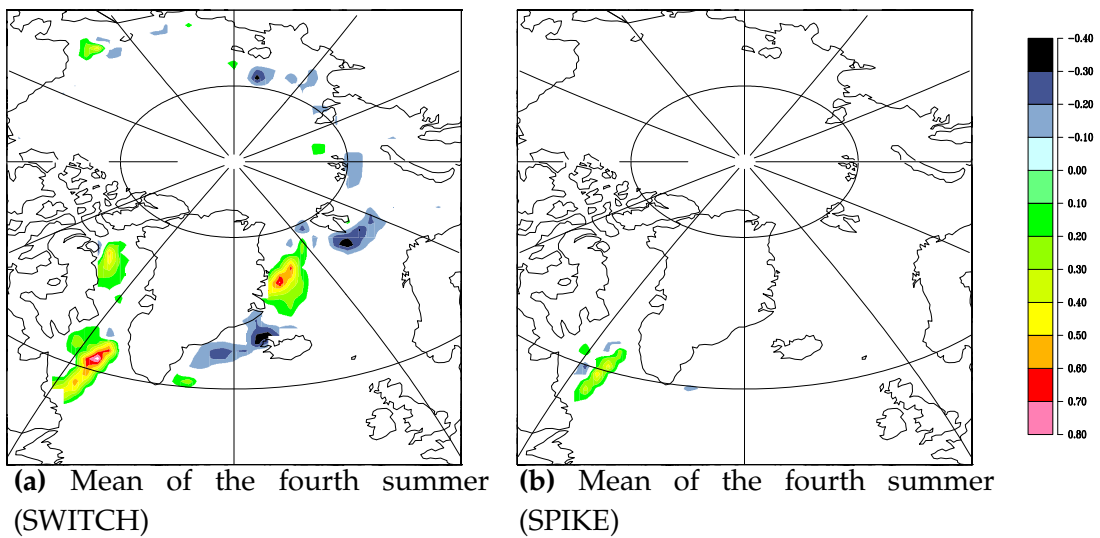


Figure 6.5: Difference of sea ice growth of SWITCH and SPIKE, relative to CTRL (in metres/month); values less than ± 0.1 metres/month are omitted

thermodynamic sea ice growth after switching back to NAO+ forcing in SPIKE. Since the atmospheric forcing is identical to the CTRL forcing, the persistent dipole anomaly in the Labrador Sea, which lasts for the subsequent ten years of calculation, is surprising. The sea ice margin in the northern Labrador Sea is permanently shifted to the north, with less than normal ice formation in the north and reduced melting in the south. The reason for the permanent shift must be found in the ocean. In the next section, we examine the reaction of the ocean to the NAO shift.

6.2.2 Response of the ocean fields

Overturning circulation

The overall meridional transport can be described by the streamfunction of the zonally integrated volume transport as shown in Eq. (5.2). The value of Φ at 48°N and 1500 m

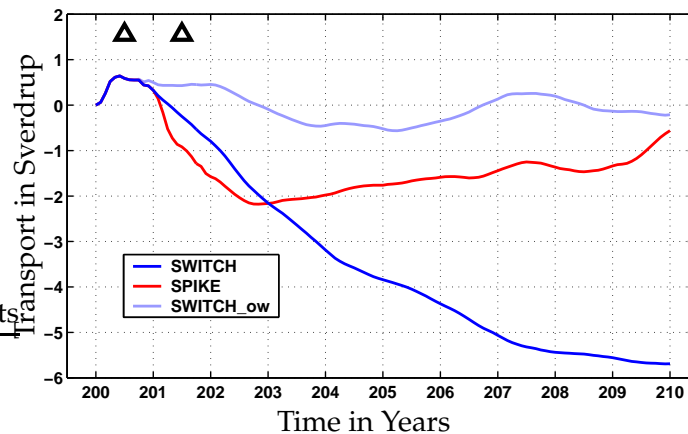


Figure 6.6: Deviation of the value of the streamfunction for the meridional overturning at 48°N and 1500 m depth from the CTRL (in Sverdrup). The time series are filtered with a thirteen month running mean; triangles mark the switch to NAO- forcing and the return to NAO+ forcing one year later in the SPIKE experiment (compare Fig. 6.2)

depth is representative for the total overturning across 48°N , which is near the southern boundary of the subpolar gyre. Its development is depicted in Fig. 6.6. The time series are filtered with a thirteen month running mean to remove the seasonal variations. The mean of the overturning in the CTRL experiment is 23.5 Sv. After the switch to NAO- forcing, the overturning increases immediately by half a Sverdrup, in all sensitivity experiments. This is due to the change in meridional Ekman volume transport in response to the changes of the zonal wind stress. In the vertical distribution of the zonally integrated mass transport (Fig. 6.7), there is a negative anomaly in the south with southward Ekman drift and a positive anomaly in the north (northward Ekman drift) and anomalous upwelling at 40°N . Below the Ekman layer, the streamfunction decreases linearly with depth to zero at the bottom, consistent with a barotropic compensation of the Ekman transport. EDEN AND WILLEBRAND (2001) performed a comparable sensitivity experiment and found a similar instantaneous reaction. The ocean response to NAO- is nearly symmetric with that to NAO+ in their experiments in agreement with the results presented here. The meridional overturning at 48°N drops below the CTRL value in year 201 and declines further to 6 Sv below CTRL at the end of the experiment. The baroclinic reaction to the changes of the forcing field includes a weakening of the basin-wide NADW cell of the overturning (Fig. 6.7b). In the top 300 m of the subpolar North Atlantic, the Ekman cell is visible as a reaction to the different wind stress forcing.

In the case of SWITCH_{ow}, we see baroclinic adjustment processes in the area of the subtropical Ekman cell (Fig. 6.8), a mechanism described by ANDERSON ET AL. (1979). At higher latitudes this mechanism is too weak or not present because of the low speed and strong damping of baroclinic Rossby waves. Here, the Ekman transport near the surface is still compensated by a more or less barotropic current after five years. The baroclinic

Results

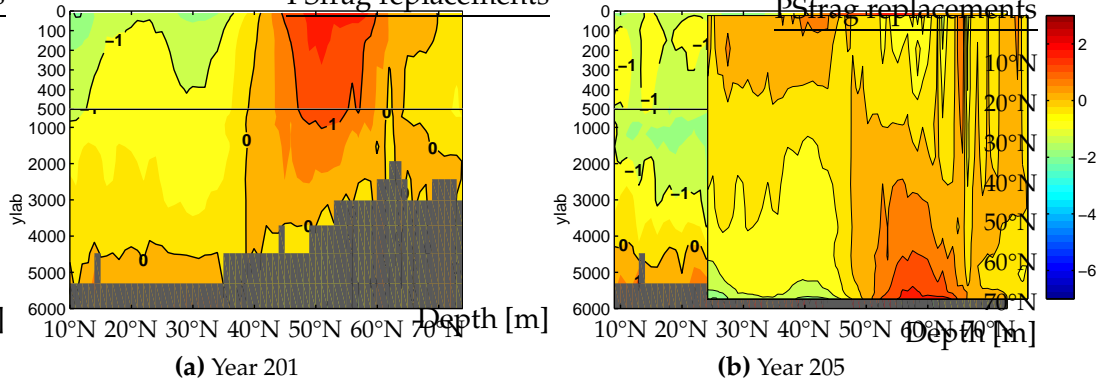


Figure 6.7: Annual mean meridional overturning of the SWITCH experiment as deviation from CTRL (in Sverdrup)

compensation in SWITCH must therefore be due to the effects of the thermohaline forcing, which differs in SWITCH_{OW} and in CTRL. The NADW cell in SWITCH_{OW} is slightly stronger because of the higher transport of subtropical water to subpolar latitudes. This enhancement results in increased water mass transformation and stronger sinking of dense water. The anomalies are small compared to the SWITCH experiment and the overturning at 48°N and 1500 m depth remains close to the value in CTRL (Fig. 6.6). Switching back to NAO+ forcing in the SPIKE experiment reduces the overturning as expected from the change in Ekman transport. However, following the switch back to NAO+ forcing, the overturning at 48°N drops below that of CTRL (Fig. 6.6). This reduction is associated with a permanent shift of the position of the convection in the Labrador Sea. This is also visible in the shift of the sea ice margin (compare Fig. 6.5, right panel). Forcing the model for only one year with NAO– forcing apparently moves the ocean to a different state of equilibrium. The slight shift in the location of convection hints at a

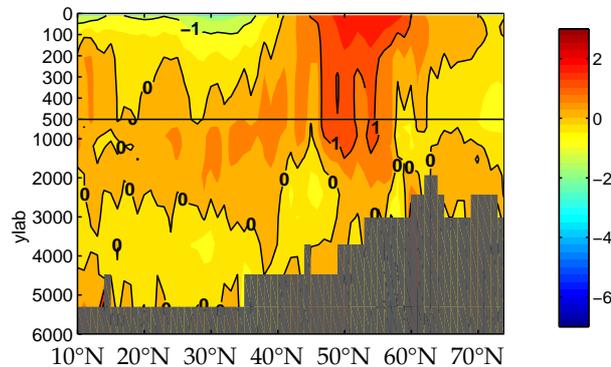


Figure 6.8: Year 205 of the annual mean meridional overturning of the SWITCH_{OW} experiment as deviation from CTRL (in Sverdrup)

mechanism first proposed by LENDERINK AND HAARSMAN (1994). According to these authors, the circulation induced by convection acts as a positive feedback that stabilises the new convection site. Convection shifts to a new location due to changes in the forcing. As these changes are taken back, the convection stays in the new position because of the feedback and the slightly changed background conditions.

Horizontal circulation

The baroclinic compensation mentioned above makes the response on the streamfunction in SWITCH increasingly compatible with the classic (non-topographic) Sverdrup relation (Fig. 6.9; EDEN AND WILLEBRAND (2001)) as the system responds with a substantial weakening of both the subtropical and the subpolar gyres (Fig. 6.9b-d) after a few years. Strong topographic influences are still present north of 40°N over the Mid-Atlantic Ridge. In the northern Labrador Sea, a negative streamfunction anomaly appears after two years, but it weakens rapidly after the fourth year.

The changes in the upper level flow after switching to NAO– forcing (illustrated by the velocity field at 100 m depth in Fig. 6.10) are characterised by a weakening of the Gulf Stream and the North Atlantic Current. The NAC turns north sharply just after passing the Grand Banks with the NAO– forcing of the SWITCH experiment. It continues zonally at approximately 55°W before it enters the Nordic Seas. The whole subpolar circulation becomes weaker in SWITCH, also affecting the flow of Atlantic water into the Arctic via the Barents Sea. On the other hand, the cyclonic circulation reaches further north in the Labrador Sea, an effect related to the shift in convection as discussed above. In the case of SWITCH_{OW}, the streamfunction anomaly of the first year is similar to that of the SWITCH run, but the reinforcement of the anomalies in the following years is much slower. In the Labrador Sea, the inflow from Davis Strait is weaker than in the CTRL, resulting in an enhanced circulation in the northern area as in the SWITCH experiment. Here, the negative streamfunction anomaly develops in the third year, as in SWITCH, but it is present until the end of the experiment.

Integrated potential energy

Looking at the integrated potential energy is helpful to understand which part of the surface forcing, the wind stress or the buoyancy flux, drives the barotropic circulation. The integrated potential energy is part of the forcing term of the equation of the depth-averaged flow as summarised by MERTZ AND WRIGHT (1992). SARKISYAN AND IVANOV (1971) introduced the idea that a combination of baroclinicity and sloping bottom topography can give a rise to a driving force for the depth-averaged flow. When vorticity advection and friction are neglected, the equation for the depth-averaged flow can be written as:

$$\nabla \cdot (H^{-1} \nabla \psi_t) = J \left(\frac{f}{H}, \psi \right) + J (\chi, H^{-1}) + \left[\nabla \times \left(\frac{\tau_s - \tau_b}{\rho_0 H} \right) \right]_z \quad (6.1)$$

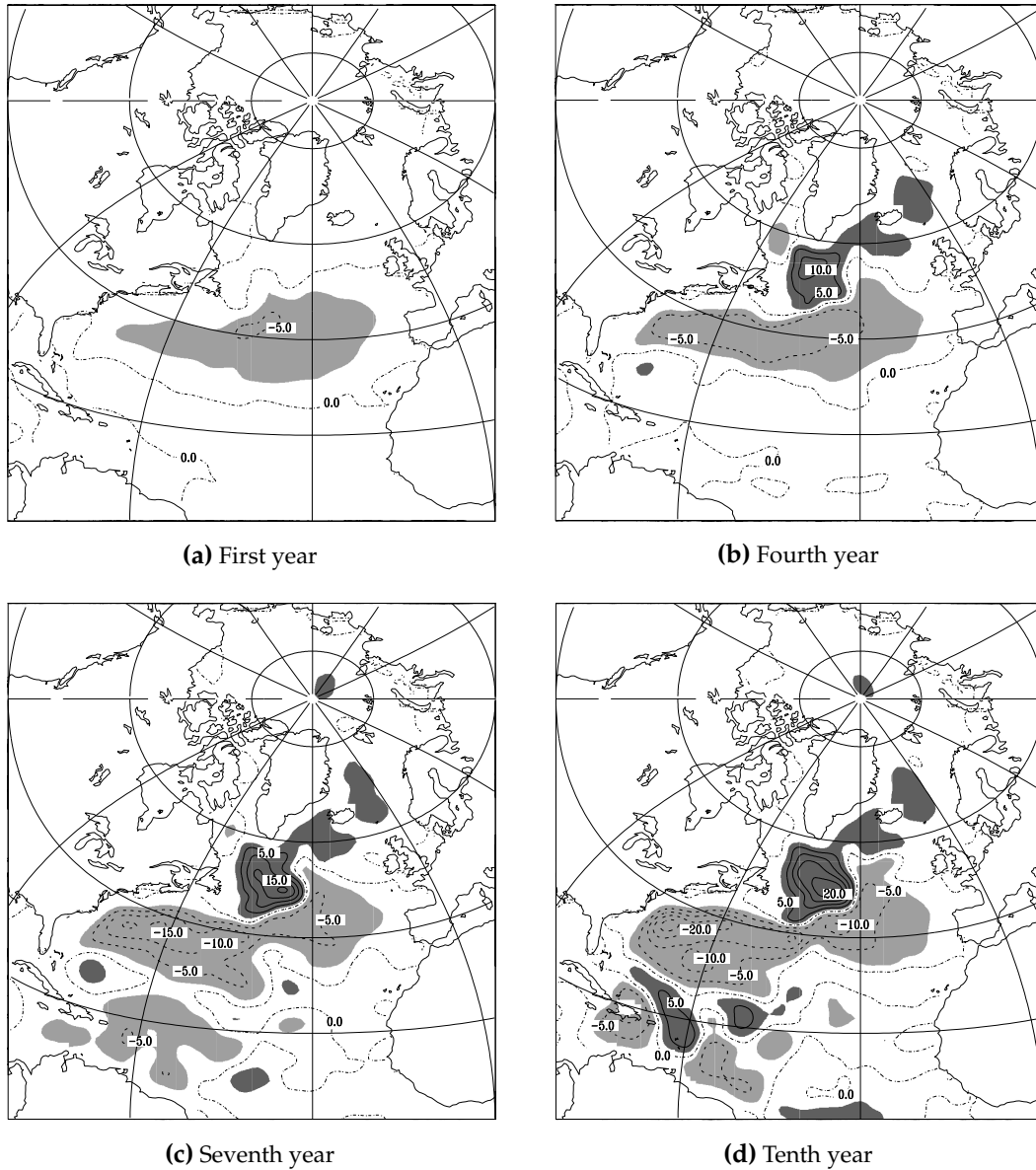


Figure 6.9: Difference between SWITCH and CTRL in the barotropic streamfunction with a contour interval of 5 Sv; values smaller than -2.5 Sv are lightly shaded, values larger than 2.5 Sv are heavily shaded

$H(\lambda, \phi)$ denotes the depth of water and χ is the integral of potential energy. ρ_0 is a constant reference density and $J(A, B) = (a^2 \cos \phi)^{-1} (A_\lambda B_\phi - A_\phi B_\lambda)$ is the Jacobi-Operator (with a , the earth's radius). The first term on the right hand side describes the transport across geostrophic contours (combining planetary and topographic vorticity), the second term is the JEBAR, which couples the baroclinic structure χ and the external mode over sloping bottom topography. In addition to the JEBAR term, the wind stress τ_s and the

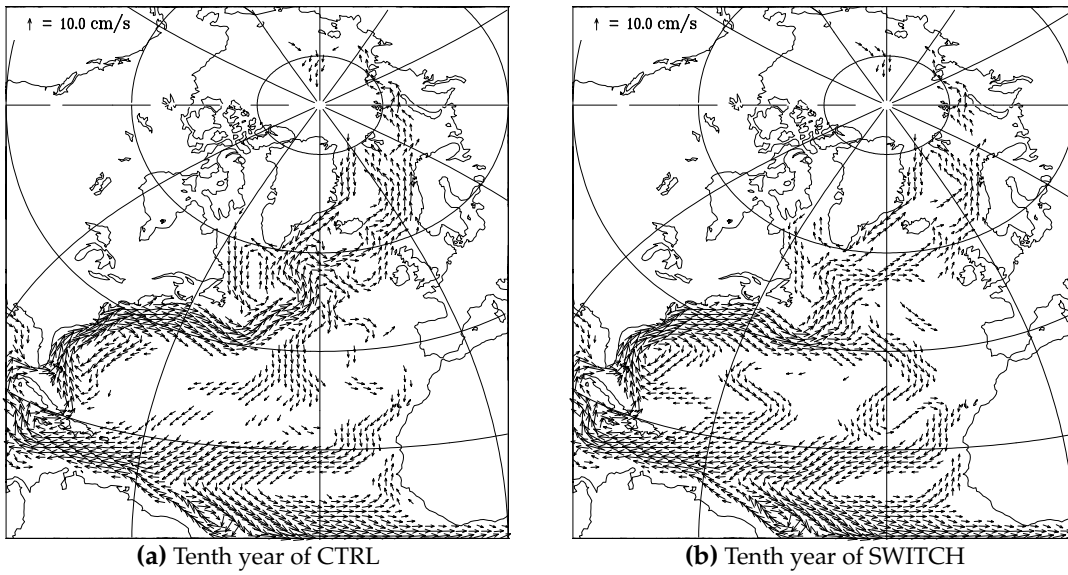


Figure 6.10: Annual mean velocity field in 100 m depth (in cm/s); values less than 1.0 cm/s are cut off, quadratic scale of arrow length

bottom stress τ_b can force the external mode directly. To simplify the equation, the time derivative is neglected as the external mode is regarded to be in a quasi-equilibrium state.

In the following, the density differences relative to CTRL are discussed for the experiments with the help of the anomaly of the potential energy integral $\delta\chi$ ¹:

$$\delta\chi = \frac{g}{\rho_0} \int_{-H}^0 z \left(\rho^{SWITCH} - \rho^{CTRL} \right) dz, \quad (6.2)$$

where g is the acceleration due to gravity. The annual mean differences of $\delta\chi/f_0$ between the CTRL and the SWITCH experiment are shown in Fig. 6.11. After a few years, when the baroclinic adjustment has taken place, the streamfunction ψ and $-\delta\chi/f_0$ are very similar. As seen in the meridional overturning streamfunction Φ for SWITCH and SWITCH_{OW} (Fig 6.7 and 6.8), baroclinic adjustment by baroclinic Rossby waves north of 45°N is too slow or too strongly damped to be important in the subpolar gyre. Here, other processes must be important for the change in density recorded in the potential energy field. The velocity at 100 m depth shows a small shift of the NAC to the west, accompanied by warmer sea surface temperature and saltier surface water west of 40°W, which strengthens in the subsequent years. The East Greenland Current transports fresher and colder water at the southern tip of Greenland compared to the CTRL run.

The separation between the wind forcing, which is included in the last term of Eq. (6.1) and the density field as the driving factor of the depth-averaged flow is not clear, because

¹the actual values of the JEBAR vary on rather small scales and are not very instructive

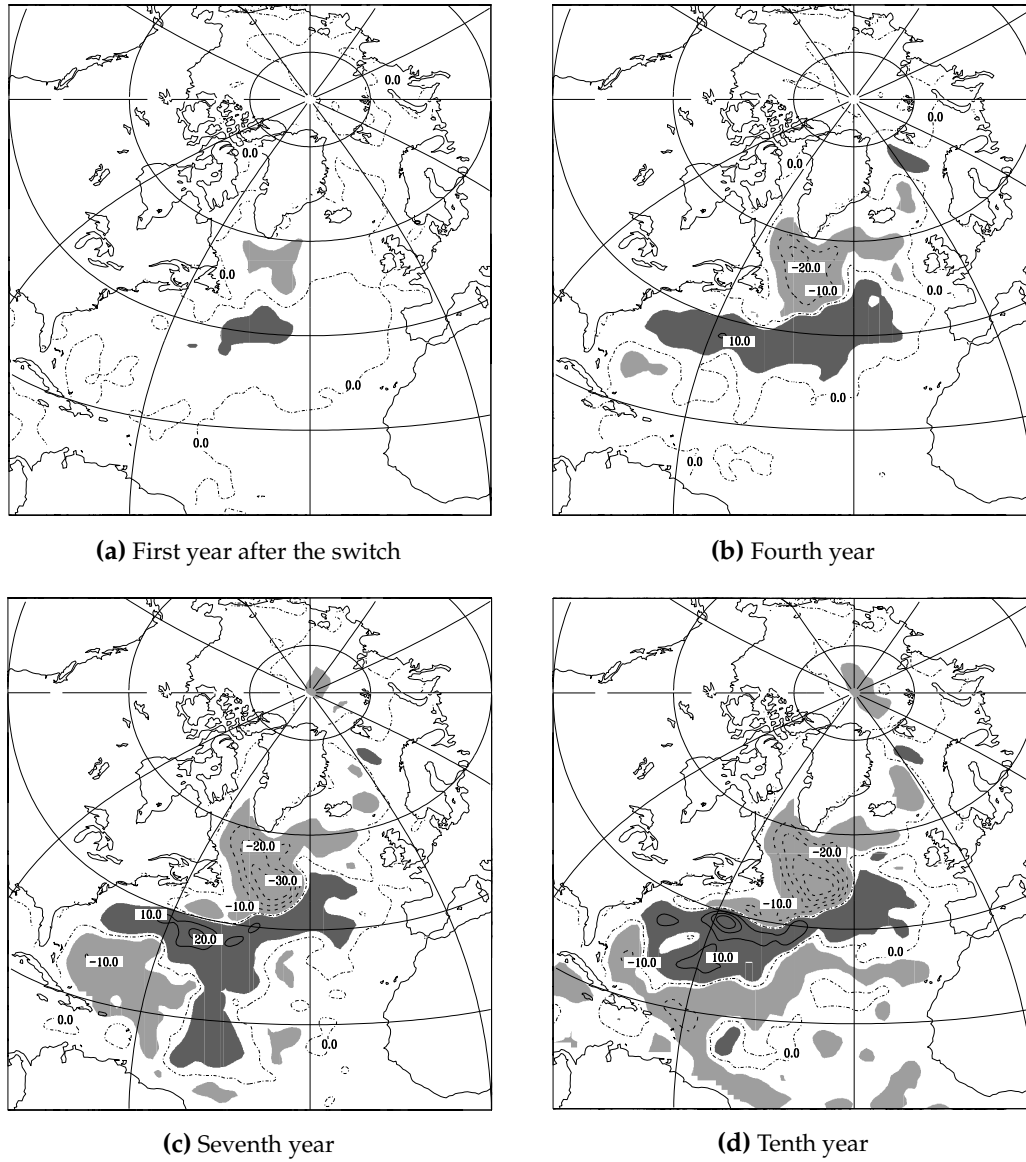


Figure 6.11: Annual means of the integrated potential energy anomaly ($\delta\chi/f_0$, where $f_0 = 2\Omega\sin(50^\circ)$) of SWITCH versus CTRL in Sverdrup (compare Eq. (6.2)); contour interval is 10 Sv; values smaller than -5 Sv are lightly shaded, values larger than 5 Sv are heavily shaded

the wind stress τ_s varies between SWITCH and the SWITCH_{OW}. Anyway, the difference between the two experiments relative to the CTRL experiment is investigated to judge whether the change in the baroclinic structure is induced by changes of the wind stress field or of the thermohaline surface fluxes. In SWITCH_{OW}, the evolution of the integrated potential energy (Fig. 6.12) resembles that of SWITCH after ten years of integration, but the anomalies have a smaller amplitude. The anomaly of the subpolar gyre is restricted to

a smaller area with no extension to the Labrador and Irminger Seas. A positive anomaly is visible in the Labrador Sea. The thermohaline surface fluxes, especially heat fluxes of the NAO+ composite, produce the strong anomalies of the integrated potential energy here, which in turn enhance the convection and the overturning. So the density distribu-

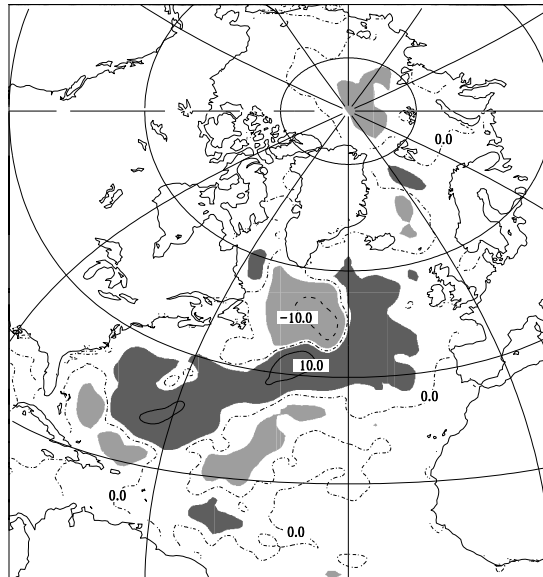


Figure 6.12: Annual mean of the integrated potential energy anomaly for the tenth year of SWITCH_{ow} in Sverdrup; figure caption as in Fig. 6.11

tion in the area of the subpolar gyre is influenced by the wind stress field, but the main impulse comes from the thermohaline surface fluxes.

Convection in the Labrador Sea

The maximum depth of convection in the Labrador Sea for the four experiments is illustrated in Fig. 6.13. The Labrador box encompasses the Labrador Sea between approximately 55°N and 65°N and the coast of New Foundland and 45°W. It is employed to investigate the local effects contributing to the convection in this area. In the first years of SWITCH, the sea ice cover retreats to the north–west corner of the Labrador Sea (Fig. 6.3), which reduces the freshwater flux (melt water) into the central Labrador Sea. The surface salinity is therefore raised compared to CTRL and as a consequence, convection is stronger, and the convection site shifts to the north–west, following the sea ice edge. A static stability analysis reveals that the density changes in the surface layers in the Labrador box are governed by changes in the salinity; temperature changes are of minor importance. Even with changed wind stress and reduced Ekman suction in the northern Labrador Sea, deep convection continues for four years. The doming of the isopycnals is strong and the north–west extension of the subpolar gyre is stronger than in CTRL

Results

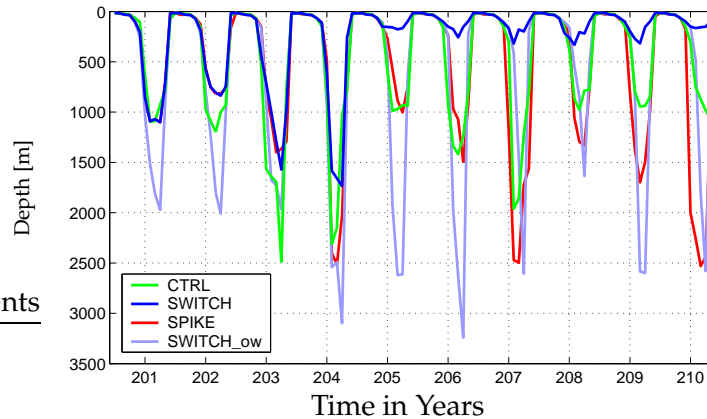


Figure 6.13: Maximal convection depth in the Labrador box (in metres)

(Fig. 6.9, fourth year). The fresh and cold water of the East Greenland Current shows no transport variability during the ten years of the experiment, neither does the outflow of the Labrador Current. After four years, the convection in the Labrador Sea diminishes in the SWITCH experiment. At this time, the reduced surface freshwater flux is no longer enough to maintain the convection with the wind stresses of the NAO– composite. The isopycnals flatten and the stratification becomes stable, with a lens of cold and fresh water at the surface. In this situation, the density differences between the surface and the subsurface layers are dominated by the temperature differences. This is directly connected to the shift of the NAC axis (Fig. 6.10), which now enters the Labrador box from the south, and is no longer restricted by the strong subpolar gyre. The streamfunction anomaly in the northern Labrador Sea weakens at the same time and the anomaly of the circulation becomes restricted to the upper 200 m. The situation after four years is in agreement with earlier findings that, in NAO– years, the convection in the Labrador Sea is weak (DICKSON ET AL., 1996).

The NAO– wind stresses also shift the sea ice margin in the SPIKE experiment to the northern Labrador Sea. The same process as in SWITCH takes place: reduced melting of sea ice in this area, reduced freshwater flux into the ocean and the shift of the convection site. After the switch back to NAO+ forcing, this newly established position of the convection is stable and keeps the area ice free for the subsequent years of the experiment. This also leads to convection depths in the Labrador Sea that exceed those of the CTRL experiment during several years after the return to NAO+ conditions.

Due to the changes in the wind stress field in SWITCH_{OW}, the sea ice margin is shifted to the north exposing the ocean to the colder atmosphere of the NAO+ conditions (Fig. 4.4). The reduction of the sea ice cover is not as strong as in SWITCH, thus the air temperature plays an additional role in determining the sea ice margin. The combination of shifted sea ice margin and colder air temperature leads to an intense heat loss at the surface and subsequent strong enhancement of the convection (Fig. 6.13, light grey line). Convection deepens immediately (year 201) and reaches deeper than 2000 m in al-

most all subsequent years. In this experiment, the density change due to temperature changes is larger than that caused by salinity changes. Stratification is weak during the ten years of calculation.

It should be noted that the internal variability (without change in the forcing) in the Labrador Sea convection is very large. Only the weakening in SWITCH and the strengthening in SWITCH_{OW} compared to CTRL seem to be significant. Even if convection in the Labrador Sea is strong in the SWITCH_{OW} experiment, the meridional overturning weakens after five years. There is no straightforward connection between the Labrador Sea convection and the strength of the meridional overturning.

Heat transport

The changes in the horizontal and the overturning circulation affect meridional heat transport. It is convenient to use the decomposition of total heat advection into the overturning and gyre components as derived by BRYAN (1962), which has already been introduced in Section 5.3. In Fig. 6.14 the time evolution of the total meridional heat transport and the decomposition at 48°N is illustrated. In the CTRL experiment, the total meridional heat transport is 0.85 PW at this latitude. In all three experiments, there

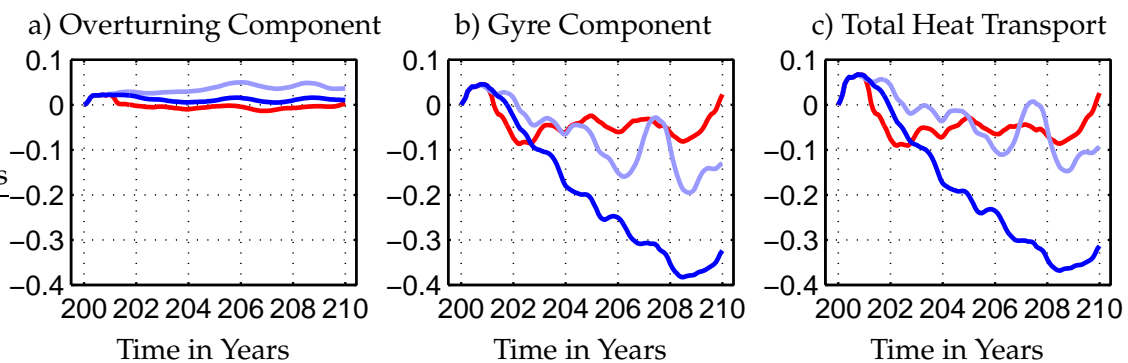


Figure 6.14: Deviation of meridional heat transport at 48°N from CTRL (in PW); the blue line is the SWITCH experiment, the red line the SPIKE experiment and the light blue line is the SWITCH_{ow} experiment; the time series are filtered with a thirteen months running mean

is a slight instantaneous increase of the overturning component (Fig. 6.14a, blue line) after the switch to NAO– forcing. This matches the results from the evolution of the meridional overturning circulation at 48°N (Fig. 6.6). The enhanced heat transport at the Subpolar Front is mainly the result of the diminished southward Ekman transport. The gyre component reflects the spin down of the subtropical and subpolar gyres accompanied by a reduction of heat transport to the north Fig. 6.14b. This is most pronounced in SWITCH. As seen above, the SPIKE experiment exhibits long term changes that can not be explained by the external forcing alone but must involve interior ocean dynamics. The total heat transport (Fig. 6.14c) is the sum of both components, and it is dominated by the

gyre component. The gyre component contains interannual variability that again hints at internal variability in the ocean circulation, independent of the imposed forcing.

6.3 Discussion

The shift from NAO+ to NAO– forcing has a basinwide impact on ocean and sea ice in our numerical model. This result agrees with observations (WALSH AND JOHNSON, 1979; FANG AND WALLACE, 1994; DESER ET AL., 2000; LAZIER ET AL., 2002; CURRY ET AL., 1998). KAUKER ET AL. (2003) found the dipole in sea ice cover (positive anomaly in the Barents and Nordic Seas and negative anomaly in the Labrador Sea) as a reaction of the shift from NAO+ to NAO– forcing by using statistical methods. In the experiments presented here, an isolated switch is conducted and a direct, physical connection between the dipole pattern and the NAO index is found. The sea ice cover reacts immediately to the new forcing, but the patterns amplify further over the subsequent years. Thus, we can support the hypothesis of KAUKER ET AL. (2003), that the NAO causes a shift in the observed sea ice cover.

MAURITZEN AND HÄKKINEN (1997) investigated the influence of sea ice export on the thermohaline circulation. They found that an increase of 2-3 Sv of the meridional overturning at 25°N corresponds to a decrease of sea ice export through the Fram Strait of 800 km³/yr. The ice export anomaly through the Fram Strait and Barents Sea in the sensitivity experiments described here is smaller than discussed by MAURITZEN AND HÄKKINEN (1997) and the sea ice melts in the Greenland-Iceland-Norwegian Sea, before passing through the Denmark Strait (Tab. 6.1). In the simulations presented here, the East Greenland Current, which is the link between Fram Strait freshwater export and the Labrador Sea, does not influence the convection. In the sensitivity experiments, the freshwater transport of the East Greenland Current into the Labrador Sea showed no discernible differences between the experiments. Thus, the ice induced freshwater anomaly is confined to the region north of the Greenland-Iceland ridge and a possible response of the meridional overturning streamfunction could not be isolated.

The meridional heat transport decomposition of BRYAN (1962) is also used by EDEN AND WILLEBRAND (2001), who performed idealised studies concerning the oceanic response to the NAO. The heat transport in their “NAO–both” study ^{II} is qualitatively similar to SWITCH, but the amplitude of the signal differs substantially. In our SWITCH experiment, the total heat flux is reduced by 0.3 PW, whereas the comparable value of the results of EDEN AND WILLEBRAND (2001) is ± 0.08 PW. We attribute this to the strong decrease of both the subtropical and subpolar gyres in SWITCH by ± 20 Sv compared to a 7-8 Sv anomaly in the experiments of EDEN AND WILLEBRAND (2001). The difference could be caused by the closed northern boundary in the model of EDEN AND WILLEBRAND (2001), which restricts the variability from the Nordic Seas. Additionally, the wind stress forcing fields are likely to be different, because EDEN AND WILLEBRAND

^{II}wind stress fields and surface heat flux associated with high NAO phases were used

(2001) used a regression analysis to deduce them, compared to the composites which are utilised here. Hydrographic data were analysed by BERSCH (2002) and a decrease of northward heat transport at 47°N in the upper layer in 1997 was found.

The delayed baroclinic reaction of the meridional overturning streamfunction following the switch to NAO– conditions also differs as the 3-yr lagged response of EDEN AND WILLEBRAND (2001) resembles the initial anomaly but with reverse signs. The centre of the anomalous cells is at approximately 1000 m depth and there is no sign reversal in the water column. This difference might also be caused by the smaller internal variability.

The dipole pattern of the vertically integrated potential energy looks similar to the observed distribution of CURRY AND MCCARTNEY (2001). The authors define a baroclinic mass transport index from the difference of the potential energy anomaly (0-200 db) in the subtropical and subpolar gyre derived from measurements. This index correlates well with the NAO index, with the ocean lagging by 1-2 years. The ocean response constitutes an integration of the atmospheric signal through mixed layer memory and Rossby wave propagation (CURRY AND MCCARTNEY, 2001). In our experiment, we have an immediate reaction of the integrated potential energy anomaly, so we can not confirm the lagged response, but the spatial distribution of the anomaly. However, our experiments use an idealised scenario. We expect that in a hindcast study, it is more straightforward to detect a lagged response. On the other hand, other interactions, which are not taken into account here, could dampen or modify the response to the NAO.

According to the results of CURRY AND MCCARTNEY (2001), the anomalous freshwater fluxes and the lateral advection of cold and fresh water from the East Greenland Current into the Labrador Sea current are too small to influence the deep convection, except in times of the passage of a low salinity anomaly like the GSA, which could inhibit convective overturning. The model results of HAAK ET AL. (2003) reveal only a minor impact of a single GSA event on the strength of the thermohaline circulation. This is in contradiction with the results of HÄKKINEN (1999a), who showed that an idealised GSA could produce surface salinity changes in the subpolar North Atlantic and in the thermohaline circulation which need several years to readjust. Our experiments do not produce a freshwater anomaly which is comparable to the GSA and the East Greenland Current shows no variability due to the shift from NAO+ to NAO– forcing.

6.4 Conclusions

Three sensitivity studies of the reaction to NAO+ and NAO– conditions are performed with the help of a coupled ocean-sea ice model. Switching from NAO+ to NAO– conditions produced an instantaneous reaction in the sea ice cover and thickness. In the sea ice extent, a dipole between the GIN Sea/Barents Sea and the Labrador Sea evolves. In the central Arctic Ocean, the sea ice which is formed in the Beaufort Sea is advected to the Eurasian shelf and into the central Arctic Ocean. This causes a convergent pattern of anomalous thick ice in the East Siberian Sea and the central Arctic Ocean. The ice export

Conclusions

through the Fram and Davis Straits is reduced with NAO– forcing, whereas more ice is advected southwards through the Barents Sea Opening. In SWITCH, the response patterns are instantaneously induced, but their amplitudes increase over time. The total sea ice volume needs ten years to converge to $34 \times 10^3 \text{ km}^3$.

The meridional streamfunction shows an instantaneous reaction to the changed meridional Ekman volume transport, which is expressed in an enhanced meridional overturning and corresponding northward heat transport at 48°N . In the subsequent years, adjustment by wave processes and advection of density anomalies reduces the overturning by 8 Sv in SWITCH, additionally the northward heat transport at 48°N is decreased. The subtropical and subpolar gyres are reduced in strength and the deep convection in the Labrador Sea stops after a transition period of four years.

When only the wind stress field is switched to NAO– forcing and the thermohaline forcing is associated with NAO+ conditions (SWITCH_{OW} experiment), the baroclinic reaction of the ocean is different. In the subpolar gyre, the barotropic compensation of the changed northward Ekman transport is still present, which leads to the conclusion that the NAO– thermohaline surface forcing is necessary for the baroclinic reaction. In this experiment, the convection in the Labrador Sea is present throughout the ten years of the experiment, in fact the convection goes usually deeper than in CTRL. Thus, there is no straightforward connection to the overturning at 48°N in this experiment, which exhibits very small differences between the overturning of SWITCH_{OW} and CTRL. A further experiment is presented in the next chapter, where a close relationship between the meridional overturning streamfunction and the convection in the Labrador Sea is revealed.

The influence of the switch of the NAO is felt in sea ice volume and extent. Furthermore, convection in the Labrador Sea is affected, as are the meridional overturning streamfunction and the meridional heat transport. Perhaps the most surprising result is the switch to a different state of equilibrium in SPIKE by switching for only one year to NAO– forcing. Substantial but transient changes in the forcing over the Labrador Sea lead to long lasting anomalies of the convection and as a consequence the sea ice margin. The memory effect of the Labrador Sea is clearly visible in these experiments. These results call for future investigations that compare the results with those of a hindcast experiment. An investigation of the impact of the changes in meridional heat transport on the atmosphere is also of interest.

7 Internal variability

When the model is integrated for centuries with the OMIP year (see section 4.1) as atmospheric forcing, the maximum of the meridional overturning streamfunction oscillates on time scales of approximately 40 years. Since the OMIP forcing does not contain any other variability than seasonal, this oscillation must stem from processes within the model system. The possibility of a self-sustained internal oscillation of the ocean–sea ice system is highly interesting in view of the ongoing discussion about long-term climate variability. It is still an open question, to what degree the observed climate variability is anthropogenically forced and how much is natural climate variability. A better understanding of the development of internal ocean–sea ice variability and their time scale is essential to the interpretation of fully coupled climate models.

To investigate this variability, the model is initialised from a state of rest and integrated for 980 years. The time series of the maximum of the meridional overturning streamfunction at 48°N and 1500 m depth is shown in Fig. 7.1.

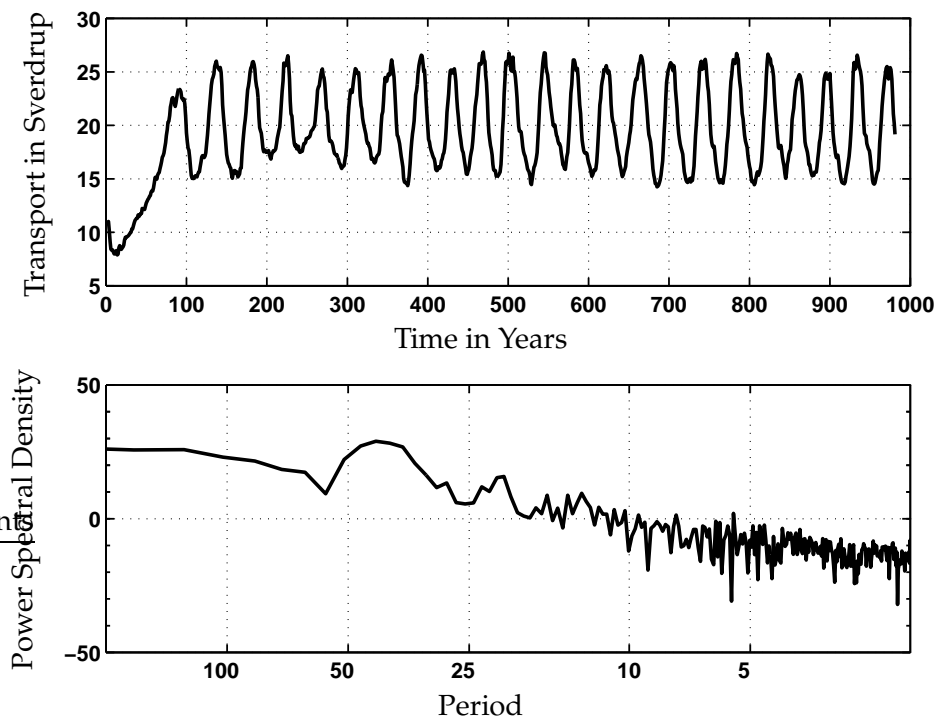


Figure 7.1: Time series of the oscillation; upper panel: meridional overturning at 48°N and 1500 m depth; lower panel: spectrum of the time series

First look at the oscillation

After a spin up of 90 years, the overturning starts to oscillate between values of 15 and 26 Sv. The Fourier spectrum has a peak at the period of 42 years, but the bandwidth of this peak is quite broad. The periods of the variability range between 30 and 50 years. To understand the mechanisms of the oscillation, various fields are investigated. The first 135 years are neglected in the analysis, because they fall into the spin up phase.

Firstly, phase relationships between various fields are described with the help of lagged regressions: the time series of the overturning is regressed onto sea surface salinity and the vertically integrated streamfunction. The focus will be on the processes which lead and follow the maximum of the overturning. Distinct years are then consulted to examine the processes in the Labrador Sea. Finally, the discussion summarises the mechanisms that lead to the oscillation.

7.1 First look at the oscillation

Minimum of the overturning

Lag 0 is defined as the time when the overturning streamfunction is at its maximum value. Approximately 20 years before this maximum is reached, the overturning is at its lowest value. At this time, circulation in the subtropical and subpolar gyres is weaker than the mean values (Fig. 7.2(a)) and the transport is enhanced in the region downstream of the Gulf Stream separation, near 45°N. This region will be referred to as NAC Pathway in the following.

Due to the reduction of the subpolar and the subtropical gyres, the total advective heat transport at 48°N is about 0.5 PW (Fig. 7.3). The main contributor to the heat transport at this latitude is the gyre component. It is about 0.4 PW in the minimum of the oscillation. The minimum heat transport of the gyre component occurs a few years before the minimum of the overturning (Fig. 7.3). The heat transport due of the overturning component is less than 0.1 PW on the average. Associated with the minimum of the overturning are positive salinity anomalies west of North Africa, in the Caribbean (Fig 7.4(a)) and especially in the NAC Pathway region. The surface salinity is reduced over a large area if the subpolar gyre. The sea surface temperature (SST) also has an anomalous dipole pattern (not shown), with warm water in the NAC Pathway region and colder than normal water in the Labrador Sea. The associated patterns of the surface density (not shown) can be described in analogy to the salinity patterns: the density is low in the subpolar gyre, where the surface water is anomalously fresh and the density is anomalously high in the NAC Pathway region.

The oscillation is not restricted to the surface fields, but has a deep reaching signal. This is illustrated in Fig. 7.5 for the vertical salinity and temperature distributions of the upper 600 m of the Labrador box. The Labrador box, as introduced in section 6.2.2, encompasses the Labrador Sea from approximately 55°N to 65°N and from the coast of Newfoundland to 45°W. In the upper 200 m, the water is fresh and cold, when the overturning is at its

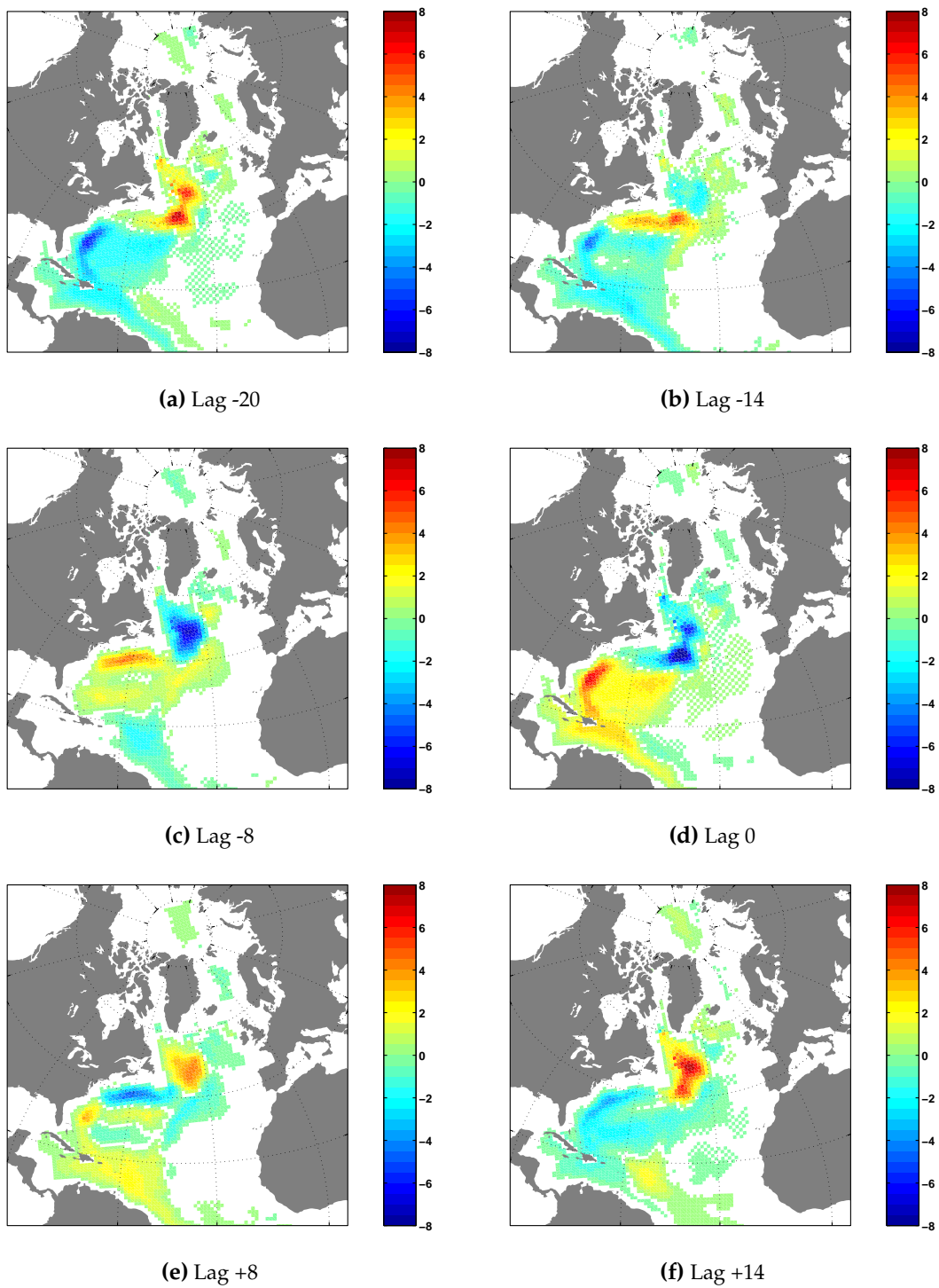


Figure 7.2: Associated patterns of the streamfunction for the vertically integrated transport regressed upon the overturning index defined as the value of the overturning streamfunction at 48N and 1500m depth. Amplitudes smaller than $0.2 S_0$ are omitted. Lags are given in years relative to the maximum of the overturning where negative lags mean that the streamfunction anomalies lag behind the overturning

First look at the oscillation

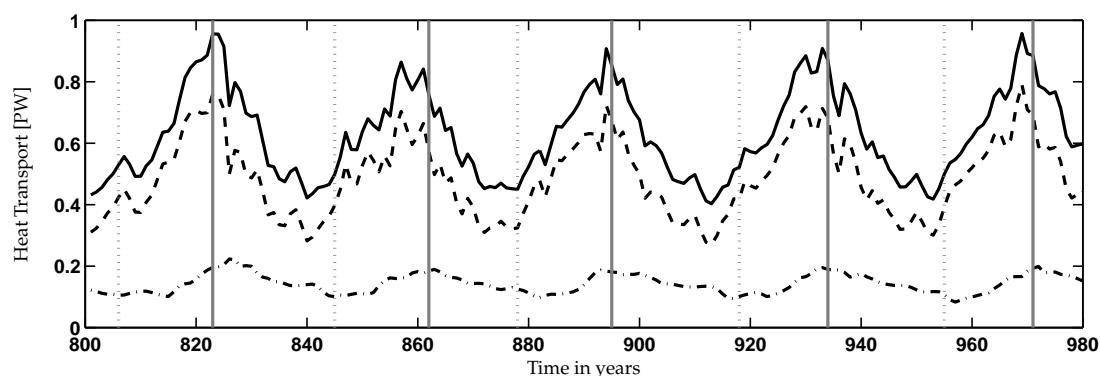


Figure 7.3: *Fluctuations of the meridional heat transport at 48°N (solid black line) and its decomposition in gyre (dashed line) and overturning component (dashed–dotted line); the maxima of the overturning are marked with vertical grey lines, the minima with vertical dotted grey lines*

minimum. Water lighter than $\sigma = 27$ appears at the surface in the Hovmöller diagram of the horizontally averaged densities in the Labrador Sea box (Fig. 7.5). At this time, there is no deep convection in the Labrador Sea, as can be seen from the time series of maximum convection depths in Fig. 7.6. From this figure can be deduced that the oscillation of the meridional overturning and the convection in the Labrador Sea are closely related. The convection sites south of Iceland and in the Greenland Sea (compare Fig. 5.4) are analysed in the same way (not shown), but they do not appear to be connected to this oscillation.

Increasing overturning

The Gulf stream assumes its northernmost position and reaches its peak 14 years before the maximum of the overturning. The positive salinity and streamfunction anomalies reflect that the Gulf Stream is at its strongest. In the subtropical North Atlantic, the positive salinity anomaly becomes weaker and the circulation of the subtropical gyre increases. At the same time, a positive salinity anomaly appears in the Labrador Sea accompanied by an increase of the cyclonic circulation strength in the subpolar gyre. This intensification of the subpolar gyre is also visible in the rising of the isopycnals in the Labrador Sea (Fig. 7.5). In year 810 or 920 for example, the 5°C isotherm and the 35.2 isohaline move up from 250 m to 200 m. Simultaneously, convection in the Labrador Sea sets in (Fig. 7.6). With increasing overturning, the salinity anomaly in the Labrador Sea gets stronger (Fig. 7.4(c)) and the subpolar gyre is further amplified (Fig. 7.2(c)). These anomalies reach their extreme values about 8 years before the maximum of the overturning. Now, the doming in the subpolar gyre is fully established and the convection is at its maximum. The heat transport increases in this phase of the oscillation, because the gyre component increases. The maximum of the gyre component appears a few years before the maximum of the overturning. In contrast to this, the overturning component of the heat transport reaches its maximum shortly after the maximum of the meridional overturning.

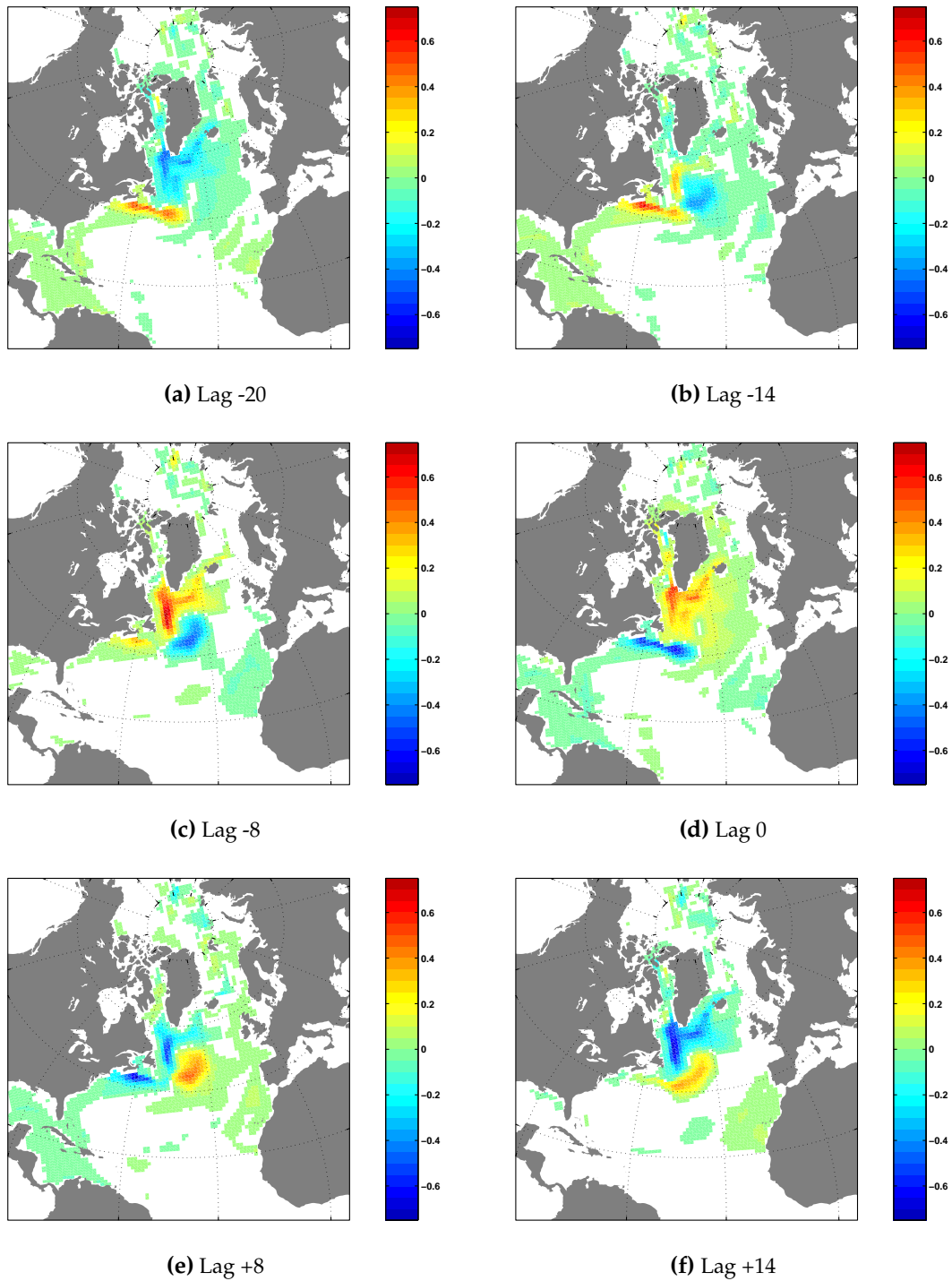


Figure 7.4: Associated patterns of the maximum of the overturning and sea surface salinity (SSS) for specific lags, values smaller than ± 0.01 are omitted

First look at the oscillation

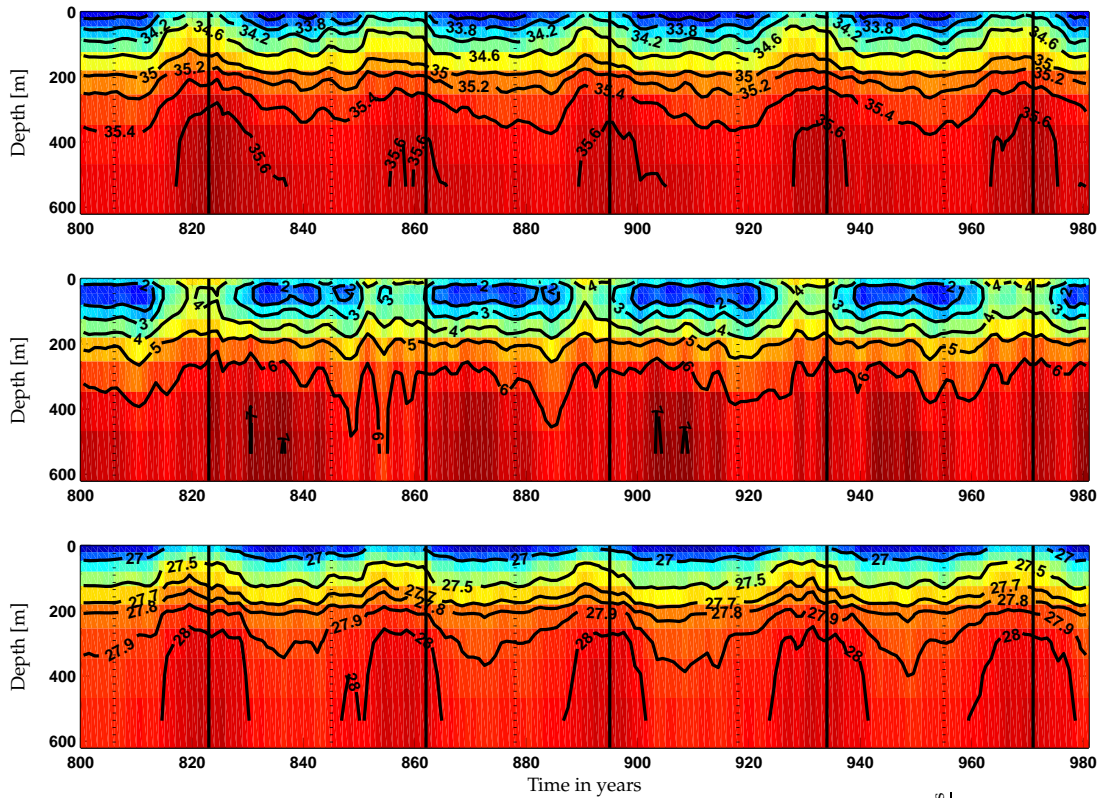


Figure 7.5: Mean layer profiles in the Labrador box as Hoömüller diagrams over time; upper panel: salinity, middle panel: potential temperature, lower panel: potential density in sigma units; the maxima of the overturning are marked with vertical grey lines, the minima with vertical dotted grey lines

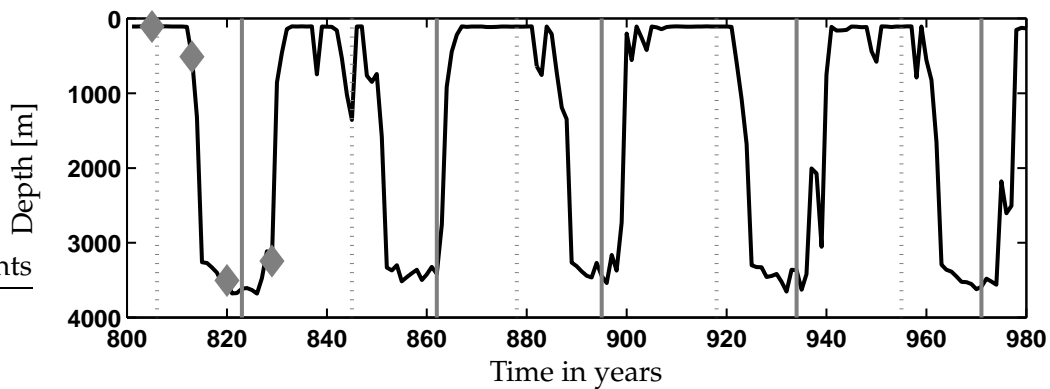


Figure 7.6: Maximal convection depth in the Labrador box in March (in metre); the diamonds mark the distinct times of four different phases of the overturning (years 805, 813, 820 and 829)

Maximum of the overturning

The subtropical gyre is now strongest (Fig. 7.2(d)) with an enhancement of about 8 Sverdrup above the mean transport. There is a negative salinity anomaly visible in the Caribbean and along the coast of North America (Fig. 7.4(d)). The negative streamfunction anomaly off the coast of Newfoundland describes a weaker Gulf Stream that is displaced southwards. This displacement is linked to a negative salinity anomaly.

The circulation in the subpolar gyre is reduced in magnitude, but there is still a strong cyclonic circulation anomaly off the Grand Banks. The positive salinity anomaly in the subpolar gyre is weaker than in the years before. The mean profile in the Labrador box still shows shallow depths of the $\sigma = 27.7$ isopycnal. Overturning maxima appear at the end of the periods with warm, saline surface waters in the Labrador Sea. The meridional heat transport responds to the weakened subpolar gyre with a decrease, and the overturning component is at its maximum.

Decreasing overturning

The subtropical and the subpolar gyres have slowed down 8 years after the maximum of the overturning streamfunction. The Gulf Stream is still weak, associated with a negative streamfunction anomaly off the coast of Newfoundland (Fig. 7.2(e)). The salinity anomaly decreases also. The surface salinity anomaly in the Labrador Sea has changed sign and the surface water is now fresher than in the years before. The density is low at the surface as in the state of minimum overturning and deep convection is altogether suppressed. 14 years after the maximum, the NAC pathway is in a position between its extremes. Now, the decrease of the subpolar gyre is strongest, whereas the circulation in the subtropical gyre decreases further. The northward heat transport is at its lowest value.

Rossby waves

The associated patterns between the overturning time series and the salinity at 300 m depth (Fig. 7.7) reveal that in the subtropical North Atlantic, anomalies are propagated by Rossby waves. The Rossby waves are visible in the typical crest-shape of the phase lines that reflect the fast westward propagation at low latitudes (Fig. 7.7) and the rapid drop in propagation speed rapidly decreases with geographical latitude. The Rossby waves propagate salinity anomalies from the coast of North Africa to the Caribbean by displacing the depth of the isopycnals. The waves are absorbed in the western boundary current. The Gulf Stream and the NAC advect the salinity anomalies to the north, where they affect the density distribution in the Labrador Sea. The salinity anomalies could be traced further to the north in the Norwegian Atlantic Current, but these changes could not be linked to the oscillation of the overturning. The East Greenland Current which could possibly propagate these changes of the Nordic Seas to the south, is also free of any accountable oscillation. Thus, the Labrador Sea is the missing link between the changes in the horizontal circulation and the meridional overturning.

At lag -20, a positive salinity anomaly at the coast of North Africa is visible, which

First look at the oscillation

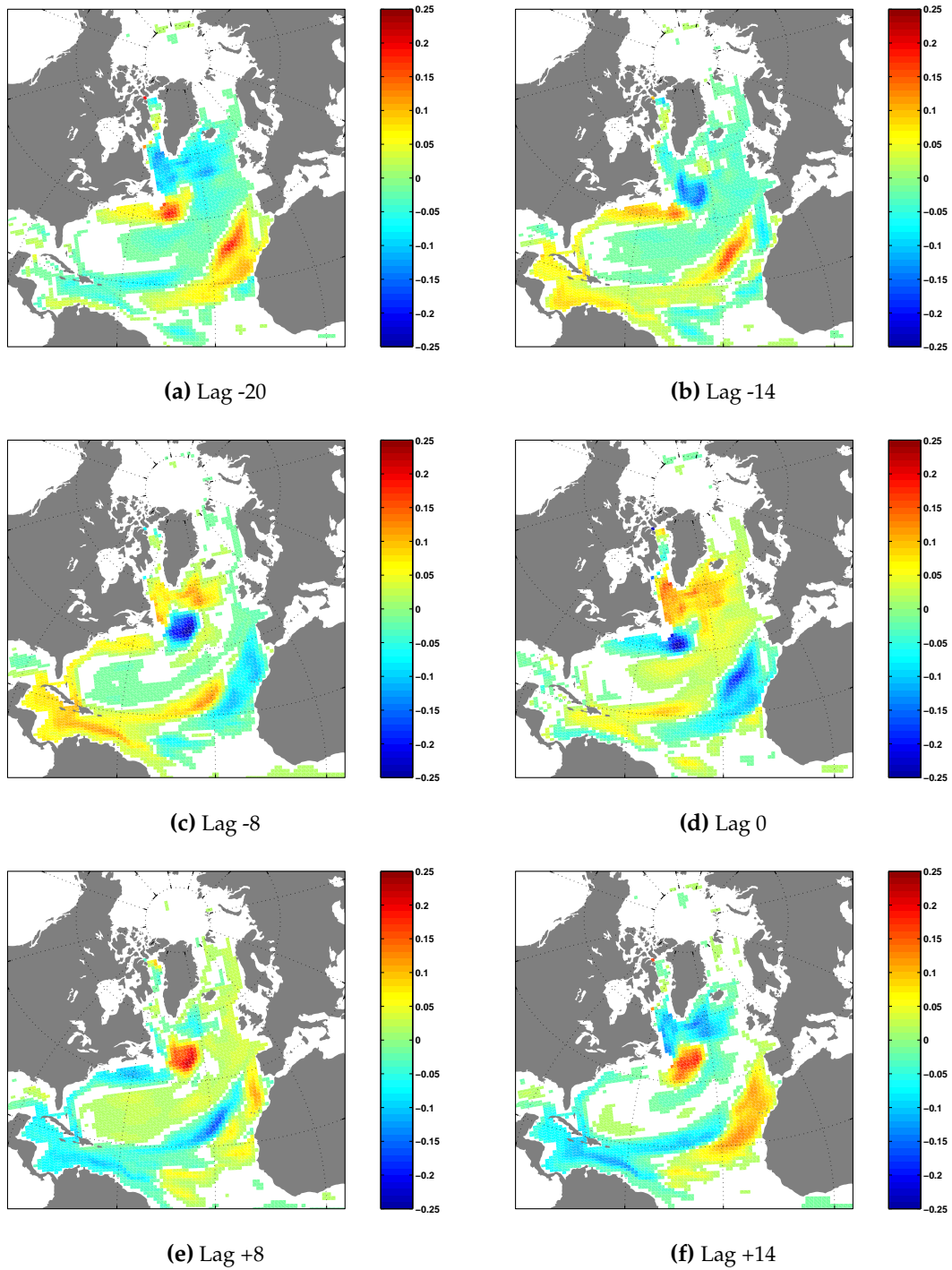


Figure 7.7: Associated patterns of the maximum of the overturning and salinity at 300 m depths for specific lags, values smaller than ± 0.01 are omitted

spreads at lag -14 and lag -8 into the Carribean. At this time, a negative anomaly evolves at the coast of North Africa.

7.2 Role of the Labrador Sea

In the preceding section several regions are identified where the effects of the oscillation are most pronounced. The largest amplitudes of salinity anomalies at the surface are located in the region of the NAC pathway and of the subpolar gyre. In the subtropics and at the North African coast, the amplitudes are small. In the Nordic Seas and Arctic Ocean, they are negligible. The streamfunction anomalies are restricted to the western North Atlantic.

Of all convection sites, only the Labrador Sea convection appears to be connected to the overturning time series. Thus, the Labrador Sea and the NAC pathway region are identified as the key regions of the oscillation.

The connection between the Labrador Sea convection and the overturning time series is analysed with the help of a cross-spectral analysis. This method retrieves the phase relationship and the coherency between the two time series. Fig. 7.8 displays the variance and the squared coherency of a cross-spectral analysis between the time series of the maximum depth of the convection in the Labrador Sea (Fig. 7.6) and the maximum of the overturning (Fig. 7.1) for the 980 years integrated. The maxima of the variance for the two time series are both at a period of about 40 years. At a period of 40 years, the squared coherence is significant, with values of almost 1.0. The phase spectrum reveals that the convection time series leads the overturning time series by 45° , which is equivalent to a lag of five years: When convection sets in, maximum overturning is reached five years later. In the Labrador Sea, deep convection contributes the main fraction of the production of the deep western boundary current, which is, in the model, the lower branch of the meridional overturning, located between 1200 and 3000 m depth.

The next question is what controls the oscillation. The atmospheric wind stress forcing is climatological and is therefore ruled out as the driving factor. Another possibility would be surface or lateral fluxes of heat and freshwater into the Labrador Sea, which are investigated in the following.

The stability of a water column is determined by the vertical density gradient, which is defined according to GILL (1982) as

$$E = \frac{d\rho}{dz} = \left[\left(\frac{\partial\rho}{\partial T} \right)_S \frac{dT}{dz} + \left(\frac{\partial\rho}{\partial S} \right)_T \frac{dS}{dz} \right] \quad (7.1)$$

Therein, $-\rho^{-1}(\partial\rho/\partial T)_S = \alpha$ and $\rho^{-1}(\partial\rho/\partial T)_T = \beta$ are the thermal and haline expansion coefficients. The temperature in equation (7.1) is the potential temperature, which includes the adiabatic lapse rate, and the density is the potential density. The stratification is stable when the density in the upper layer is lighter than the density below. Equation (7.1) is linearised by assuming that the expansion coefficients do not change with

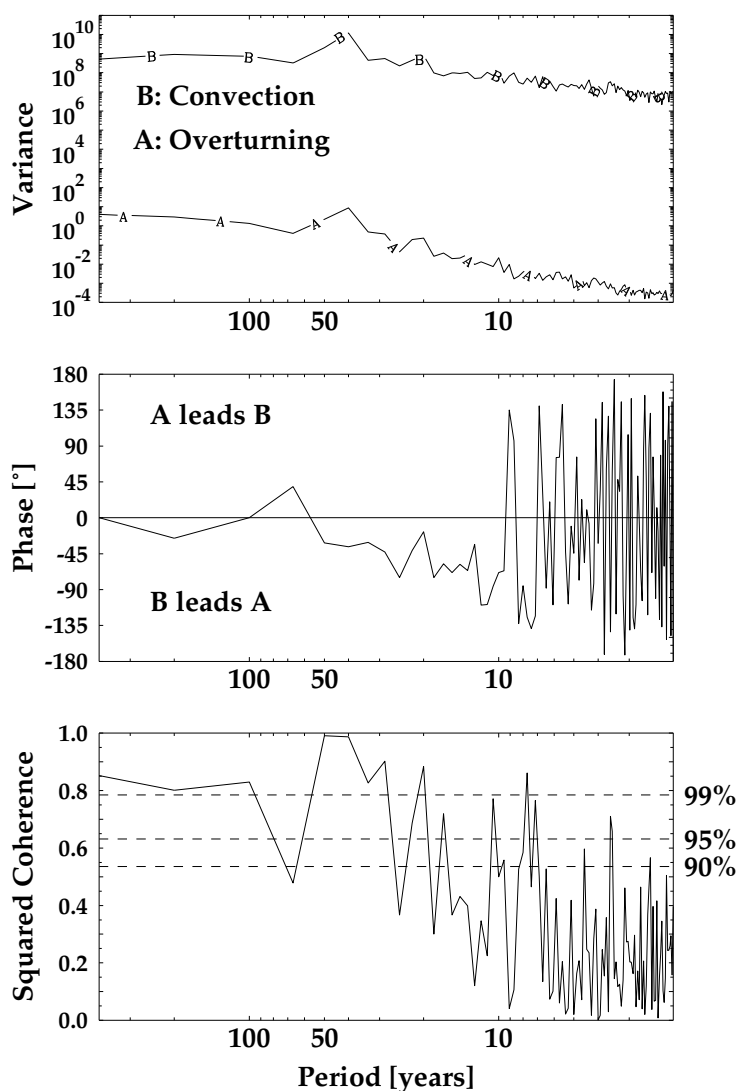


Figure 7.8: The cross-spectra of the maximum of the overturning streamfunction (A) and the maximum of the convection in March in the Labrador box (B). Top panel: spectral variance; middle panel: phase spectrum, lower panel: squared coherency; the significance of the squared coherency is estimated by a Bartlett procedure with a chunk length of 200 years

temperature, salinity or density. Now, the temperature and salinity effects on the density can be discussed separately.

To estimate the vertical density gradient in the Labrador box, the mean temperature and salinity are calculated for the upper 300 m and the layer 300-600 m of the Labrador box. The main density variations are confined to the upper 300 m, so that restricting the analysis to the upper ocean seems reasonable. The temporal derivatives of temperature and salinity in the upper (and lower) box are calculated. Then, the differences between the temporal derivatives of the density in the upper ($d\rho_1$) and the lower ($d\rho_2$) layers is

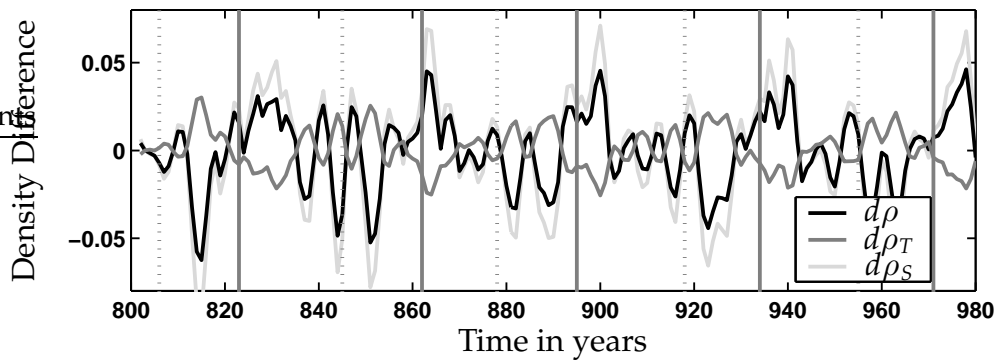


Figure 7.9: Temporal derivatives of density difference between the upper 300 m and the adjacent 300 m, based on yearly mean values; separated into the salinity ρ_S and temperature ρ_T parts of the density difference

estimated and illustrated in Fig. 7.9. The temporal derivatives emphasise the times when stability is changing most.

In year 813 (Fig. 7.9), when the convection sets in (Fig. 7.6), the density changes are strong from one year to the next and have a negative sign. This indicates a destabilisation of the water column. Also, the density changes are governed by changes in salinity, whereas the effect of the temperature changes tend to stabilise the water column. During deep convection (years 816 to 827), the density differences fluctuate around zero and become positive at the end of the convection phase. The water column is again stably stratified. This analysis shows, that convection in the Labrador Sea is governed by the salinity changes in the Labrador box, which destabilise the water column. And with a lag of five years, the overturning reacts to these changes in the Labrador Sea.

The analysis is extended to quantify the influence of the surface freshwater flux. The annual mean values of the surface freshwater flux are always positive, indicating a continuous supply of freshwater to the Labrador box. The freshwater flux is in phase with the overturning, being high, when the overturning is maximum and reduced, when the overturning is weak. This flux is converted into a volumetric change of salinity and subtracted from the above mentioned derivation of the salinity in the upper layer over time ($d\rho_S$). As a result, the progress of the destabilisation is not changed due to this surface flux, rather it supports the stabilisation of the water column. Thus, the surface freshwater flux is not a driving component.

For the understanding of the lateral salt fluxes into the Labrador box, four distinct years are chosen, because the lateral fluxes has been shown to control the convection in the Labrador Sea and thus the overturning circulation. The horizontal salt transports are illustrated in Fig. 7.11, and the absolute values of the streamfunction and convection depth are depicted in Fig. 7.10.

In the minimum of the overturning (year 805), the subpolar gyre is the weakest, with only a small band of cyclonic circulation south of Greenland (Fig. 7.10(a)). The salt trans-

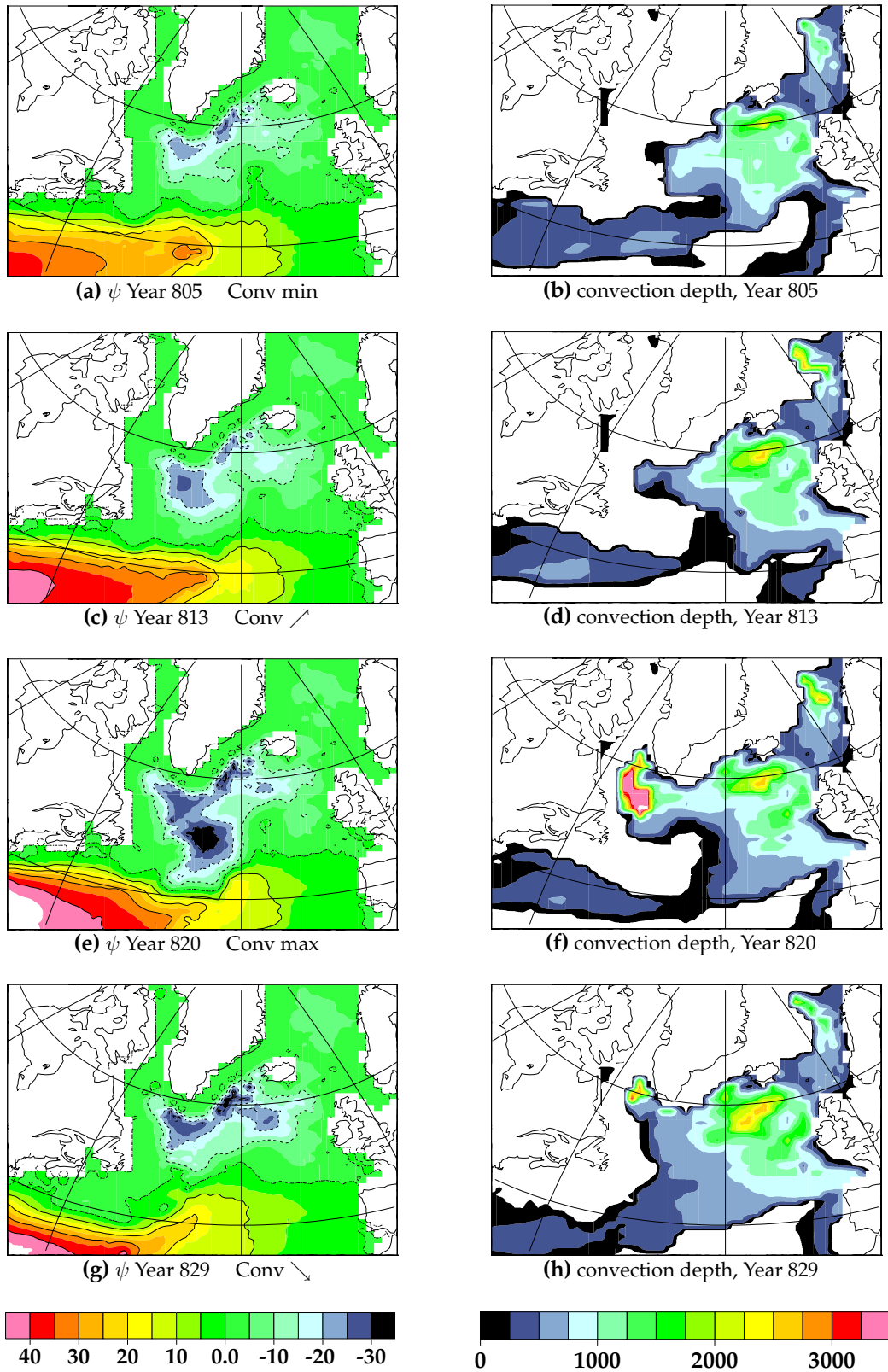


Figure 7.10: Annual means of the streamfunction (in Sv) and convection depths (in metres) in the northern North Atlantic for distinct years, only convection depths larger than 100 m are shown

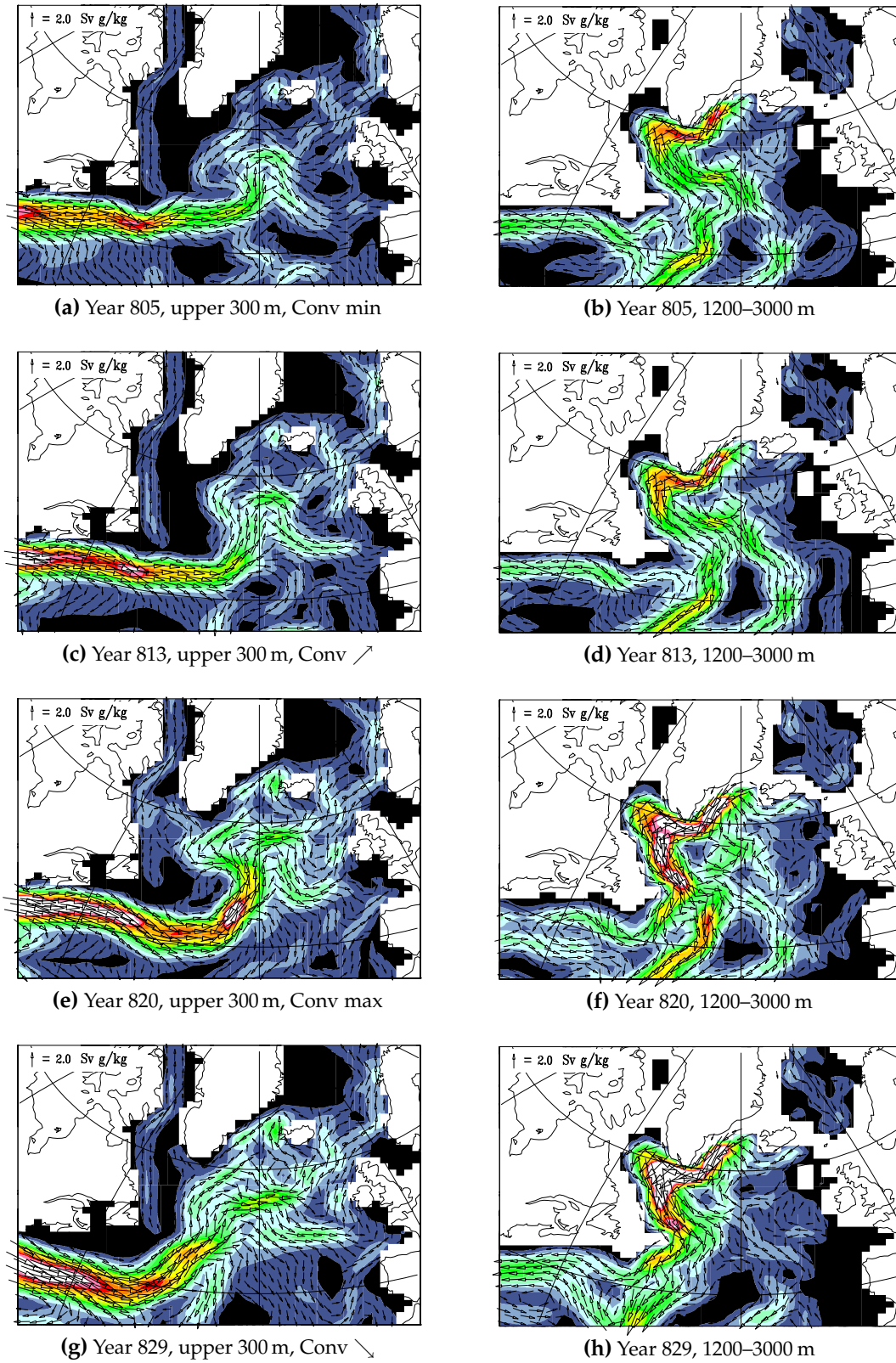


Figure 7.11: Annual means of salt transport relative to 34.46 in the northern North Atlantic for the upper 300 m and for the depth of the DWBC (1200–3000 m)

port of the Gulf Stream is close to the coast and weak (Fig. 7.11(a)). The salt transport of the NAC takes an almost straight path to the north-east. There is no inflow of salty water into the Labrador Sea. This corresponds to the situation at lag -20 of the regression analysis, where the surface salinity shows a negative anomaly in the Labrador Sea (Fig. 7.4(a)). What appears to be the northward salt transport at the coast of Newfoundland (Fig. 7.11(a)) is actually southward transport of freshwater in the Labrador Current. The deep western boundary current (DWBC) is weak while crossing the Labrador Sea and flows to the south in a broad band (Fig. 7.11(b)). The term “western boundary current” is not quite appropriate for a current close the Mid-Atlantic ridge, but it is used here, because the location of the current is variable and the name is consistent with the literature (SPALL, 1996b).

Eight years later, in year 813, the Gulf Stream salt transport is increased (Fig. 7.11(c)). The NAC transports salt in the vicinity of the Labrador Sea, which enhances the cyclonic circulation in the Labrador Sea and mid-depth convection is setting in (Fig. 7.10(d)). This is comparable to lag -14 of the regression analysis, where a positive salinity is developing in the Labrador Sea (Fig. 7.4(b)). The salt transport of the DWBC is also increased in the Labrador Sea.

In year 820, deep convection is established in the Labrador Sea, with convection depths over 3500 m in a large area (Fig. 7.10(f)). Now, the salt transport of the Gulf Stream is very strong and the inflow of saline water with the NAC over the eastern boundary of the Labrador Sea is prominent (Fig. 7.11(e)). On its way into the Labrador Sea the NAC loses heat (not shown) and the saline water carried with it becomes denser. The inflow of dense water increases the density in the Labrador Sea. The subpolar gyre is still strong, accompanied by shallowing of the isopycnals in the central Labrador Sea (Fig. 7.5). Underneath, the salt transport of the DWBC is strongly enhanced, with a branch close to the coast. This enhancement raises the isopycnals near the coast and squeezes the upper water column. There the Gulf Stream loses potential vorticity and regains it by moving southward. The increased DWBC at the coast and the enhanced NAC lead to the increased cyclonic circulation at 40°W and 45°N (Fig. 7.10(e)).

The relocation of the Gulf Stream has consequences for the following years. The import of saline water from the east into the Labrador Sea vanishes and the convection diminishes. Only a small patch of deep convection remains in the northern Labrador Sea in the year 829 (Fig. 7.10(h)). The salt transport of the Gulf Stream is still displaced southward of 40°N, and its strength is weakened (Fig. 7.11(g)). Now, saline water flows into the Labrador Sea from the south-east with the NAC, but this water does not reach the convection sites and is not dense enough to maintain the convection as the eastern inflow did. The subpolar gyre is weak and the Labrador Sea is, at the surface, filled with fresh and cold water from the surface and of Arctic origin, supplied via the Davis Strait and the East Greenland Current (Fig. 7.5). The cyclonic streamfunction anomaly at 40°W, 45°N has vanished and the streamfunction is positive in this area, because the NAC is flowing gradually moving to the north.

7.3 Discussion

Oscillations of the meridional overturning streamfunction were detected in numerous modelling studies. Several experiments with idealised ocean-only models reveal such a variability on decadal time scales due to various changes of the atmospheric surface forcing. An overview has been given in Section 2.2.4. Very interesting results in regard to the presented oscillation are found by DELWORTH ET AL. (1993) and GREATBATCH AND ZHANG (1995). DELWORTH ET AL. (1993) detected in the GFDL coupled ocean-atmosphere model a variability of the thermohaline circulation with a time scale of 40–60 years. A similar oscillation was found by GREATBATCH AND ZHANG (1995) in an ocean model of an idealised North Atlantic with a period of 50 years. As summarised by STOCKER (1996), the main factor of these oscillation is a pool of cold and fresh water in the western Atlantic Ocean. STOCKER (1996) estimated the time it would take to renew this cold and freshwater pool by a flux anomaly of 1 Sv to about 26 years. The period of the oscillation of WEAVER AND SARACHIK (1991b) was about ten years and the authors proposed a purely advective mechanism. A periodic strengthening and weakening of the convection which was caused by subsurface advective warming and surface freshening in the subpolar region was the explanation of YIN AND SARACHIK (1995) for their oscillation. The authors called it an advective–convective mechanism.

OTTERÅ ET AL. (2003) found a long term variability of the meridional overturning in the North Atlantic in their coupled ocean-atmosphere-sea ice model which is linked to temperature and salinity anomalies in the western tropical Atlantic. In our experiments, the temperature and salinity anomalies in the Caribbean play only a minor role and they are not governing the oscillation. However, this region could be important for air–sea interaction and the connection to the Pacific Ocean as stated by LATIF ET AL. (2000).

Variability on multidecadal time scale was extracted from observations of SST and sea level pressure by DESER AND BLACKMON (1993): the authors distinguished between a cold period in the North Atlantic from about 1900 to 1930 and a warm period from about 1940 to 1970. KUSHNIR (1994) also analysed SST data of the North Atlantic and found negative SST anomalies before 1920 and during the 1970s and 1980s. Positive SST anomalies dominated from 1930 to 1960. In another study, SCHLESINGER AND RAMANKUTTY (1994) could isolate a period of 65–70 years from the nearly 140 year-long IPCC estimated global temperature record. Further analysis of MANN AND PARK (1996) and TOURRE ET AL. (1999) located a spectral peak between 50 and 60 years, which could be seen as the confirmation of a multidecadal variability as the used data set is just about long enough to allow this conclusion. A recent work of DELWORTH AND MANN (2000) compared data from instrumental records and coupled model studies and concluded that the observed patterns of SST variability in the North Atlantic and the model results are in a good agreement.

JOYCE ET AL. (2000) analysed the variability of subtropical mode water (STMW) and found a decadal variability of about 12 to 14 years period. An enhanced production of STMW is associated with a high NAO and a northerly position of the Gulf Stream.

This is followed by an enhanced export of Labrador Sea Water (LSW) with the DWBC, which affects the position of the Gulf Stream at their crossover point. Direct velocity measurements of [LAVENDER ET AL. \(2000\)](#) further interpreted by [RHEIN \(2000\)](#) revealed that warm and salty water enters the Labrador Sea from the north west corner of the Gulf Stream. Additionally, the deep western boundary could not be traced south of 45°N. The authors concluded, that it might not be a boundary current at this location, but flows south further east on either side of the Mid-Atlantic Ridge. These observations are in good agreement with our model results.

In our model, the time scale of the oscillation is about 40 years, which is in the range of observed natural variability in the North Atlantic Ocean. On the other hand, the limitations of a model with one degree resolution and climatological forcing must be kept in mind. E.g. the mixing processes of mesoscale eddies, which could contribute to the exchange between the Gulf Stream and the adjacent DWBC ([SPALL, 1996b](#)), are only parametrised. Moreover, distorted physics was used for this study, which changes the time scales of barotropic Rossby and internal gravity waves.

The path of the Gulf Stream along the coast of North America, especially after Cape Hatteras, is very important for the oscillation. A general deficiency of large-scale models is that they fail to simulate the separation of the Gulf Stream from the coast at the correct location (Cape Hatteras) and the pathway downstream is too far north ([ROBERTS ET AL., 1996](#)). North of the observed Gulf Stream, a recirculation cell is observed, which is also underrepresented or missing in the models ([BOWER AND HOGG, 1996](#)). In the results presented here, the separation of the Gulf Stream also occurs too far north. Thus, the variability of the pathway of the Gulf Stream in the oscillation is restricted by this northerly position, where the range for variability is quite small. Numerous model investigations have been conducted to understand the reason for this model deficiency: [THOMPSON AND SCHMITZ, JR. \(1996\)](#) used a limited-area model of the NAC pathway region and varied the inflow of DWBC into the model area. The NAC Pathway agreed the best with the observations with a prescribed value of 20 Sv for the DWBC. [GERDES AND KÖBERLE \(1995\)](#) conducted comparable sensitivity studies with the same model as used in this thesis. There, the Pathway of the Gulf Stream became realistic when the authors enhanced the transport of Denmark Strait Overflow Water. Recently, [GERDES ET AL. \(2001\)](#) published the results of sensitivity experiments with an high resolution model of the Gulf Stream separation region. Here, the Gulf Stream separation at Cape Hatteras and a realistic northern recirculation cell was achieved by prescribing the eastern inflow of the northern recirculation cell at the Grand Banks. The authors concluded, that the DWBC sets up the cyclonic recirculation cell north of the Gulf Stream.

The oscillation which is discussed here is maintained by the interaction between the Gulf Stream and the DWBC. The DWBC varies in strength, forced by the convection in the Labrador Sea. This relocates the Gulf Stream to the south, which is in agreement with the studies discussed. As noted by [JOYCE ET AL. \(2000\)](#) and [GERDES ET AL. \(2001\)](#), the shift of the Gulf Stream position in turn produces SST anomalies that could influence

air-sea interaction and lead to a climate feedback loop.

7.4 Conclusions

The oscillation, which occurs in the long integration with the OMIP year as atmospheric forcing emerges as an interaction between the processes in the Labrador Sea and the position of the Gulf Stream and the NAC. The strength of the subpolar and subtropical gyres varies substantially in the course of the oscillation.

An analysis of the density differences between the first 300 m of the Labrador Sea and the 300 m beneath shows when convection occurs. In addition, the main density variability is found in the upper 300 m. These density differences are dominated by changes in the upper layer salinity. The density variability due to differences in temperature is small compared to the salinity differences and of opposite direction. The surface freshwater flux is exactly in phase with the overturning, with an enhanced input of freshwater at times when the convection is strong. This should counteract the convection, but the surface freshwater fluxes are too small to be of importance for the Labrador Sea convection in this experiment. Thus, the changes of the lateral fluxes into the Labrador Sea govern the oscillation. The position of the NAC is highly variable in the course of the oscillation: It can be found near 30°W when the overturning increases, and in the centre of the Labrador Sea, at 52°W, when the overturning decreases.

The cycle is sketched in Fig 7.12. At the beginning of an oscillation cycle, here taken as the state with minimum overturning, the NAC follows a north–east pathway before finally turning northward at 35°W. The NAC transports warm and saline water of subtropical origin. It cools after leaving the North American continent and becomes denser. In this state, there is no convection in the Labrador Sea but the surface density increases. In the next phase, the overturning and the strength of the subtropical and subpolar gyres increase. The dense water of the NAC is imported by a meander from the east into the Labrador Sea to compensate for the increased sinking. This further increases the surface density. The doming of the isopycnals in the Labrador Sea is enhanced and convection to mid depth sets in as a consequence. In the following phase, the overturning reaches its maximum value and there is deep convection in the Labrador Sea. At the same time, the supply of warm and saline water from the subtropics decreases. The enhanced convection increases the transport of the DWBC to the south, thereby raising the isopycnals between the DWBC and the Gulf Stream. By the afore–mentioned vorticity argument, the Gulf Stream is displaced to the south. The inflow of dense water from the east into the Labrador Sea decreases because of the reduced salt transport and relocation of the Gulf Stream. The convection site in the Labrador Sea shifts to the north–west. In the last phase of the cycle, the stratification in the Labrador Sea becomes stable with a lens of cold and freshwater in the upper 300 m. The light water is supplied by import via the Davis Strait and the East Greenland Current and supplemented by the surface fluxes. These fluxes do not change significantly during the cycle but can surpass the inflow of saline water

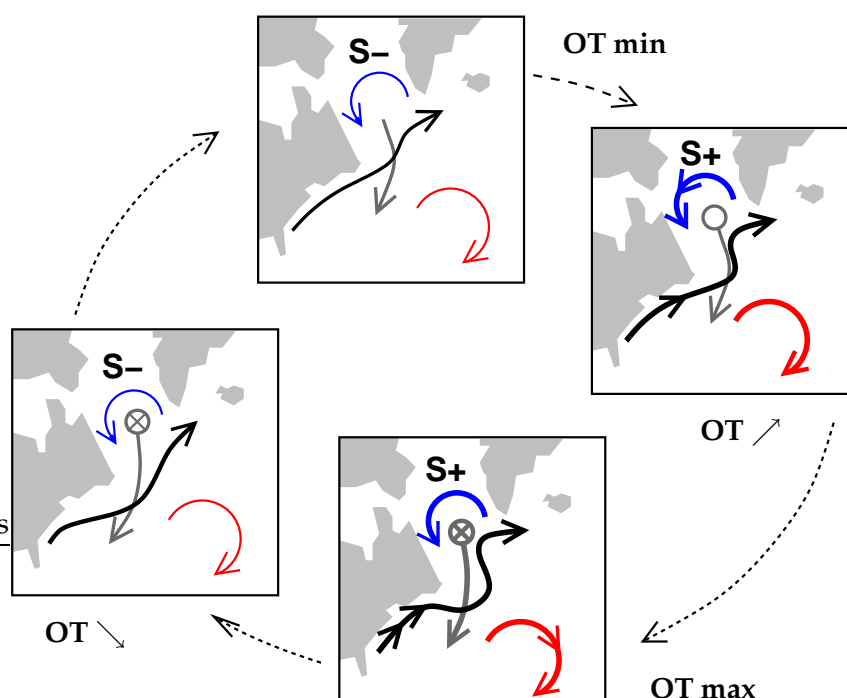


Figure 7.12: Sketch of an oscillation cycle; the black arrow indicates the pathway and strength of the NAC; the grey arrow the pathway and strength of the DWBC; grey circle and cross stand for mid-depth and deep convection; the red circle denotes the strength of the subtropical gyre, the blue circle the strength of the subpolar gyre; $S-(S+)$ is a negative (positive) salinity anomaly

with NAC during this part of the cycle. The freshwater inhibits convection and with less supply from the Labrador Sea, the DWBC weakens. The position of the isopycnal between the DWBC and the Gulf Stream is lowered, and the Gulf Stream relocates back to the north. From this point, the cycle of the oscillation starts again, because the NAC can again import dense water into the Labrador Sea, which will restart the convection.

In our analysis, we did not find a large pool of anomalous warm and saline or cold and fresh water, which could set the time scale of our oscillation (STOCKER, 1996). The period of the presented oscillation is more comparable to the advective-convective mechanism of YIN AND SARACHIK (1995). Anomalous warm and saline water is advected with the Gulf Stream into the Labrador Sea, where the convection site is located. Convection sets in and the deep water formation starts, which modifies the transport of the DWBC. The increasing production rate of the deep water combined with the slowly enhancing transport of the DWBC changes finally the pathway of the Gulf Stream, which cuts off rather abruptly the supply of warm and saline water to the convection site. The memory effect of the Labrador Sea could be also of importance (compare Section 6.4). Further investigations of the oscillation are necessary to specify the exact time scale of the advective and the convective mechanism.

8 Final conclusions and outlook

In the presented study, interannual and multidecadal time scales of natural variability of the North Atlantic ocean–sea ice system are investigated with the help of a coupled ocean–sea ice model.

The ocean model is a general circulation model in z -coordinates developed on the basis of the MOM-2 code of the GFDL (PACANOWSKI, 1995). It is coupled to a dynamic–thermodynamic sea ice model with viscous–plastic rheology (HIBLER, 1979; HARDER, 1996). The horizontal resolution is $1^\circ \times 1^\circ$ with 19 vertical levels. The area of the model comprises the Arctic and North Atlantic Ocean, with an open boundary at approximately 20°S .

One of the main interests of this study is the reaction of the coupled ocean–sea ice model to changes in the atmospheric surface forcing, which are related to the NAO. For this purpose, one composite for positive NAO years and one for negative NAO years is derived from the data of the NCAR/NCEP reanalysis project (KALNAY ET AL., 1996); the composite comprise annual climatologies for the surface boundary conditions. Additionally, a climatological forcing (OMIP year) is used, which consists of a typical year of the ECMWF reanalysis project data (GIBSON ET AL., 1997). As the data cover the period 1979–1993, the OMIP year is somewhat biased towards a positive NAO index.

The NAO+ composite shows strengthened wind stresses in the west wind drift zone with a northward relocation of the main pathway over Europe compared to the NAO– composite. The air temperature which is associated with the NAO+ composite is warmer over the Nordic Seas and the Barents Sea, but colder over the Labrador Sea, capturing the main observed effects of positive NAO years. A comparison between the three forcing sets reveals that the magnitude of the wind stress fields of the OMIP year is less than in the NAO composites, but in mid–latitude, the OMIP year shows a close resemblance to the NAO+ composite.

The three atmospheric data sets are used to integrate the model for 200 years each. The main characteristics of the ocean and sea ice field are compared, using mean states of the years 150–200. All experiments show a Gulf Stream separation that is too far north compared to observations, and the northern recirculation is missing completely. These are known deficiencies of coarse resolution models. Additionally, the NAC is found in the western subpolar North Atlantic Ocean in all experiments and the surface water mass in the subpolar gyre is warmer and more saline than in the observations. In the subtropical North Atlantic, the tracer distribution resembles the observations in the mean of years 150–200 compared to the mean of years 10–60. The maximum of the meridional overturning at 48°N and 1500 m depth reveals two features which are common in all three

spin up integrations. First, after an initial drop of the maximum of the overturning, there is a long trend lasting for almost 100 years or more. In the integration with the NAO– composite, this trend even lasts as long as the integration period is. Second, all experiments show multidecadal variability at least in the last fifty years of integration. The standard deviation for the NAO– experiment in this period is 1.5 Sv and 2.5 Sv for the NAO+ experiment.

The influence of a switch from a long time NAO+ state to an enduring NAO– situation is investigated on the basis of the 200 year integration with NAO+ forcing. The sea ice extent increases quickly in the margins of the ice covered areas in the Arctic Ocean, Nordic Seas and Labrador Sea after this switch: positive anomalies are detected in the Barents and Greenland Seas, negative anomalies in the Labrador Sea. This dipole pattern agrees with the combined model–observations analysis of [KAUKER ET AL. \(2003\)](#). The changes in the sea ice volume adapt slower to the changed forcing, because of the integral effect of the ocean mixed layer and ice thickness itself. In the NAO– case, the total sea ice volume increases gradually. Switching only the wind stress to the NAO– situation helps to separate the influence of wind stress forcing from the thermohaline forcing. The NAO– wind stress distribution relocates the sea ice margin very fast, but NAO+ air temperature melts more ice. Changing the initial forcing of NAO+ for one year to NAO– and then back to NAO+ leads to an almost instantaneous recover of the sea ice extent, but also to a long term change in the sea ice cover in the Labrador Sea, which persists due to permanent changes in the ocean. The ocean itself adjusts with a fast barotropic circulation anomaly, accompanied by an enhancement of meridional overturning and northward heat transport at 48°N. The slow response is a substantial decrease of the northward heat transport, which is caused by a reduction of the transport of subpolar and subtropical gyre and a decrease of the meridional overturning. In the experiment where only the wind stress is changed, the adaption to NAO– wind stress forcing is damped strongly by the NAO+ thermohaline forcing. The gyres decrease, but slower than in the NAO– case. The baroclinic adaption is different, because the heat fluxes counteract the wind stress forcing and adapt the meridional overturning and the heat transport to the North to only slightly reduced values. [EDEN AND WILLEBRAND \(2001\)](#) found a similarly fast and slow reaction to abrupt changes in the sign of NAO related forcing, but the amplitudes were different compared to the presented sensitivity experiments. Analysis of hydrographic sections revealed a decrease in northward heat transport two years after a shift from NAO+ to NAO– at 47°N ([BERSCH, 2002](#)). One year of NAO– forcing shifts the area of convection in the Labrador Sea to a different position, which turns out to be a new state of equilibrium for the ocean.

The OMIP experiment starts to oscillate strongly after 80 years of integration, with a peak to peak amplitude of 10 Sv and a period of 40 years. The amplitude and period of the oscillation did not decrease in a long term integration over 1000 years, which suggests that it is not a transient phenomenon. The oscillation is sustained by processes involving the Labrador Sea and the position of the Gulf Stream/NAC system. A stability

analysis of the surface layers of the Labrador Sea reveals that the occurring density differences are dominated by changes in the upper layer salinity. The effects of temperature changes are small and they act to stabilise the water column, where the salinity effect destabilises it. Surface freshwater fluxes over the Labrador Sea were ruled out as possible forcing mechanism, as they also act to stabilise the water column. The main contributor of saline surface water to the Labrador Sea is the NAC. Warm and saline subtropical surface water is advected with the Gulf Stream and the NAC to the north. When the maximum of the overturning is increasing, the NAC transports this water from the east into the Labrador Sea. The anomalies destabilise the water column and convection sets in. The convection enhances the deep water formation and the transport of the DWBC to the south increases. This increase raises the isopycnals between the DWBC and the Gulf Stream. Due to conservation of potential vorticity, the Gulf Stream is relocated to the south. This displacement suppresses the transport of subtropical surface water into the Labrador Sea and the convection and the maximum of the meridional overturning decreases. The transport of the DWBC weakens simultaneously, and the Gulf Stream is shifting back to the north. This closes the cycle of the oscillation. The time scale of the oscillation is governed by the advection of warm and saline water by the Gulf Stream into the Labrador Sea and the subsequent increase of convection and deep water formation and changes in the DWBC/Gulf Stream system. The period of 40 years of the oscillation lies in the range where observed SST anomalies showed interdecadal variability (MANN AND PARK, 1996; TOURRE ET AL., 1999; DELWORTH AND MANN, 2000): on time scales of 50–60 years. Other model studies also detected internal oceanic variability (DELWORTH ET AL., 1993; GREATBATCH AND ZHANG, 1995; TIMMERMANN ET AL., 1998) with comparable time scales. The mechanism of the oscillation of DELWORTH ET AL. (1993) was based on the advection of SST anomalies, which also influenced the convection region in the subpolar North Atlantic. GREATBATCH AND ZHANG (1995) claimed that changes in the surface heat fluxes were responsible for their oscillation. Variability of the position of the Gulf Stream and of the underlying DWBC were detected previously in observations (JOYCE ET AL., 2000; LAVENDER ET AL., 2000; RHEIN, 2000) and also in model studies SPALL (1996a,b).

The captured oscillation is a very interesting starting point for further investigation. The sensitivity to the surface boundary conditions could be analysed further by running the model with prescribed climatological heat and/or freshwater fluxes with an annual cycle. This would be a way to test the stability of the oscillation. A passive tracer release experiment would be helpful to calculate the time scale of the oscillation similar to EDEN AND GREATBATCH (2003). A further comparison between the results of the oscillation and the sensitivity experiments is also possible, because the position of the Gulf Stream is affected by the change from NAO+ to NAO– related forcing (see Fig. 6.10). The variability of the Gulf Stream/DWBC system is also interesting to investigate, e.g. calculating the potential vorticity in detail and quantifying the transports. Employing a fully coupled atmosphere–ocean–sea ice model is a next step to improve the understanding of

interactions between atmosphere and ocean.

Integrations of an atmospheric general circulation model which were forced with prescribed SSTs could capture the observed NAO index in an ensemble mean state (RODWELL ET AL., 1999). Long term weather forecasts with such a model seem to be possible with the limitation that the SST must be known. Another attempt of predicting the NAO index for several years was made by EDEN ET AL. (2002). The authors improved the prediction skill by using a realistic ocean model to force a very simple coupled model of BRETHERTON AND BATTISI (2000). Recently, SIRABELLA ET AL. (2001) were able to prove that there is a very strong and statistically significant link between the North Atlantic winter sea level pressure (SLP) field and the Barents Sea upper layer temperature. This link affects as stated by the authors the cod recruitment in this area through the SST. Thus prediction of SST in the North Atlantic could be a starting point for the prediction of cod recruitment. However, for the predictability of cod recruitment it is necessary to keep in mind that the changing water temperature is only one factor among others, such as changes in the predator field or in the food chain, to name just a few. In this sense, the understanding of the processes (oceanic and/or atmospheric) which drives the SST anomalies is important for the prediction of future climate scenarios and also somewhat for the future of the cod.

Bibliography

- AAGAARD, K. and E. C. CARMACK, 1989: The role of sea ice and other fresh water in the Arctic Circulation, *J. Geophys. Res.*, **94** (C10), 14485 – 14498.
- AAGAARD, K., J. SWIFT and E. C. CARMACK, 1985: Thermohaline circulation in the Arctic Mediterranean Seas, *J. Geophys. Res.*, **90** (C3), 4833 – 4846.
- ALEXANDER, M. A. and C. DESER, 1995: A mechanism for the recurrence of wintertime midlatitude SST anomalies, *J. Climate*, **25**, 122 – 127.
- AMBAUM, M. H., B. J. HOSKINS and D. B. STEPHENSON, 2001: Arctic Oscillation or North Atlantic Oscillation?, *J. Climate*, **14**, 3495 – 3507.
- ANDERSON, D. L. T., K. BRYAN, A. E. GILL and R. C. PACANOWSKI, 1979: The transient response of the North Atlantic: some model studies, *J. Geophys. Res.*, **84**, 4795 – 4815.
- BACKHAUS, J., H. FOHRMANN, J. KÄMPF and A. RUBINO, 1997: Formation and export of water masses produced in Arctic shelf polynyas - process studies of oceanic convection, *ICES J. Mar. Sci.*, **54**, 366 – 382.
- BACON, S., W. GOULD and Y. JIA, 2003: Open-ocean convection in the Irminger Sea, *Geophys. Res. Letters*, **30** (5), doi:10.1029/2002GL016271.
- BARNSTON, A. G. and R. E. LIVEZEY, 1987: Classification, seasonality and persistence of low - frequency atmospheric circulation patterns, *Monthly Weather Review*, **115**, 1083 – 1126.
- BELKIN, I. M., S. LEVITUS, J. ANTONOV and S.-A. MALMBERG, 1998: “Great Salinity Anomalies” in the North Atlantic, *Prog. Oceanog.*, **41**, 1 – 68.
- BERSCH, M., 2002: North Atlantic Oscillation - induced changes of the upper layer circulation in the northern North Atlantic Ocean, *J. Geophys. Res.*, **107** (C10), doi:10.1029/2001JC000901.
- BERSCH, M., J. MEINCKE and A. SY, 1999: Interannual thermohaline changes in the northern North Atlantic 1991–1996, *Deep-Sea Res. II*, **46**, 55 – 75.
- BITZ, C. and G. ROE, 2003: A physical explanation for the high rate of sea-ice thinning in the Arctic Ocean, *Geophys. Res. Letters*, submitted.

Bibliography

- BJERKNES, J., 1964: Atlantic air–sea interaction, *Adv. Geophysics*, **10**, 1 – 82.
- BÖNING, C. W., F. O. BRYAN and W. R. HOLLAND, 1996: Deep-water formation and meridional overturning in a high-resolution model of the North Atlantic, *J. Phys. Oceanogr.*, **26** (7), 1142 – 1164.
- BÖNING, C. W., M. RHEIN, J. DENG G and C. DOROW, 2003: Modeling CFC inventories and formation rates of Labrador Sea Water, *Geophys. Res. Letters*, **30** (2), 10.1029/2002GL014855.
- BOWER, A. S. and N. G. HOGG, 1996: Structure of the Gulf Stream and its recirculation at 55°W, *J. Phys. Oceanogr.*, **26**, 1002 – 1022.
- BREHERTON, C. and D. BATTISI, 2000: An interpretation of the results from atmospheric general circulation models forced by the time history of the observed sea surface temperature distribution, *Geophys. Res. Letters*, **27** (6), 767 – 770.
- BROECKER, W. S., 1991: The Great Ocean Conveyor, *Oceanography*, **4**, 79 – 89.
- BRYAN, F., 1986: High latitude salinity effects and inter-hemispheric thermohaline circulations, *Nature*, **323**, 421 – 424.
- BRYAN, K., 1962: Measurements of the meridional heat transport by ocean currents, *J. Geophys. Res.*, **67** (9), 3403 – 3414.
- BRYAN, K., 1969: A Numerical Method for the Study of the Circulation of the World Ocean, *J. Climate*, **4**, 347 – 376.
- BRYAN, K., 1984: Accelerating the convergence to equilibrium of ocean–climate models, *J. Phys. Oceanogr.*, **14** (4), 666 – 673.
- BUDYKO, M. I., 1974: *Climate and life*, vol. 18 of *International Geophysics Series*, Academic Press, New York, 508 pp.
- CAVALIERI, D. J., P. GLOERSEN, C. L. PARKINSON, J. C. COMISO and H. J. ZWALLY, 1997: Observed hemispheric asymmetry in global sea ice changes, *Science*, **278**, 1104 – 1106.
- CAYAN, D. R., 1992: Latent and sensible heat flux anomalies over the Northern Oceans: the connection of the monthly atmospheric circulation, *J. Climate*, **5**, 354 – 369.
- CHAPMAN, W. L. and J. E. WALSH, 1993: Recent variations of sea ice and air temperature in high latitudes, *Bull. Amer. Met. Soc.*, **74** (1), 33 – 48.
- COLONY, R. and A. S. THORNDIKE, 1984: An estimate of the mean field of Arctic sea ice motion, *J. Geophys. Res.*, **89** (C6), 10623 – 10629.

- COON, M. D., A. MAYKUT, R. S. PRITCHARD, D. A. ROTHROCK and A. S. THORNDIKE, 1974: Modeling the pack ice as an elastic-plastic material, *AIDJEX Bulletin*, pp. 1 – 105.
- COX, M. D., 1984: A primitive equation 3-dimensional model of the ocean, Technical report no. 1, GFDL Ocean Group, Princeton.
- CURRY, R. G. and M. S. MCCARTNEY, 2001: Ocean gyre circulation changes associated with the North Atlantic Oscillation, *J. Phys. Oceanogr.*, **31**, 3374 – 3400.
- CURRY, R. G., M. S. MCCARTNEY and T. M. JOYCE, 1998: Oceanic transport of subpolar climate signals to mid-depth subtropical waters, *Nature*, **391**, 575 – 577.
- CZAJA, A., A. W. ROBERTSON and T. HUCK, 2003: The role of the Atlantic ocean-atmosphere coupling in affecting the North Atlantic Oscillation variability, in *The North Atlantic Oscillation Climate Significance and Environmental Impacts*, no. 134 in Geophysical Monograph Series, pp. 147 – 172, American Geophysical Union.
- DELWORTH, T. and R. GREATBATCH, 2000: Multidecadal thermohaline circulation variability driven by atmospheric surface flux forcing, *J. Climate*, **13**, 1481 – 1495.
- DELWORTH, T., S. MANABE and R. J. STOUFFER, 1993: Interdecadal variations of the thermohaline circulation in a coupled ocean-atmosphere model, *J. Climate*, **6** (11), 1993 – 2011.
- DELWORTH, T. and M. MANN, 2000: Observed and simulated multidecadal variability in the Northern hemisphere, *Climate Dynamics*, **16**, 661 – 676.
- DESER, C., 2000: On the teleconnectivity of the “Arctic Oscillation”, *Geophys. Res. Letters*, **27** (6), 779 – 782.
- DESER, C. and M. L. BLACKMON, 1993: Surface climate variations over the North Atlantic Ocean during winter: 1900 - 1989, *J. Climate*, **6** (9), 1743 – 1753.
- DESER, C., J. E. WALSH and M. S. TIMLIN, 2000: Arctic sea ice variability in the context of recent atmospheric circulation trends, *J. Climate*, **13** (3), 617 – 633.
- DICKSON, R. R. and J. BROWN, 1994: The production of North Atlantic Deep Water: Sources, rates and pathways, *J. Geophys. Res.*, **99** (C6), 12319 – 12341.
- DICKSON, R. R., E. M. GMITROWICZ and A. J. WATSON, 1990: Deep - water renewal in the North Atlantic, *Nature*, **344**, 848 – 850.
- DICKSON, R. R., J. LAZIER, J. MEINCKE, P. RHINES and J. SWIFT, 1996: Long - term coordinated changes in the convective activity of the North Atlantic, *Prog. Oceanog.*, **38**, 241 – 295.
- DICKSON, R. R., J. MEINCKE, S.-A. MALMBERG and A. LEE, 1988: The Great Salinity Anomaly in the northern North Atlantic 1968 - 1982, *Prog. Oceanog.*, **20**, 103 – 151.

Bibliography

- DICKSON, R. R., T. J. OSBORN, J. W. HURRELL, J. MEINCKE, J. BLINDHEIM, B. ADLANDSVIK, T. VINJE, G. ALEKSEEV and W. MASLOWSKI, 2000: The Arctic Ocean response to the North Atlantic Oscillation, *J. Climate*, **13** (15), 2671 – 2696.
- DIETERICH, C., 2003: *The turbulent life of phytoplankton*, Ph.D. thesis, University of Bremen, in preparation.
- DÖSCHER, R., C. W. BÖNING and P. HERRMANN, 1994: Response of meridional overturning and heat transport in the North Atlantic to changes in thermohaline forcing in the northern latitudes: a model study, *J. Phys. Oceanogr.*, **24**, 2306 – 2320.
- EDEN, C. and R. GREATBATCH, 2003: A damped decadal oscillation in the North Atlantic Oscillation climate system, *J. Climate*, submitted.
- EDEN, C., R. GREATBATCH and J. LU, 2002: Prospects for decadal prediction of the North Atlantic Oscillation (NAO), *Geophys. Res. Letters*, **29** (10), 10.1029.
- EDEN, C. and T. JUNG, 2001: North Atlantic interdecadal variability: Oceanic response to the North Atlantic Oscillation (1865-1997), *J. Climate*, **14** (5), 676–691.
- EDEN, C. and J. WILLEBRAND, 2001: Mechanism of interannual to decadal variability of the North Atlantic circulation, *J. Climate*, **14** (10), 2266 – 2280.
- EICKEN, H. and P. LEMKE, 2001: The response of polar sea ice to climate variability and change, in *Climate of the 21st Century: Changes and Risks*, J. L. Lozan, H. Graßl and P. Hupfer, eds., pp. 206 – 222, Lozan, José L., Wissenschaftliche Auswertungen, Hamburg.
- EICKEN, H., M. LENSU, M. LEPPÄRANTA, W. B. TUCKER III, A. GOW and O. SALMELA, 1995: Thickness, structure, and properties of level summer multi-year ice in the Eurasian sector of the Arctic Ocean, *J. Geophys. Res.*, **100** (C11), 22697 – 22710.
- ESSELBORN, S. and C. EDEN, 2001: Sea surface height changes in the North Atlantic Ocean related to the North Atlantic Oscillation, *Geophys. Res. Letters*, **28** (18), 3473 – 3476.
- EWG - ENVIRONMENTAL WORKING GROUP, 1997: *Joint U.S. Russian Atlas of the Arctic Ocean*, NSIDC/CIRES, University of Boulder, CO, USA.
- FANG, Z. and J. M. WALLACE, 1994: Arctic sea ice variability on a time scale of weeks and its relation to atmospheric forcing, *J. Climate*, **7**, 1897 – 1914.
- FRITZSCH, B., R. GERDES, W. HILLER, M. LATIF, S. LEGUTKE, E. MAIER-REIMER, D. OLBERS and F. ROESKE, 2000: Vergleich der thermohalinen Zirkulation in zwei globalen ozeanischen Zirkulationsmodellen - The Ocean Model Intercomparison Project, Tech. rep., Alfred-Wegener-Institut für Polar- und Meeresforschung, Bremerhaven, Germany, Abschlubericht BMBF Projekt 01 LA 9862/8.

- GANACHAUD, A. and C. WUNSCH, 2000: Improved estimates of global ocean circulation, heat transport and mixing from hydrographic data, *Nature*, **408**, 453 – 456.
- GENT, P. and J. MCWILLIAMS, 1990: Isopycnal mixing in ocean circulation models, *J. Phys. Oceanogr.*, **20**, 150 – 155.
- GERDES, R., 1989: The role of numerical advection schemes in general circulation models, in *Parametrisation of Small-Scale Processes, Proc. 'Aha Huliko'a, Hawaiian Winter Workshop*, P. Müller and D. Henderson, eds., pp. 21 – 57, Hawaii Institute of Geophysics.
- GERDES, R., A. BIASTOCH and R. REDLER, 2001: Fresh water balance of the Gulf Stream system in a regional model study, *Climate Dynamics*, **18**, 17 – 27.
- GERDES, R. and C. KÖBERLE, 1995: Influence of DSOW in a numerical model of the North Atlantic general circulation, *J. Phys. Oceanogr.*, **25** (11), 2624 – 2642.
- GERDES, R., C. KÖBERLE and J. WILLEBRAND, 1991: The influence of numerical advection schemes on the results of ocean general circulation models, *Climate Dynamics*, **5**, 211 – 226.
- GERDES, R. and U. SCHAUER, 1997: Large-scale circulation and water mass distribution in the Arctic Ocean from model results and observations, *J. Geophys. Res.*, **102** (C4), 8467 – 8483.
- GIBSON, J., P. KALLBERG, S. UPPALA, A. NOMURA, E. SERRANO and A. HERNANDEZ, 1997: ERA description. ECMWF reanalysis project report 1: project organisation, Tech. rep., European Centre for Medium Range Weather Forecast, Reading, UK.
- GILL, A. E., 1982: *Atmosphere–Ocean Dynamics*, International Geophysics Series, Vol. 30, Academic Press, London.
- GORDON, A. L., 1986: Interocean exchange of thermocline water, *J. Geophys. Res.*, **91** (C4), 5037 – 5046.
- GOURETSKI, V. V. and K. JANCKE, 1998: WOCE Report No. 162/98, Tech. Rep. 3, WHP Special Analysis Center,
<http://www.dkrz.de/~u241046/SACserver/SACHome.htm>.
- GREATBATCH, R., 2000: The North Atlantic Oscillation, *Stochastic Environmental Research and Risk Assessment*, **14**, 213 – 242.
- GREATBATCH, R. and S. ZHANG, 1995: An interdecadal oscillation in an idealised ocean basin forced by constant heat flux, *J. Climate*, **8** (1), 81 – 91.
- GROTEFENDT, K., K. LAGEMANN, D. QUADFASEL and S. RONSKI, 1998: Is the Arctic Ocean warming?, *J. Geophys. Res.*, **103** (C12), 27679 – 27687.

Bibliography

- HAAK, H., J. JUNGCLAUS, U. MIKOLAJEWICZ and M. LATIF, 2003: Formation and propagation of great salinity anomalies, *Geophys. Res. Letters*, **30** (9), doi:10.1029/2003GL017065.
- HÄKKINEN, S., 1993: An arctic source for the Great Salinity Anomaly: a simulation of the Arctic Ice-Ocean system for 1955 - 1975, *J. Geophys. Res.*, **98** (C9), 16397 – 16410.
- HÄKKINEN, S., 1999a: A simulation of thermohaline effects of a Great Salinity Anomaly, *J. Climate*, **12** (6), 1781 – 1795.
- HÄKKINEN, S., 1999b: Variability of the simulated meridional heat transport in the North Atlantic for the period 1951 - 1993, *J. Geophys. Res.*, **104** (C5), 10991 – 11007.
- HÄKKINEN, S., 2002: Freshening of the Labrador Sea surface waters in the 1990s: Another great salinity anomaly, *J. Climate*, **13**, 1195 – 1219.
- HALLIWELL, G. R., 1998: Simulation of North Atlantic decadal/multidecadal winter SST anomalies driven by basin-scale atmospheric circulation anomalies, *J. Phys. Oceanogr.*, **28** (1), 5 – 21.
- HANSEN, B., W. R. TURRELL and S. ØSTERHUS, 2001: Decreasing overflow from the Nordic Seas into the Atlantic Ocean through the Faroe Bank channel since 1950, *Nature*, **411**, 927 – 930.
- HARDER, M., 1996: Dynamics, roughness, and age of Arctic sea ice – Numerical investigations with a large-scale model, in *Reports on Polar Research*, vol. 203, Alfred-Wegener-Institut für Polar- und Meeresforschung, Bremerhaven, Germany, 126 pp.
- HIBLER, W., 1979: A dynamic thermodynamic sea ice model, *J. Phys. Oceanogr.*, **9**, 815 – 846.
- HIBLER, W. and K. BRYAN, 1987: A diagnostic ice-ocean model, *J. Phys. Oceanogr.*, **17**, 987 – 1015.
- HILMER, M. and T. JUNG, 2000: Evidence for a recent change in the link between the North Atlantic Oscillation and Arctic sea ice export, *Geophys. Res. Letters*, **27** (7), 989 – 992.
- HILMER, M. and P. LEMKE, 2000: On the decrease of arctic sea ice volume, *Geophys. Res. Letters*, **27**, 3751 – 3754.
- HOLLOWAY, G. and T. SOU, 2002: Has Arctic sea ice rapidly thinned?, *J. Climate*, **15** (13), 1691 – 1701.
- HU, A., C. ROTH, R. BLECK and C. DESER, 2002: NAO influence on sea ice extent in the Eurasian coastal region, *Geophys. Res. Letters*, **29** (22), 10.1029/2001GL014293.

- HURRELL, J., Y. KUSHNIR, G. OTTERSEN and M. VISBECK, eds., 2003: *The North Atlantic Oscillation Climate Significance and Environmental Impacts*, no. 134 in Geophysical Monograph Series, American Geophysical Union.
- HURRELL, J. W., 1995: Decadal trends in the North Atlantic Oscillation: regional temperatures and precipitation, *Science*, **269**, 676 – 679.
- JAMES, I. and P. M. JAMES, 1989: Ultra low frequency variability in a simple atmospheric circulation model, *Nature*, **342**, 53 – 55.
- JOHANNESSEN, O. M., E. V. SHALINA and M. W. MILES, 1999: Satellite evidence for an Arctic sea ice cover in transformation, *Science*, **286**, 1937 – 1939.
- JONES, P., T. JONSSON and D. WHEELER, 1997: Extension to the North Atlantic Oscillation using early instrumental pressure observations from Gibraltar and South-West Iceland, *Int. J. Climatology*, **17**, 1433 – 1450.
- JONSSON, J., 1994: Fishery of iceland, 1600–1900, *ICES Mar Sci. Symp.*, **198**, 3 – 16.
- JOYCE, T. M., C. DESER and M. A. SPALL, 2000: On the relation between decadal variability of Subtropical Mode Water and the North Atlantic Oscillation, *J. Climate*, **13**, 2550 – 2569.
- KALNAY, E., M. KANAMITSU, R. KISTLER, W. COLLINS, D. DEAVEN, L. GANDIN, M. IREDELL, S. SAHA, G. WHITE, J. WOOLLEN, Y. ZHU, A. LEETMAA, R. REYNOLDS, M. CHELLIAH, W. EBISUZAKI, W. HIGGINS, J. JANOWIAK, K. MO, C. ROPELEWSKI, J. WANG, R. JENNE and D. JOSEPH, 1996: The NCEP/NCAR 40-year Reanalysis Project, *Bull. Amer. Met. Soc.*, **77** (3), 437 – 495.
- KARCHER, M., R. GERDES, F. KAUKER and C. KÖBERLE, 2003: Arctic warming: evolution and spreading of the 1990s warm event in the Nordic seas and Arctic Ocean, *J. Geophys. Res.*, **108** (C2), doi:10.1029/2001JC001265.
- KÄSE, R. H., J. B. GIRTON and T. SANFORD, 2003: Structure and variability of the Denmark Strait Overflow: model and observations, *J. Geophys. Res.*, **108** (C6), doi:10.1029/2002JC001548.
- KAUKER, F., R. GERDES, M. KARCHER, C. KÖBERLE and J. L. LIESER, 2003: Variability of northern hemisphere sea ice: a combined analysis of model results and observations from 1978 to 2001, *J. Geophys. Res.*, **108** (C6), doi:10.1029/2002JC001573.
- KHATIWALA, S., P. SCHLOSSER and M. H. VISBECK, 2002: Rates and mechanisms of water mass formation in the Labrador Sea as inferred from tracer observations, *J. Phys. Oceanogr.*, **32**, 666 – 686.
- KÖBERLE, C. and R. GERDES, 2003: Mechanisms determining the variability of the Arctic sea ice conditions and export, *J. Climate*, **16**, 2843 – 2858.

Bibliography

- KREYSCHER, M., 1998: Dynamics of Arctic sea ice – Validation of different rheology schemes for the use in climate models, in *Reports on Polar Research*, vol. 291, Alfred-Wegener-Institut für Polar- und Meeresforschung, Bremerhaven, Germany, 116 pp.
- KREYSCHER, M., M. HARDER, P. LEMKE and G. M. FLATO, 2000: Results of the Sea Ice Model Intercomparison Project: Evaluation of sea ice rheology schemes for use in climate simulations, *J. Geophys. Res.*, **105** (C5), 11299 – 11320.
- KURLANSKY, M., 1997: *Cod: The Biography of a Fish That Changed the World*, Walker & Company.
- KUSHNIR, Y., 1994: Interdecadal variations in North Atlantic sea surface temperature and associated atmospheric conditions, *J. Climate*, **7** (1), 141 – 157.
- KWOK, R., 2000: Recent changes in the Arctic Ocean sea ice motion associated with the North Atlantic Oscillation, *Geophys. Res. Letters*, **27** (6), 775 – 778.
- KWOK, R. and D. ROTHROCK, 1999: Variability of Fram Strait ice flux and North Atlantic Oscillation, *J. Geophys. Res.*, **104** (C3), 5177 – 5189.
- LAB SEA GROUP, 1998: The Labrador Sea deep convection experiment, *Bull. Amer. Met. Soc.*, **79** (10), 2033 – 2058, <http://www.ldeo.columbia.edu/~visbeck/labsea>.
- LATIF, M., E. ROECKNER, U. MIKOLAJEWICZ and R. VOSS, 2000: Tropical stabilization of the thermohaline circulation in a greenhouse warming simulation, *J. Climate*, **13**, 1809 – 1813.
- LAVENDER, K. L., R. E. DAVIS and W. BRECHNER OWENS, 2000: Mid-depth recirculation observed in the interior Labrador and Irminger seas by direct velocity measurements, *Nature*, **407**, 66 – 69.
- LAZIER, J., R. HENDRY, A. CLARKE, I. YASHAYAEV and P. RHINES, 2002: Convection and restratification in the Labrador Sea, 1990 - 2000, *Deep-Sea Res.*, **49**, 1819 – 1835.
- LAZIER, J. R. N., 1988: Temperature and salinity changes in the deep Labrador Sea, *Deep-Sea Res.*, **35**, 1247 – 1253.
- LEMKE, P., E. TRINKL and K. HASSELMANN, 1980: Stochastic dynamic analysis of polar sea ice variability, *J. Phys. Oceanogr.*, **10** (12), 2100 – 2120.
- LENDERINK, G. and R. J. HAARSMA, 1994: Variability and multiple equilibria of the thermohaline circulation associated with deep-water formation, *J. Phys. Oceanogr.*, **24**, 1480 – 1493.
- LEVITUS, S., R. BURGETT and T. BOYER, 1994: *World Ocean Atlas 1994, vol. 3, Salinity, and vol. 4, Temperature*, NOAA Atlas NESDIS 3 & 4, U.S. Dep. of Comm., Washington, D.C.

- MACDONALD, A. M. and C. WUNSCH, 1996: An estimate of global ocean circulation and heat fluxes, *Nature*, **382**, 436 – 439.
- MALMBERG, S.-A. and S. JÓNSSON, 1997: Timing of deep convection in the Greenland and Iceland Seas, *ICES J. Mar. Sci.*, **54** (3), 300 – 309.
- MANN, M. E. and J. PARK, 1996: Joint spatio-temporal modes of surface temperature and sea level pressure variability in the northern hemisphere during the last century, *J. Climate*, **9** (9), 2137 – 2162.
- MARSH, R., 2000: Recent variability of the North Atlantic thermohaline circulation inferred from surface heat and freshwater fluxes, *J. Climate*, **13**, 3239 – 3260.
- MARSHALL, J. and F. SCHOTT, 1999: Open - ocean convection: observations, theory and models, *Review of Geophysics*, **37** (1), 1 – 64.
- MAURITZEN, C. and S. HÄKKINEN, 1997: Influence of sea ice on the thermohaline circulation in the Arctic - North Atlantic Ocean, *Geophys. Res. Letters*, **24** (24), 3257 – 3260.
- MCCARTNEY, M. S. and L. D. TALLEY, 1982: The subpolar mode water of the North Atlantic Ocean, *J. Phys. Oceanogr.*, **12**, 1169 – 1188.
- MCPHEE, M. G., 1979: The effect of oceanic boundary layer on the mean drift of pack ice: Applications of a simple model, *J. Phys. Oceanogr.*, **9**, 388 – 400.
- MERTZ, G. and D. G. WRIGHT, 1992: Interpretations of the JEBAR term, *J. Phys. Oceanogr.*, **22**, 301 – 305.
- MESINGER, F. and A. ARAKAWA, 1976: Numerical methods used in atmospheric models, Tech. rep., GARP Publication Series, No. 17, Vol.I.
- MIKOLAJEWICZ, U. and E. MAIER-REIMER, 1990: Internal secular variability in an ocean general circulation model, *Climate Dynamics*, **4** (3), 145 – 156.
- MIKOLAJEWICZ, U. and E. MAIER-REIMER, 1994: Mixed boundary conditions in ocean general circulation models and their influence on the stability of the model's conveyor belt, *J. Geophys. Res.*, **99**, 22633 – 22644.
- MONAHAN, A. H., J. C. FYFE and G. M. FLATO, 2000: A regime view of northern hemisphere atmospheric variability and change under global warming, *Geophys. Res. Letters*, **27** (8), 1139 – 1142.
- MONTEREY, G. I. and S. LEVITUS, 1997: Seasonal variability of mixed layer depth for the world ocean, NOAA Atlas NESDIS 14, NOAA, Washington, D.C.
- MORISON, J. H., M. G. MCPHEE and G. A. MAYKUT, 1987: Boundary layer, upper ocean, and ice observations in the Greenland Sea marginal ice zone, *J. Geophys. Res.*, **92** (C7), 6987 – 7011.

Bibliography

- MÜLLER, P. and J. WILLEBRAND, 1989: *Numerical data and functional relationships in science and technology*, vol. 3: Oceanography of *Landolt Börnstein, New Series*, chap. Equations for oceanic motions, pp. 1 – 14, Springer Verlag, Berlin.
- MYSAK, L. A., T. F. STOCKER and F. HUANG, 1993: Century-scale variability in a randomly forced, two-dimensional thermohaline ocean circulation model, *Climate Dynamics*, **8**, 103 – 116.
- NAMIAS, J. and R. M. BORN, 1970: Temporal coherence in the North Pacific sea-surface temperature patterns, *J. Geophys. Res.*, **75**, 5952 – 5955.
- NANSEN, F., 1906: *Northern waters: Captain Roald Amundsen's Oceanographic Observations in the Arctic Seas in 1901*, Matematisk-Naturv. Klasse No.3, Videnskabs-Selskabets Skrifter I, Christiania.
- NEW, A. L., Y. JIA, M. COULIBALY and J. DENG, 2001: On the role of the Azores Current in the ventilation of the North Atlantic Ocean, *Prog. Oceanog.*, **48** (2-3), 163 – 194.
- NOAA, 1988: Data Announcement 88-MGG-02, Digital relief of the Surface of the Earth., Tech. rep., NOAA, National Geophysical Data Center, Boulder, Colorado.
- OSBORN, T. J., K. R. BRIFFA, S. F. B. TETT and P. D. JONES, 1999: Evaluation of the North Atlantic Oscillation as simulated by a coupled climate model, *Climate Dynamics*, **15**, 685 – 702.
- OTTERÅ, O. H., H. DRANGE, M. BENTSEN, N. KVAMSTØ and D. JIANG, 2003: The sensitivity of the present day Atlantic meridional overturning circulation to anomalous freshwater input, *Geophys. Res. Letters*, **30**, doi:10.1029/2003GL017578.
- OWENS, W. B. and P. LEMKE, 1990: Sensitivity studies with a sea ice-mixed layer-pycnocline model in the Weddell Sea, *J. Geophys. Res.*, **95** (C6), 9527 – 9538.
- PACANOWSKI, R. C., 1995: MOM 2 Documentation, User's Guide and Reference Manual, Tech. Rep. 3, GFDL Ocean Group, Princeton, New Jersey.
- PARKINSON, C. L., D. J. CAVALIERI, P. GLOERSEN, H. J. ZWALLY and J. C. COMISO, 1999: Arctic sea ice extents, areas, and trends, 1978-1996, *J. Geophys. Res.*, **104** (C9), 20837 – 20856.
- PARKINSON, C. L. and W. M. WASHINGTON, 1979: A large-scale numerical model of sea ice, *J. Geophys. Res.*, **84** (C1), 311 – 337.
- PICKART, R., D. J. TORRES and R. A. CLARKE, 2002: Hydrography of the Labrador Sea during active convection, *J. Phys. Oceanogr.*, **32**, 428 – 456.
- PICKART, R. S., 1992: Water mass components of the North Atlantic Deep Western Boundary Current, *Deep-Sea Res.*, **39**, 1553 – 1572.

- PLANQUE, B. and T. FRÉDOU, 1999: Temperature and the recruitment of Atlantic cod (*gadus morhua*), *Can. J. Fish. Aquat. Sci.*, **56**, 2069 – 2077.
- POLLARD, R. and S. PU, 1985: Structure and circulation of the upper Atlantic Ocean and that of the Azores, *Prog. Oceanog.*, **145**.
- PROSHUTINSKY, A. Y. and M. A. JOHNSON, 1997: Two circulation regimes of the wind-driven Arctic Ocean, *J. Geophys. Res.*, **102** (C6), 12493 – 12514.
- RAHMSTORF, S., 1993: A fast and complete convection scheme for ocean models, *Ocean Modelling*, unpublished manuscript.
- REVERDIN, G. and N. VERBRUGGE, 1999: Upper ocean variability between Iceland and Newfoundland 1993–1998, *J. Geophys. Res.*, **104** (C12), 29599 – 29611.
- RHEIN, M., 1994: The deep western boundary current: tracers and velocities, *Deep-Sea Res.*, **41** (2), 263 – 281.
- RHEIN, M., 2000: Drifters reveal deep circulation, *Nature*, **407**, 30 – 31.
- RHEIN, M., J. FISCHER, W. SMETHIE, D. SMYTHE-WRIGHT, R. WEISS, C. MERTENS, D.-H. MIN, U. FLEISCHMANN and A. PUTZKA, 2002: Labrador sea water: Pathways, CFC inventory, and formation rates, *J. Phys. Oceanogr.*, **32** (2), 648 – 665.
- RIGOR, I. G., R. L. COLONY and S. MARTIN, 2000: Variations in surface air temperature observations in the Arctic, 1979–97, *J. Climate*, **13**, 896 – 914.
- RIGOR, I. G., J. M. WALLACE and R. L. COLONY, 2002: Response of sea ice to the Arctic Oscillation, *J. Climate*, **15**, 2648 – 2663.
- ROBERTS, M. J., R. MARSH, A. L. NEW and R. WOOD, 1996: An intercomparison of a Bryan–Cox–type ocean model and an isopycnic ocean model. Part I: the subpolar gyre and high–latitude process, *J. Phys. Oceanogr.*, **26**, 1495 – 1527.
- RODWELL, M., D. ROWELL and C. FOLLAND, 1999: Oceanic forcing of the wintertime North Atlantic Oscillation and European climate, *Nature*, **398**, 320 – 323.
- ROEMMICH, D. and C. WUNSCH, 1985: Two transatlantic sections: meridional circulation and heat flux in the subtropical North Atlantic Ocean, *Deep-Sea Res.*, **32**, 619–664.
- ROGERS, J., 1984: The association between the North Atlantic Oscillation and the Southern Oscillation in the Northern Hemisphere, *Monthly Weather Review*, **112**, 1999 – 2015.
- ROGERS, J. C., 1997: North Atlantic storm track variability and its association to the North Atlantic Oscillation and climate variability of Northern Europe, *J. Climate*, **10**, 1635 – 1647.

Bibliography

- ROSATI, A. and K. MIYAKODA, 1988: A general circulation model for upper ocean simulation, *J. Phys. Oceanogr.*, **18** (11), 1601 – 1626.
- ROTHROCK, D. A., Y. YU and G. A. MAYKUT, 1999: Thinning of the Arctic Sea-Ice Cover, *Geophys. Res. Letters*, **26** (23), 3469 – 3472.
- RUDELS, B., 1998: *Physics of ice-covered seas*, vol. 2, chap. Aspects of arctic oceanography, pp. 517 – 568, University of Helsinki.
- RUDELS, B., G. BJÖRK, R. D. MUENCH and U. SCHAUER, 1999: Double-diffusive layering in the Eurasian Basin of the Arctic Ocean, *J. Mar. Sys.*, **21**, 3–27.
- SARKISYAN, A. S. and V. F. IVANOV, 1971: Joint effect of baroclinicity and bottom relief as an important factor in the dynamics of sea currents, *Izv. Acad. Sci., USSR, Atmos. and Oceanic Phys.*, **7** (2), 173 – 188, Engl. transl.
- SCHLESINGER, M. E. and N. RAMANKUTTY, 1994: An oscillation in the global climate system of period 65–70 years, *Nature*, **367**, 723 – 726.
- SCHMITZ, W. J., 1995: On the interbasin-scale thermohaline circulation, *Rev. Geophys.*, **33** (2), 151–173.
- SCHMITZ, W. J., 1996: On the world ocean circulation: Volume I, Some global features / North Atlantic circulation, WHOI-96-03, Woods Hole Oceanographic Institution.
- SCHMITZ, W. J. and M. S. MCCARTNEY, 1993: On the North Atlantic circulation, *Rev. Geophys.*, **31**, 29 – 49.
- SCHOTT, F., T. N. LEE and R. ZANTOPP, 1988: Variability of structure and transport of the Florida Current in the period range of days to seasonal, *J. Phys. Oceanogr.*, **18**, 1209 – 1230.
- SEMTNER, A., 1976: A model for the thermodynamic growth of sea ice in numerical investigations of climate, *J. Phys. Oceanogr.*, **6** (3), 379 – 389.
- SERREZE, M., J. MASLANIK, R. BARRY and T. DEMARIA, 1992: Winter atmospheric circulation in the Arctic Basin and possible relationships to the Great Salinity Anomaly in the northern North Atlantic, *Geophys. Res. Letters*, **19**, 293 – 296.
- SERREZE, M. C., J. E. WALSH, F. S. CHAPIN III, T. OSTERKAMP, M. DYURGEROV, V. ROMANOVSKY, W. C. OECHEL, J. MORISON, T. ZHANG and R. G. BARRY, 2000: Observational evidence of recent change in the northern high-latitude environment, *Climate Change*, **46**, 159 – 207.
- SHY, T. and J. E. WALSH, 1996: North pole ice thickness and association with ice motion history 1977–1992, *Geophys. Res. Letters*, **23** (21), 2975 – 2978.

- SIRABELLA, P., A. GIULIANI, A. COLOSIMO and J. W. DIPPNER, 2001: Breaking down the climate effects on cod recruitment by principal component analysis and canonical correlation, *Mar. Eco. Prog. Ser.*, **216**, 213 – 222.
- SLONOSKY, V. C., L. A. MYSAK and J. DEROME, 1997: Linking Arctic sea ice and atmospheric circulation anomalies on interannual and decadal timescales, *Atmosphere-Ocean*, **35**, 333 – 366.
- SMOLARKIEWICZ, P. K., 1983: A simple positive definite advection scheme with small implicit diffusion, *Monthly Weather Review*, **111** (3), 479 – 486.
- SPALL, M. A., 1996a: Dynamics of the Gulf Stream/Deep Western Boundary Current Crossover. Part I: Entrainment and recirculation, *J. Phys. Oceanogr.*, **26** (10), 2152 – 2168.
- SPALL, M. A., 1996b: Dynamics of the Gulf Stream/Deep Western Boundary Current Crossover. Part II: Low-frequency internal oscillations, *J. Phys. Oceanogr.*, **26** (10), 2169 – 2182.
- STEELE, M. and T. BOYD, 1998: Retreat of the cold halocline layer in the Arctic Ocean, *J. Geophys. Res.*, **103** (C5), 10419 – 10435.
- STEPHENSON, D. B., H. WANNER, S. BRÖNNIMANN and J. LUTERBACHER, 2003: The history of scientific research on the North Atlantic Oscillation, in *The North Atlantic Oscillation Climate Significance and Environmental Impacts*, no. 134 in Geophysical Monograph Series, pp. 37 – 50, American Geophysical Union.
- STEVENS, D. P., 1991: The open boundary condition in the United Kingdom Fine-Resolution Antarctic Model, *J. Phys. Oceanogr.*, **21**, 1494 – 1499.
- STOCKER, T., 1996: An overview of century time-scale variability in the climate system: observations and models, in *Decadal Climate Variability*, D. Anderson and J. Willebrand, eds., vol. 44 of *Series I: Global Environmental Change*, pp. 379 – 406, NATO ASI, Springer-Verlag.
- STOMMEL, H., 1961: Thermohaline convection with two stable regimes of flow, *Tellus*, **13**, 224 – 230.
- STRASS, V. H., E. FAHRBACH, U. SCHAUER and L. SELLMANN, 1993: Formation of Denmark Strait Overflow Water by mixing in the East Greenland Current, *J. Geophys. Res.*, **98** (C4), 6907 – 6919.
- SUTTON, R. T. and M. R. ALLEN, 1997: Decadal predictability of North Atlantic sea surface temperature and climate, *Nature*, **388**, 563 – 567.
- SVERDRUP, H., M. JOHNSON and R. FLEMING, 1942: *Chemistry and General Biology*, chap. The Oceans: Their physics, p. 1042, Prentice-Hall, New York.

Bibliography

- SWIFT, J. H., 1984: The circulation of the Denmark Strait and Iceland - Scotland overflow waters in the North Atlantic, *Deep-Sea Res.*, **31** (11), 1339 –1355.
- THOMPSON, D. W., L. SUKYONG and M. P. BALDWIN, 2003: Atmospheric processes governing the Northern Hemisphere Annular Mode/North Atlantic Oscillation, in *The North Atlantic Oscillation Climate Significance and Environmental Impacts*, no. 134 in Geophysical Monograph Series, pp. 81 – 112, American Geophysical Union.
- THOMPSON, D. W. J. and J. M. WALLACE, 1998: The Arctic Oscillation signature in the wintertime geopotential height and temperature fields, *Geophys. Res. Letters*, **25** (9), 1297 – 1300.
- THOMPSON, J. D. and W. J. SCHMITZ, JR., 1996: A limited-area primitive equation model of the Gulf Stream: Design, initial experiments, and model-data intercomparison, *J. Phys. Oceanogr.*, **19**, 791 – 814.
- TIMMERMANN, A., M. LATIF, R. VOSS and A. GRÖTZNER, 1998: Northern Hemispheric interdecadal variability: a coupled air-sea mode, *J. Climate*, **11**, 1906 – 1931.
- TOMCZAK, M. and J. S. GODFREY, 1994: *Regional Oceanography*, Pergamon Press, London.
- TOURRE, Y., B. RAJAGOPALAN and Y. KUSHNIR, 1999: Dominant patterns of climate variability in the Atlantic ocean region during the last 136 years, *J. Climate*, **12**, 2285 – 2299.
- VAN LOON, H. and J. ROGERS, 1978: The seesaw in winter temperatures between Greenland and northern Europe. Part 1: General description, *Monthly Weather Review*, **106**, 296 – 310.
- VINJE, T., N. NORDLUND and Å. KVAMBEKK, 1998: Monitoring ice thickness in Fram Strait, *J. Geophys. Res.*, **103** (C5), 10437 – 10449.
- VINNIKOV, K. Y., A. ROBOCK, R. J. STOUFFER, J. E. WALSH, C. L. PARKINSON, D. J. CAVALIERI, J. F. B. MITCHELL, D. GARRETT and V. ZAKHAROV, 1999: Global warming and Northern Hemisphere sea ice extent, *Science*, **286**, 1934 – 1937.
- VISBECK, M., E. P. CHASSIGNET, R. G. CURRY, T. L. DELWORTH, R. R. DICKSON and G. KRAHMANN, 2003: The ocean's response to the North Atlantic Oscillation variability, in *The North Atlantic Oscillation Climate Significance and Environmental Impacts*, no. 134 in Geophysical Monograph Series, pp. 113 – 146, American Geophysical Union.
- VISBECK, M., H. CULLEN, G. KRAHMANN and N. NAIK, 1998: An ocean model's response to North Atlantic Oscillation-like wind forcing, *Geophys. Res. Letters*, **25**, 4521 – 4524.

- VON STORCH, H. and F. ZWIERS, 1999: *Statistical Analysis in Climate Research*, Cambridge University Press.
- WADHAMS, P. and N. R. DAVIS, 2000: Further evidence of ice thinning in the Arctic Ocean, *Geophys. Res. Letters*, **27** (24), 3973 – 3975.
- WALKER, G., 1924: Correlation in seasonal variation of weather, ix, *Mem. Indian. Meteor. Dep.*, **24** (9), 275 – 332.
- WALKER, G. and E. W. BLISS, 1932: World weather v, *Mem. Roy. Meteor. Soc.*, **4**, 53 – 84.
- WALLACE, J. M. and D. S. GUTZLER, 1981: Teleconnections in the geopotential height field during the northern hemisphere winter, *Monthly Weather Review*, **109** (4), 784 – 812.
- WALSH, J. and W. L. CHAPMAN, 1990: Short-term climatic variability of the Arctic, *J. Climate*, **3**, 237 – 250.
- WALSH, J. E. and C. M. JOHNSON, 1979: Interannual atmospheric variability and associated fluctuations in the Arctic ice extent, *J. Geophys. Res.*, **84**, 6915 – 6928.
- WEAVER, A. J., M. AURA and P. G. MYERS, 1994: Interdecadal variability in an idealized model of the North Atlantic, *J. Geophys. Res.*, **99**, 12423 – 12441.
- WEAVER, A. J., J. MAROTZKE, P. F. CUMMINS and E. S. SARACHIK, 1993: Stability and variability of the thermohaline circulation, *J. Phys. Oceanogr.*, **23** (1), 39 – 60.
- WEAVER, A. J. and E. SARACHIK, 1991a: The role of mixed boundary conditions in numerical models of the ocean's climate, *J. Phys. Oceanogr.*, **21**, 1470 – 1493.
- WEAVER, A. J. and E. S. SARACHIK, 1991b: Evidence for decadal variability in an ocean general circulation model: an advective mechanism, *Atmosphere-Ocean*, **29** (2), 197 – 231.
- WEAVER, A. J. and S. VALCKE, 1998: On the variability of the thermohaline circulation in the GFDL coupled model, *J. Climate*, **11** (4), 759 – 767.
- WEISSE, R., U. MIKOLAJEWICZ and E. MAIER-REIMER, 1994: Decadal variability of the North Atlantic in an ocean general circulation model, *J. Geophys. Res.*, **99**, 12411 – 12421.
- WELANDER, P., 1986: Thermohaline effects in the ocean circulation and related simple models, in *Large-scale transport processes in oceans and atmospheres*, J. Willebrand and D. Anderson, eds., vol. C 190, pp. 163 – 200, NATO ASI, D. Reidel Publishing Company, Dordrecht.
- WESTERNHAGEN, H. v. and D. SCHNACK, 2001: The effect of climate on fish populations, in *Climate of the 21st Century: Changes and Risks*, J. L. Lozan, H. Graßl and P. Hupfer, eds., pp. 283 – 289, Lozan, José L., Wissenschaftliche Auswertungen, Hamburg.

Bibliography

- WINSOR, P., 2001: Arctic sea ice thickness remained constant during the 1990s, *Geophys. Res. Letters*, **28** (6), 1039 – 1041.
- WOLFF, J.-O., E. MAIER-REIMER and S. LEGUTKE, 1997: The Hamburg Ocean Primitive Equation Model, Tech. Rep. 13, Deutsches Klimarechenzentrum (DKRZ).
- WUNSCH, C., 1999: The interpretation of short climate records, with comments on the North Atlantic and Southern Oscillations, *Bull. Amer. Met. Soc.*, **80** (2), 245 – 256.
- YIN, F. L. and E. S. SARACHIK, 1995: On interdecadal thermohaline oscillations in a sector ocean general circulation model: advective and convective processes, *J. Phys. Oceanogr.*, **25** (11), 2465 – 2484.
- ZALESAK, S. T., 1979: Fully multidimensional flux-corrected transport algorithms for fluids, *J. Comp. Phys.*, **31**, 335 – 362.
- ZHANG, J., D. ROTHROCK and M. STEELE, 2000: Recent changes in the arctic sea ice: the interplay between ice dynamics and thermodynamics, *J. Climate*, **13**, 3099 – 3114.

Acknowledgements

This PhD thesis was written at the Alfred–Wegener–Institute for Polar and Marine Research (AWI) in Bremerhaven. It was funded by the DFG of the Sonderforschungsbereich 512. Thanks to my professor Dirk Olbers* for accepting me as his PhD student and giving me helpful suggestions and support. Thanks also to Professor Peter Lemke* for examining my work.

I am grateful to all the members of the MAD (MOM Arctic Division) group and associates for lots of ideas, discussions and programming support (not to mention all the book tips, social events and charades). The members and alumni are Rüdiger Gerdes*, Cornelia Köberle*, Frank Kauker*, Michael Karcher*, Holger Brix, Matthias Prange, Katrin Meissner, Klaus Grosfeld, Daniel Borowski, Jörg Hurka and one associated observer, Ursel Schauer*.

Special thanks to Rüdiger Gerdes*, who was the head of our group and my supervisor. He never stopped believing in my work and uncountable suggestions. And thanks to Frank* for showing me the secrets of “ppsf” and statistics and for all of his ideas.

The computer support of Chresten Wübber*, Bernadette Fritsch*, Wolfgang Cohrs* and Wolfgang Dieck* was great, thank you very much.

Thanks to Vladimir Ivchenko and Jörg Hurka for the nice atmosphere in our office and the secrets of entertainment value and cryptozoology.

I am grateful to the AWI and Eberhard Fahrback* for the opportunity to participate on a Polarstern cruise (ANT XVIII/3) to Antarctica, where I learned a good deal about sea ice and found good friends.

Thanks to Professor Andrew Weaver for the opportunity to finish my thesis in his working group.

Christian Dieterich was an inexhaustible source for providing shell scripts and programs for every imaginable computer problem. Holger and Katrin were awesome company (before they left me) and they are great friends. Martin*, Heike, Hannah, Nora and Edzilla Losch left me also, but came back to support me in the last months of the thesis with music sessions, gardening work and soul food. Thank you all for being friends and believing in me!

Together with the other members of SgK (Science goes Kitchen), which are Anna von Gyldenfeldt, Jan Lieser* and Christian, I discovered the magic of experimenting in kitchens and the associated eating and drinking. Tobi Boebel fondly managed my evening program and workout. Carmen Hartmann* and Jill Schwarz* were a source of energy and fun. Thank you all for the distractions and inspirations. Thanks to all the friends not mentioned by name but nevertheless important (they will know): in Bremerhaven, Bremen, Hamburg, Wiesbaden, Sidney, Redecke, Warnemünde and the Pfalz.

Thanks to Jill, Katrin, Martin and Holger for reading almost every sentence I’ve written and all the helpful suggestions and britifications (ispell: beautifications).

Thanks to Matthias Früh for the running lesson and mental exercises.

Thanks to Mark, for showing me a glimpse of what lies beyond and Astrid for the still growing friendship.

Last but not least, thanks to my family: danke an meine Ma, für das Kissen und die Wärme, danke an meinen Vater, meine Schwester, meine Oma und meine Tante für die Anrufe und Aufmunterungen.

*Members of the Alfred Wegener Insitut